Title

Alfv&#65533;nic Wave Resonances in the Kronian and Terrestrial Magnetospheres: Modeling and Observations

Author

Rusaitis, Liutauras

Publication Date

2022

Peer reviewed|Thesis/dissertation

UNIVERSITY OF CALIFORNIA
Los Angeles

Alfvénic Wave Resonances in the Kronian and Terrestrial Magnetospheres: Modeling and Observations

A dissertation submitted in partial satisfaction
of the requirements for the degree
Doctor of Philosophy in Geophysics and Space Physics

by

Liutauras Rusaitis

2022

ABSTRACT OF THE DISSERTATION

Alfvénic Wave Resonances in the
Kronian and Terrestrial Magnetospheres:
Modeling and Observations

by

Liutauras Rusaitis
Doctor of Philosophy in Geophysics and Space Physics
University of California, Los Angeles, 2022
Professor Raymond J. Walker, Co-Chair
Professor Margaret G. Kivelson, Co-Chair

Ultra-low frequency (ULF) waves have been commonly detected in inner and outer Solar System planetary magnetospheres. ULF waves with periods that are of the order of the Alfvén wave transit time in a planetary magnetosphere are often associated with resonant field lines that can be excited by either internal or external triggers. In this dissertation, we present a comparative study of standing Alfvén waves in realistic magnetic field and plasma density models for the Kronian and Terrestrial magnetospheres.

At Saturn, we carried out the first calculation of standing wave resonances in a realistic model of the Kronian magnetosphere. The resulting eigenperiods of the 4th harmonic vary little with radial distance from 5 to 20 R_S, matching the quasi-periodic 60-minute (QP60) waves that have been reported in observations at a wide range of local times and radial distances. We have used 13 years of the Cassini magnetometer data and identified quasi-periodic fluctuations with periodicities of around 30 minutes (QP30), 60 minutes (QP60), and 120 minutes

(QP120) that reoccur at the period of planetary period oscillations (PPO) of roughly 10.7 h. We suggest that these correspond to even-mode harmonics of Saturn's magnetic field lines that are excited by the periodic vertical flapping of Saturn's magnetotail.

At Earth, we evaluated the field line resonances for several plasma density models and investigated the effects of geomagnetic activity on the field line eigenperiods up to $L = 10$ at all magnetic local times. We find that the dipole-field and the time-of-flight approximations used to estimate the fundamental eigenperiods of standing waves lead to significantly different eigenperiods, especially during active times. Additionally, the eigenperiods are shown to be more sensitive to the magnetic field configuration and equatorial plasma densities than the distribution of the mass density along the field lines.

Saturn's and Earth's magnetospheres have large differences in scale, rotational speed, and plasma distribution. Despite these differences in the parameter regimes, field line resonances are important at both magnetospheres. The QP30, QP60, and QP120 waves at Saturn reoccur consistently at a PPO period, with the highest transverse to parallel magnetic perturbation power in the post-dusk sector, suggesting mainly an internal driver such as the vertical flapping of the magnetotail. At Earth, the field line resonances that are associated with *Pc4* to *Pc5* waves do not demonstrate similar periodicity in reoccurrence as at Saturn and are likely to be driven externally by processes such as the solar wind dynamic pressure variations.

The dissertation of Liutauras Rusaitis is approved.

Vassilis Angelopoulos

Jacob Bortnik

Krishan Khurana

Margaret G. Kivelson, Committee Co-Chair

Raymond J. Walker, Committee Co-Chair

University of California, Los Angeles

2022

"The world is full of obvious things which nobody by any chance ever observes."

- Arthur Conan Doyle

TABLE OF CONTENTS

LIST OF FIGURES

ACKNOWLEDGMENTS

I first thank my mother, who encouraged my creativity and taught me to be kind. She would have loved to see me finish this degree.

I thank my dad for teaching me that the greatest obstacles are the ones that we set ourselves. He nurtured my curiosity in all things, rational or irrational.

I am also grateful for the advice, support, and patience of my sisters. They inspired me to pursue my studies and provided a tremendous opportunity for growth.

UCLA has now become my academic family and allowed me to continue to grow both personally and professionally. My advisor, Ray Walker, went out of his way to help me throughout the program. I thank him for being the best proofreader, administrator, and advisor that a graduate student can ask for. I am lucky to have enjoyed his excellent taste for coffee, humor, and interesting tidbits of history.

I am grateful to Margy Kivelson for her penetrating insights, advice, and support. I am privileged to have been a part of the Wednesday Kivelson et al. group meeting. Margy inspired me to look at everything with a fresh perspective — I will not see life or science the same way as I used to.

I thank Krishan Khurana for the scientific discussions and tangential philosophical debates. Krishan helped me look at science as an open academic playground where ideas can be tested, sometimes ardently defended, all while being a good sport.

I can also no longer imagine a complete day without an afternoon coffee with the 6th-floor group. I thank Bob McPherron for showing the power of a masterful art of storytelling and that things can always go worse. I have gained immeasurable insights into life and science through these daily discussions.

I am lucky to have Jacob Bortnik and Vassilis Angelopoulos on my committee. Jacob always made himself available for sincere advice, and he has never allowed himself to be beaten in squash, lamenting the fact that he's good at everything. I am grateful to Vassilis for his guidance and dedication to going above and beyond at the journal clubs and seminars

explaining concepts that might puzzle new students.

I have learned much from many other star people at EPSS. I thank Bob Strangeway for his keen eye and commentary, Dave Jewitt for his unrivaled heights of academic humor and insights, Kevin McKeegan for his inspiring passion for teaching and being a fellow CLUSTER 70 cult member, and, of course, Lauri Holbrook, who cares about the graduate students more than Janeway cares for her crew.

UCLA is a welcoming community, and it is hard not to be touched by a wider scope of its members. I am thankful to Troy Carter for being so approachable and demonstrating that one can be fast up Mandeville Canyon and still be good in plasma physics. I also thank Tony Friscia for helping me cultivate my passion for teaching and inspiring me to be a life-long learner.

I would not have made it without the support and company of my fellow graduate students at the EPSS, AOS, and Physics departments. Whether it was supporting each other through ups and downs, turning trivial societal problems into non-trivial debates, or just sharing coffee over an Atlantic article or a programming challenge — it all has been an integral part of the graduate experience.

Last, but not least, I'll always be grateful to Maha Ashour-Abdalla for returning an invite to a young aspiring undergraduate and unknowingly changing his career path.

Funding has been partly provided by the NASA grant UCB #SA3650/NASA NAS5-02099. This support is gratefully acknowledged.

VITA

2013	B.A. (Physics), University of Oxford, St Anne's College.
2014	M.S. (Physics), City College of New York.
2014-2015	Research Assistant, Experimental Condensed Matter Physics, Science Education Department, Columbia University.
2013-2015	RGDX Developer, Science Education Department, Princeton Plasma Physics Laboratory.
2016–2021	Teaching Assistant and Teaching Fellow, CLUSTER 70: Evolution of Cosmos and Life, Undergraduate Education Initiatives, UCLA.
2020	M.S. (Geophysics and Space Physics), University of California, Los Angeles.

PUBLICATIONS

Rusaitis, L., Khurana, K. K., Kivelson, M. G., & Walker, R. J. (2021) Quasiperiodic 1-hour Alfvén wave resonances in Saturn's magnetosphere: Theory for a realistic plasma/field model. Geophysical Research Letters. https://doi.org/10.1029/2020GL090967.

Rusaitis, L., Khurana, K. K., Kivelson, M. G., & Walker, R. J. (2022 – in review) Long-period Alfvén waves as signatures of field line resonances in Saturn's magnetosphere. Journal of Geophysical Research.

Rusaitis, L., Khurana, K. K., Kivelson, M. G., & Walker, R. J. (2022 – in preparation) Alfvén wave resonances in Earth's magnetotail: Eigenfrequency sensitivity to density models and solar wind parameters. Journal of Geophysical Research.

CHAPTER 1

Introduction

1.1 Background

Nature is relentless and unchangeable, and it is indifferent as to whether its hidden reasons and actions are understandable to man or not.

— *Galileo Galilei*

Planetary magnetospheres can be viewed as natural laboratories for a diverse range of interesting plasma physical processes, including ultralow frequency (ULF) waves, occupying an approximate frequency range from 1 millihertz to 10 hertz. ULF waves are a common feature of the magnetospheres of the Earth and the outer planets (Khurana et al., 1992), and they play a dynamic part in wave transport and energy coupling throughout the magnetospheres (Liu & Fujimoto, 2011). They can also be a useful diagnostic tool in the magnetosphere for inferring local plasma properties (Glassmeier et al., 1999; Min et al., 2013). Nevertheless, despite the wealth of ULF observations within the last few decades, some fundamental questions remain regarding the generation, propagation and influences of the waves (Liu & Fujimoto, 2011).

Many features of common ULF events can be understood in terms of standing Alfvén waves. The concept and theory of standing Alfvén waves were first explored by Alfvén (1942a,

1942b) and Dungey (1955) as an application of magnetohydrodynamics (MHD) to waves in a conducting medium embedded in a uniform magnetic field. Alfvén (1942b) likened the magnetic lines of force to elastic vibrating strings because of the frozen-in flux condition and named the resulting waves magnetohydrodynamic (MHD) waves. The coupling between the MHD wave modes, namely the fast (compressional) mode and the shear (Alfvén) mode, was subsequently established as a field line resonance (FLR) or, more generally, a resonant mode coupling phenomenon (Tamao, 1965; Radoski, 1972; Southwood, 1974; Chen & Hasegawa, 1974). In this dissertation, we treat field line resonance as any phenomenon that leads to resonant Alfvén waves, irrespective of the properties of the driver.

The problem of field line resonance is analytically tractable if evaluated using a magnetospheric box model with a uniform magnetic field. Southwood and Kivelson (1986) introduced and investigated a model with a non-uniform box-function density profile to study the effects of the Alfvén velocity gradients along the unperturbed field direction. The effects of plasma inhomogeneity along the field are particularly important for rotationally-driven magnetospheres like Saturn's and Jupiter's, with dense plasma sheets centrifugally confined near the equator. Khurana and Kivelson (1989) modeled the Jovian 10 -20 min ULF waves as FLR's using such a simplified hydromagnetic box model magnetosphere with a two-density plasma distribution. More recently, the hydromagnetic box model has been applied to the study of Saturn's quasiperiodic 60-minute (QP60) waves (Yates et al., 2016), and Jupiter's QP 10-60 min waves (Manners & Masters, 2019).

The spectrum of resonant waves, however, depends significantly on the field structure and the plasma distribution. Resonant frequencies were studied for dipolar fields by (Cummings et al., 1969) and later for more realistic model magnetospheric fields (Warner & Orr, 1979; Singer et al., 1981). Singer et al. (1981) derived and solved linearized transverse wave equations for an arbitrary field geometry, enabling numerical calculations of eigenoscillations for the toroidal and poloidal modes in arbitrary magnetic fields and plasma density distributions. Singer et al. (1981) demonstrated that the model field of Olson and Pfitzer (1974)

significantly modified the mode structure on field lines at high (>70°) geomagnetic latitude at Earth, even if they assumed a uniform density along the field. More recent studies of FLRs in outer planetary magnetospheres also demonstrated the importance of realistic magnetic field models for calculation of the observed standing mode frequencies (Lysak & Song, 2020; Rusaitis et al., 2021). In the following section we describe the formalism of Singer et al. (1981) used in this dissertation for the calculation of field line resonances.

1.2 Theory

We follow the standing wave MHD theory of Singer et al. (1981) for calculations of the field line resonances in a curvilinear coordinate system, neglecting any effects of the centrifugal or Coriolis forces. The stationary plasma conditions are justified, as the timescales of the higher ULF MHD modes are a small fraction of the planetary rotation rate ($\sim 10\%$) (Glassmeier et al., 1999).

From the linear MHD equations for a cold, collisionless, magnetized plasma, the wave electric field $\mathbf{E}$ must satisfy (ignoring the effects of a background current)

$$\frac{\partial^2 \mathbf{E}}{\partial t^2} = \mathbf{v_A} \times (\mathbf{v_A} \times (\nabla \times (\nabla \times \mathbf{E}))). \tag{1.1}$$

where $\mathbf{v_A} = \mathbf{B}/(\mu_0 \rho)^{1/2}$ is the Alfvén velocity, ρ is the local plasma mass density, $\mathbf{B}$ is the background field, and all vectors and differential vector operators in the wave equation depend implicitly on the coordinate along the field line. Using the Alfvén frozen-in flux condition, the wave electric field can be expressed in terms of the plasma (field) displacement $\boldsymbol{\xi}$ as

An edited version of the Theory section was published by AGU (Rusaitis et al., 2021).

$$\mathbf{E} = -\frac{\partial \boldsymbol{\xi}}{\partial t} \times \mathbf{B}. \tag{1.2}$$

In a uniform field embedded in cold plasma of constant density, (1.1) can be used to describe two uncoupled MHD wave modes: the shear Alfvén (transverse) mode, with its Poynting vector directed along $\mathbf{B}$, and the fast (compressional) mode, with a Poynting vector angled at any direction to $\mathbf{B}$ (but parallel to the wave vector $\mathbf{k}$). A plasma or field aligned inhomogeneity, however, couples the two modes. Assuming the longitudinal variation is $e^{im\phi}$, where ϕ is longitude and m is the azimuthal wave number, the modes decouple for special limits of m (see, Orr (1973), for a dipole field case). Two shear Alfvén modes are then possible: one for $m = 0$ (toroidal axisymmetric b_ϕ oscillations), and the other for $m \to \infty$ (poloidal asymmetric oscillations in the meridian plane). The third uncoupled case is a fast (compressional) mode with an axisymmetric ($m = 0$) poloidal disturbance, which represents symmetric expansions and compressions of the entire magnetosphere (Radoski, 1967b; Orr, 1973).

The field of a realistic magnetosphere is non-uniform. We will therefore, consider a model field with two adjacent field lines separated by a distance h_α along a unit vector $\hat{\boldsymbol{\alpha}}$ normal to the background field and by a distance h_β along a unit vector $\hat{\boldsymbol{\beta}}$ normal to both $\mathbf{B}$ and $\hat{\boldsymbol{\alpha}}$. We allow both h_α and h_β to vary along the field. We write the normal unit vector $\hat{\boldsymbol{\alpha}}$ as

$$\nabla\alpha = \hat{\boldsymbol{\alpha}}/h_\alpha. \tag{1.3}$$

We can choose any direction $\hat{\boldsymbol{\alpha}}$ transverse to the field, but we will explicitly define our coordinate system in section 3. Faraday's law and the Alfvén frozen-in flux condition imply that a small displacement in the $\hat{\boldsymbol{\alpha}}$ direction, ξ_α, produces a magnetic perturbation

$$\mathbf{b} = \nabla \times (\xi_\alpha \hat{\boldsymbol{\alpha}} \times \mathbf{B}). \tag{1.4}$$

Substituting (1.4) and Ampères's law in Cauchy's momentum equation (ignoring the

contributions from the background currents), and assuming $\mathbf{b} \cdot \mathbf{B} = 0$ (as in Singer et al., 1981), we arrive at the wave equation for plasma (field) displacement ξ_α

$$\mu_0 \rho \frac{\partial^2 (\xi_\alpha / h_\alpha)}{\partial t^2} = \frac{1}{h_\alpha^2} \mathbf{B} \cdot \nabla \left\{ h_\alpha^2 [\mathbf{B} \cdot \nabla (\xi_\alpha / h_\alpha)] \right\}. \tag{1.5}$$

Assuming a time dependence of the form $e^{i\omega t}$, and writing an increment along the local magnetic field $\mathbf{B}$ as ds, we rewrite (1.5) as a second-order partial differential equation for plasma (field) displacement ξ_α as a function of s

$$\frac{\partial^2}{\partial s^2}\left(\frac{\xi_\alpha}{h_\alpha}\right) + \frac{\partial}{\partial s}\left(ln(h_\alpha^2 B)\right)\frac{\partial}{\partial s}\left(\frac{\xi_\alpha}{h_\alpha}\right) + \frac{\mu_0 \rho \omega^2}{B^2}\left(\frac{\xi_\alpha}{h_\alpha}\right) = 0. \tag{1.6}$$

Once ξ_α is numerically determined using a value of the eigenfrequency, ω, that satisfies the homogeneous boundary conditions at the ionosphere ($\xi_\alpha = 0$), the magnetic perturbation, b_α, electric field perturbation E_β, and the plasma velocity, u_α, can be calculated using (1.4) and (1.2) as

$$b_\alpha = h_\alpha B \frac{\partial}{\partial s} \frac{\xi_\alpha}{h_\alpha} \tag{1.7}$$

$$E_\beta = -i\omega \xi_\alpha B \tag{1.8}$$

$$u_\alpha = i\omega \xi_\alpha \tag{1.9}$$

where $\hat{\boldsymbol{\beta}}$ is a unit vector perpendicular to both the unperturbed field $\mathbf{B}$ and the chosen normal vector to the field $\hat{\boldsymbol{\alpha}}$, i.e.

$$\hat{\boldsymbol{\beta}} = \frac{\mathbf{B}}{|\mathbf{B}|} \times \hat{\boldsymbol{\alpha}}. \tag{1.10}$$

We find orthogonal perturbations ξ_β, b_β, and E_α by solving (1.6) for a geometric scale factor, h_β, orthogonal to h_α. Equations analogous to (1.7) to (1.9) apply to the $\hat{\boldsymbol{\beta}}$ components of the perturbations.

1.3 Synopsis

In Chapter 2, we present the first model of field line resonances in a realistic Saturn's magnetosphere (Rusaitis et al., 2021), building on top of the work of Singer et al. (1981) introduced in the preceding section. We calculate the eigenfrequencies of the first 6 modes for noon and midnight meridian field lines with equatorial crossing distances up to $20\,R_{\mathrm{S}}$. We show that the frequency of the 4th harmonic matches closely that of the QP60 waves, and the eigenfrequencies vary little with radial distance between 5 and $20\,R_{\mathrm{S}}$ as in the observations of the QP waves.

In Chapter 3, we analyze 13 years of the Cassini magnetometer data from Saturn's magnetosphere and identify quasiperiodic fluctuations with periods up to 3 hours (Rusaitis et al., 2022, in-review). We find signatures of quasiperiodic pulsations corresponding to the even harmonics in a field line resonance model at around 30 minutes (QP30), 60 minutes (QP60), and 120 minutes (QP120). These quasi-periodic waves come in wave trains of 4-to-5 hours before decaying in amplitude, but typically reoccur in the magnetic field data at the planetary period oscillation (PPO), roughly every 10.7 hours. We suggest that these even-mode harmonics of Saturn's magnetic field lines are excited by the periodic vertical flapping of Saturn's magnetotail.

In Chapter 4, we investigate field line resonances at Earth for an increasing geomagnetic activity from $0\,\mathrm{nT}$ to $-100\,\mathrm{nT}$ Dst (Rusaitis et al., 2022, in-preparation). We use a realistic magnetic field and plasma density model that are parameterized by the geomagnetic indices Dst and K_p, and we calculate eigenfrequencies of the first 4 modes for field lines at all magnetic local times between 3 and $10\,R_{\mathrm{E}}$. Additionally, we evaluate the deviations in the resulting eigenperiods from those using a dipolar-field and WKB approximations and investigate the effect of assuming different mass density distributions along the field line. We compare our calculated eigenfrequencies to some of the ULF observations.

In the last Chapter 5, we summarize the results of the three studies and comment on

the main differences and similarities between field line resonances in the magnetospheres of Earth and Saturn. We conclude by discussing the limitations of these studies and possible directions of further study.

CHAPTER 2

Quasiperiodic 1-hour Alfvén Wave Resonances in Saturn's Magnetosphere: Theory for a Realistic Plasma/Field Model

2.1 Introduction

If you do not change direction, you may end up where you are heading.

— *Lao Tzu*

One of the more puzzling features in Saturn's magnetosphere is the source of persistent quasi periodic 60-minute (QP60) phenomena, which became particularly apparent during continuous in-situ investigations by the Cassini spacecraft from 2004 to 2017. The QP60 phenomena are observed in much of the magnetospheric data – from magnetic field fluctuations (Bunce et al., 2014; Mitchell et al., 2016; Yates et al., 2016) and field-aligned electron beams and ion conics (Schardt et al., 1985; Mitchell, Kurth, et al., 2009) to auroral pulsations (Mitchell, Krimigis, et al., 2009; Mitchell et al., 2016; Bunce et al., 2014; Bader et al., 2019;

An edited version of this chapter was published by AGU (Rusaitis et al., 2021).

Menietti et al., 2020) and auroral hiss (Carbary et al., 2016). An extensive global survey of these events is provided by Roussos et al. (2016) and Palmaerts et al. (2016), focusing both on their spatial and spectral distribution. We will focus on the transverse quasi-periodic magnetic field perturbations in this chapter.

The QP60 magnetic field oscillations were found mostly in the outer magnetosphere, mapping inside Titan's orbit of roughly 20 R_S (Carbary et al., 2016) and beyond, with highest frequency of occurrence in the dusk sector and mid-to-high latitudes (Roussos et al., 2016). The field perturbations are typically transverse to the magnetic field with amplitudes between 0.1 and 1 nT (Kleindienst et al., 2009; Yates et al., 2016), and come in short wavetrains – i.e., they typically last ∼5 hours before decaying. The Alfvénic signature of these perturbations, as well as the persistence of the 1-hour periodicity over a wide range of local times, distances, and latitudes is indicative of characteristic time scales of the Kronian magnetosphere. Simple estimates of the Alfvén inter-hemispheric transit times in the outer Kronian magnetospheres are found to be close to 1 hour, or roughly within 10% of the planetary rotation period, consistent with the idea that the observed periodic perturbations are standing Alfvén waves (Bagenal et al., 2017; Bunce et al., 2005).

In this chapter, we present the first model of the field line resonances in Saturn's magnetosphere using a realistic model of the magnetic field and plasma density. We show it is important to do so in order to fully understand the peculiar characteristics of the QP60 waves.

2.2 Model

We use a global magnetic field of the Saturn's field (Khurana et al., 2006), based on the general deformation technique of Tsyganenko (1998, 2002). Saturn's internal field uses magnetic moments derived from Cassini's proximal orbits (Cao et al., 2011, 2012). The field lines calculation use nominal solar wind conditions of dynamic pressure $D_P = 0.017\,\mathrm{nPa}$,

$B_z = 0.1\,\mathrm{nT}$, $B_y = -0.2\,\mathrm{nT}$, and are traced using a 4th order Runge Kutta method in a dipole centered coordinate system with x pointing towards the Sun (with Saturn's magnetic equivalent dipole being offset 0.04 R_S northward of the center of mass of Saturn).

Thanks to many Cassini plasma sheet crossings, models of plasma sheet densities and scale heights are available (Bagenal & Delamere, 2011). We use the equatorial water-group ion density profiles within the 3 to 20 R_S region and use a local cubic spline to obtain the density on field lines that extend slightly beyond the modeled density profiles, crossing the equator within 20 R_S, sufficiently far out to represent regions where some of the quasi-periodic pulsations have been observed. The density variation along the field line uses an exponential scale height given by Hill and Michel (1976)

$$n(s) = n_0 exp(-s/H)^2 \tag{2.1}$$

where s is distance along the field line, with $s = 0$ the maximum radial distance of the field line, the center of the plasma sheet, and we use the water-group ion scale height, H, given in Bagenal and Delamere (2011, Figure 5). We use the same equatorial plasma density profiles for the day-side and night-side, but allow the field line configuration to change with local time.

The solution of the second order partial differential equation for displacement, ξ_α, (Equation 1.6) uses a shooting method (see Press, 2007, §18) with homogeneous boundary conditions in the ionosphere. We start with $\xi_\alpha = 0$ at the northern ionosphere, selecting the eigenfrequencies, ω, and the initial displacement derivatives, $d\xi/ds$, that satisfy homogeneous boundary conditions at the other end of the field line.

The local geometric scaling factors, h_α, in equation (1.3) are calculated by using flux conservation along a magnetic field line. Starting from an equatorial position of the field line, two nearby field lines are mapped, displaced from the original by a finite increment along unit vectors $\hat{\boldsymbol{\alpha}}$ and $\hat{\boldsymbol{\beta}}$:

$$\hat{\boldsymbol{\alpha}} = \hat{\mathbf{b}}_{\parallel} \times \hat{\boldsymbol{\phi}} \Big/ \left| \hat{\mathbf{b}}_{\parallel} \times \hat{\boldsymbol{\phi}} \right| \tag{2.2}$$

$$\hat{\boldsymbol{\beta}} = \hat{\mathbf{b}}_{\parallel} \times \hat{\boldsymbol{\alpha}} \tag{2.3}$$

where $\hat{\mathbf{b}}_{\parallel}$ is a unit vector along the field line.

We verify our implementation of the model by calculating properties of the field line resonances in a purely dipolar field (Cummings et al., 1969) using the wave equation (1.1) expressed in orthogonal dipole field coordinates. We also test our calculation by reproducing the known scale factors for a dipole field, i.e., $h_\alpha = (rB\sin\theta)^{-1}$ and $h_\beta = r\sin\theta$.

A cross-section of a portion of the magnetosphere (field lines at invariant latitudes of 64 to 73 degrees) is visualized in Figure 2.1 for the day and night sides, with (a) the plasma density and (b) the Alfvén velocity color-coded along the field. The peak of the plasma density ($\sim 70\,\mathrm{cm}^{-3}$) is at 4 R_S near the orbit of Enceladus, but the Alfvén velocity (especially close to the magnetic equator) varies little with x along the equator and the changes along the field are similar from one field line to the next. This will help us understand the eigenfrequencies that we discuss later.

2.3 Results

Consider a single field line that crosses the day-side equator at 20 R_S (invariant latitude 75.8°) in the field model. The wave electric field, $E_\perp$ (shown in Figure 2.2a) and magnetic field perturbation, $b_\perp$ (shown in Figure 2.2b), represent a typical form of an eigenoscillation in the outer magnetosphere of our model, calculated using the shooting-method procedure explained in the previous section. The eigenperiods of the third and fourth harmonics, 75 and 52 minutes, match the expected period of a QP60 event, while the eigenperiods of the second and first harmonics, 121 and 469 minutes, are well outside the typical QP60 range. The poloidal field displacement, $\boldsymbol{\xi}_\perp$ is shown in yellow in Figure 2c for the fourth harmonic

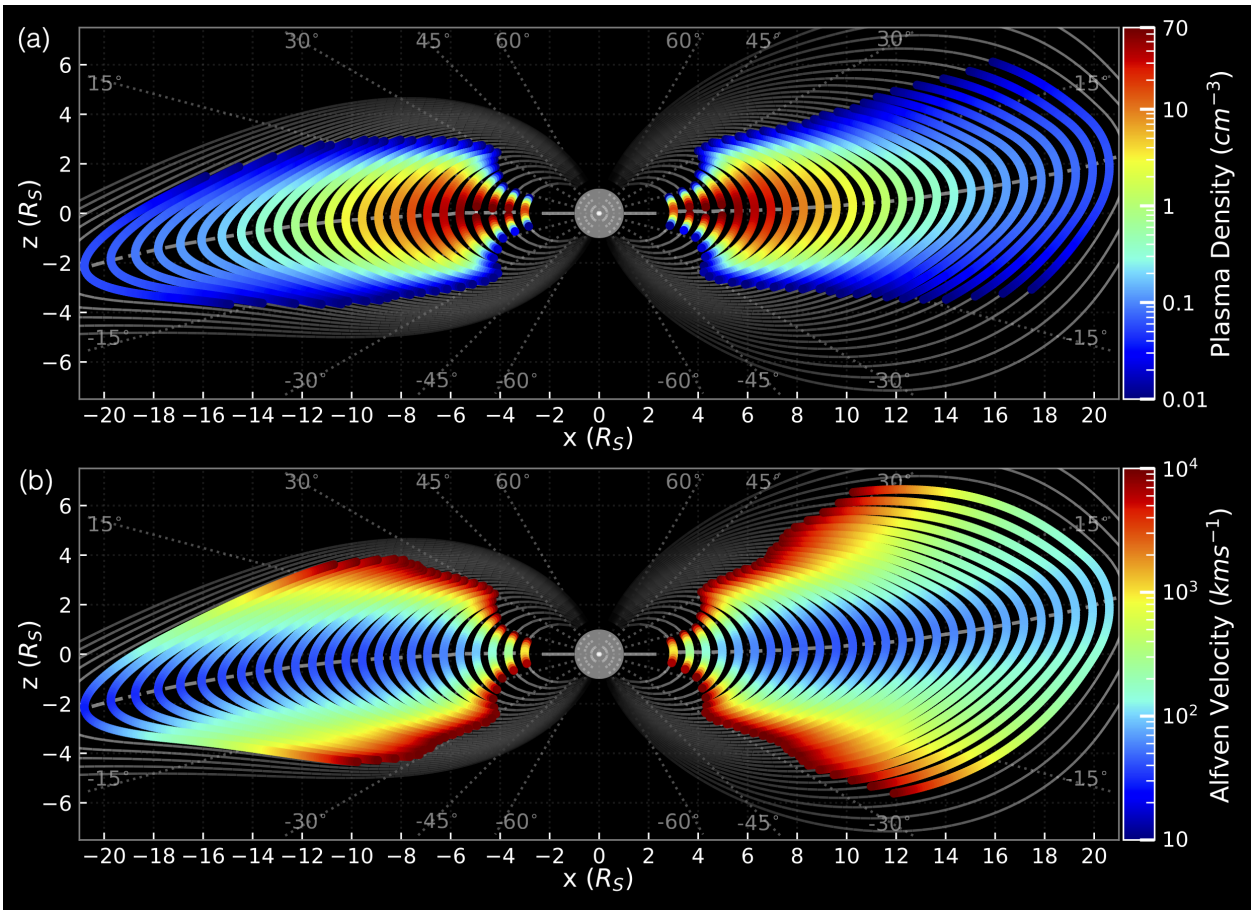

Figure 2.1: (a) Color plot of the plasma density (Bagenal & Delamere, 2011) in Saturn's magnetic field model (Khurana et al., 2006), visualized along field lines (solid lines, both colored and gray) of equatorial crossing distances of 3 to 24 R_S. The field is in a dipole-centered coordinate system, with the x axis pointing towards the Sun. The field reversal position is marked with a thick gray dashed line. (b) Alfvén speed color plot, based upon the plasma densities and field lines visualized in Figure 1a.

of the same field line. Other harmonics are shown in different colors for three sufficiently separated field lines for visual clarity. As required in our wave equation solutions, the field displacement vanishes to zero at the ionosphere.

Note the magnetic field perturbation, $\mathbf{b}_\perp$, amplitude at high latitudes (> 60 degrees) surpasses the amplitude at the equator (Figure 2.2b). This is consistent with the fact that QP60 pulsations are less frequently observed at the equator than at mid-to-high latitudes (Roussos et al., 2016; Palmaerts et al., 2016), perhaps because they are more readily detectable at higher latitudes where the perturbation amplitude is greater. This latitude dependence is also a feature of perturbations in a dipolar field; similar variation with latitude can be observed in the numerical results of Cummings et al. (1969) for the standing waves in Earth's dipole field, in which the perturbations at the ionosphere are 10 times larger than those at the equator. A hydromagnetic box model like the one in Southwood and Kivelson (1986) and Yates et al. (2016), in contrast, produces relatively small amplitudes of magnetic perturbations outside the plasma sheet because of the uniform magnetic field and low plasma density outside the plasma sheet.

The nodes and the local peaks of field perturbations occur within the denser region of the plasma sheet (Figure 2.2a). The exception to this is the fundamental mode, which does not have any nodes beyond the ionosphere, and is less sensitive to the ambient plasma. The close spacing of the nodes of the higher harmonics near the equator (or equivalently, the short parallel wavelength of the perturbations) can be understood by evaluating the radius of curvature, R_c, which for slow changes of the field magnitude, can be approximated (see Riley et al., 2006) as

$$\frac{\hat{\mathbf{n}}}{R_c} \approx -\frac{(\mathbf{B}\cdot\nabla)\mathbf{B}}{B^2} \tag{2.4}$$

Let's consider a small perpendicular perturbation, $\mathbf{b}_\perp$, in the $\hat{\boldsymbol{\alpha}}$ direction. Since $(\hat{\mathbf{B}}\cdot\nabla) = \partial/\partial s$ for a field-aligned coordinate system, we can rewrite (2.4) as

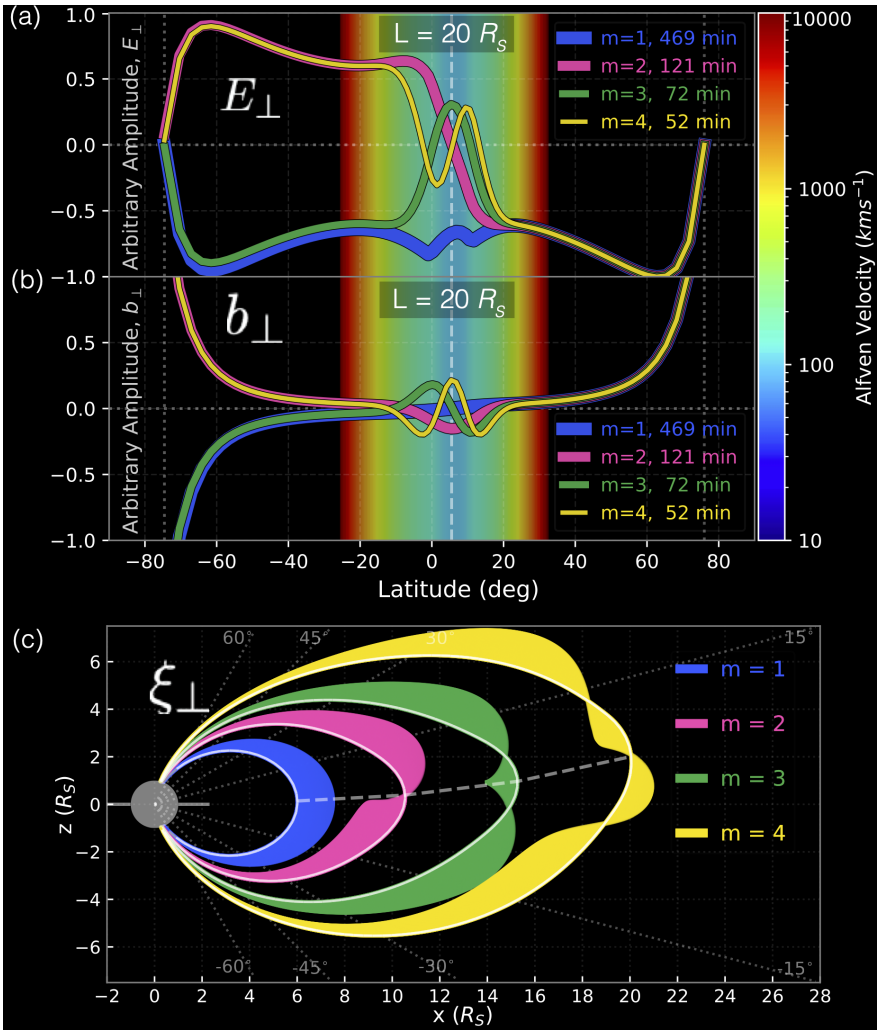

Figure 2.2: (a) The wave electric field, $\mathbf{E}_\perp$, and (b) magnetic field perturbations, $\mathbf{b}_\perp$, shown for the first four harmonics of a field line with an equatorial crossing distance of 20 R_S. The Alfvén velocity along the field line is color coded in the background. (c) Poloidal field displacement, $\boldsymbol{\xi}_\perp$, for the first four harmonics, drawn perpendicularly to four arbitrarily chosen day-side field lines that are sufficiently separated to display distinct nodal structures of the first four harmonics. All quantities in (a)-(c) are normalized to an arbitrary amplitude of one.

$$\frac{\hat{\mathbf{n}}}{R_c} \approx -\frac{\partial}{\partial s}\left(\frac{\mathbf{B}+\mathbf{b}}{|\mathbf{B}+\mathbf{b}|}\right) \approx -\frac{\hat{\mathbf{n}}}{R_{c,B}} - \frac{\partial}{\partial s}\left(\frac{b_\alpha \hat{\boldsymbol{\alpha}}}{h_\alpha B}\right) \approx -\frac{\partial}{\partial s}\left(\frac{b_\alpha \hat{\boldsymbol{\alpha}}}{h_\alpha B}\right) \tag{2.5}$$

where we neglected the contribution of the perturbation to the total field strength in the denominator. We substitute the expression for b_α (1.7) for the last term in (2.5), assuming the geometric scale factor, h_α, varies negligibly near the equator. Since the radius of curvature of the background field, $R_{c,B}$, is big, and $\hat{\boldsymbol{\alpha}}$ changes slowly with s, we then get

$$\frac{\hat{\mathbf{n}}}{R_c} \approx -\hat{\boldsymbol{\alpha}}\frac{\partial}{\partial s}\left(\frac{b_\alpha}{h_\alpha B}\right) = -\hat{\boldsymbol{\alpha}}\frac{\partial^2}{\partial s^2}\left(\frac{\xi_\alpha}{h_\alpha}\right) \tag{2.6}$$

Noting that the second term in (1.6) scales like variations in the background field and is small above the fundamental

$$\frac{\hat{\mathbf{n}}}{R_c} = \left(\frac{\hat{\boldsymbol{\alpha}}}{h_\alpha}\right)\frac{\omega^2}{v_A^2}\xi_\alpha \tag{2.7}$$

where b_α is a field perturbation in the $\hat{\boldsymbol{\alpha}}$, direction and we assumed the orientation of the background field to be changing slowly at the equator.

Therefore, a small radius of curvature in a region of low Alfvén velocity implies that the perturbation reverses sign over a comparatively short range of s, and that the local wavelength of the perturbation field is small.

This explains the close spacing of the nodes of the perturbation near the equator, but does not account for the high perturbation amplitudes near the plasma sheet and in the tenuous high-latitude regions. High amplitudes closer to the ionosphere can be viewed as an effect of a curvilinear field geometry, where the field strength becomes large close to the planet. Even small reorientation of a strong field can create a significant perturbation field. As seen in equation (1.7), the magnetic perturbation amplitude, b_α, is proportional to the magnitude of the unperturbed field, $|\mathbf{B}|$.

Because we use a realistic model of Saturn's magnetic field, the field lines of the same

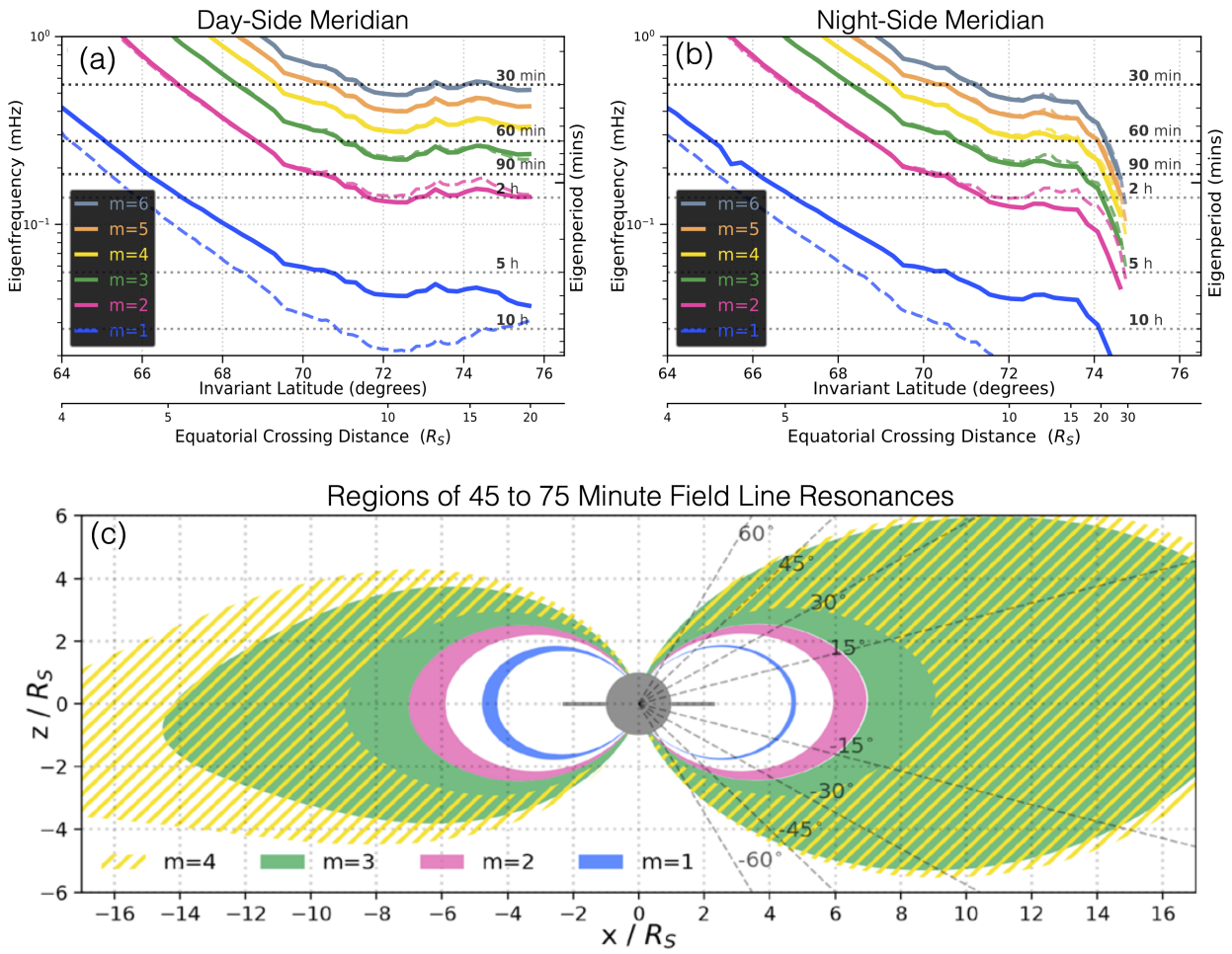

Figure 2.3: (a) Eigenfrequencies for the first 6 toroidal (solid) and poloidal (dashed) modes for varying invariant latitudes of field lines in the day side of Saturn's magnetosphere. (b) Same as (a), but for the night-side meridian. (c) Regions of 45 to 75 minute field line resonances for the first four modes, shown for the day and night side meridian planes.

invariant latitude map differently from ionosphere to equator in the day-side and night-side meridians (see Figure 2.1a and 2.1b). We calculate the resonant periods separately for the day-side and night-side field lines (Figure 2.3a and 2.3b, respectively) for both the toroidal and the poloidal modes. Only the fundamental gives values that notably differ between the two modes, similar to the findings of Orr and Matthew (1971), but in the outer magnetosphere, those periods greatly exceed 1 hour. Consequently, we will not distinguish between the toroidal and the poloidal modes.

Field line resonances in substantial regions of the outer magnetosphere (invariant latitudes of 72 to 76 degrees on the day-side, and 72 to 74 degrees on the night-side) have periods that vary little with equatorial crossing distance for the harmonics above the fundamental. The third (odd) and the fourth (even) harmonics oscillate at close to a 60-minute period in this region. The field lines with 60-minute resonances map to equatorial radii of 10 to 20 R_S. Notably, the resonant periods on the night-side start to increase sharply past 74 degrees invariant latitude. Since the field is highly stretched on the night side, the field lines map into a region outside the validity of the plasma sheet models of Bagenal and Delamere (2011). A model of the plasma sheet density valid at larger distances might reveal a larger region for the 1-hour eigenoscillations on the night side. The day-side magnetosphere, on the other hand, is compressed, and the resonant periods remain roughly constant for field lines of higher invariant latitudes, even close to the magnetopause.

The regions in which field lines resonate with periods of 45 to 75 minutes are indicated in 2.3c. Only the 3rd and the 4th harmonics resonate at $\sim$ 1-hour eigenperiods (45 to 75 minutes) in the outer magnetosphere (10 to 20 R_S in radial distance from the planet), with the fundamental and the second harmonic resonating close to this period only in very narrow ranges close to the planet. If we compare our results to those for a purely dipolar field embedded in the same plasma distribution, it becomes apparent that a realistic field model is important for producing these large regions of field lines resonances with 1-hour periodicities (see Figure S1). The eigenperiods in the dipole model decrease continuously

with L, and beyond $\sim$ 15 R_S do not fall in the required 45 to 75 minute range. Saturn's field becomes decreasingly dipolar beyond $\sim$10 R_S from the planet, and the stretched-out field geometry produces a roughly constant eigenperiod in the outer magnetosphere (at least up to 20 R_S in our model). Thus, neither a hydromagnetic box model nor a dipole field provides a valid model of the periodic phenomena observed in Saturn's magnetosphere.

2.4 Conclusion

Using the approach introduced by Singer et al. (1981), we have calculated the resonant frequencies of MHD waves in regions within $\sim$ 20 R_S of Saturn using realistic models of the magnetic field (Khurana et al., 2006) and the plasma density (Bagenal & Delamere, 2011). We find that field line resonances can produce the quasi-periodic $\sim$ 60–minute pulsations reported in particle and field data. As contrasted with the standing wave periods calculated in a hydromagnetic box model, the eigenperiods matching the observations the closest are produced by the third (odd) and fourth (even) harmonics, rather than the second (even) mode (Yates et al., 2016). The period of the fundamental is comparable to the rotational rate of the planet, prohibiting the development of such long-period Alfvén standing modes (Glassmeier et al., 2004). Higher harmonics may also be present in Saturn's magnetosphere but the wave power at the higher frequencies is probably not observable.

We have established that a realistic magnetic field model is important for obtaining quantitative eigenperiods of field line resonances, especially in the outer magnetosphere. Even the combination of a realistic plasma density distribution and a purely dipolar model produces model eigenperiods that continue to increase with L beyond roughly 15 R_S, inconsistent with the widespread appearance of fluctuations in the $\sim$ 60-minute range. Our implementation of a realistic field model reveals that there are large regions in the outer magnetosphere (10 to 20 R_S) in which resonances have eigenperiods in the 45 to 75-minute range, even as the flux tubes become long compared with the height of the high density region near the equator. We

would expect to identify fewer pulsations at latitudes of 15 to 60 degrees. At the equator, the plasma sheet is dense, and the local peaks are confined to a narrow region of roughly ± 15 degrees. Many QP60 pulsations have been detected very close to the equator (Palmaerts et al., 2016), but the closeness of the magnetic field perturbation nodes may make it difficult to distinguish between the odd and even modes (Figure 2.2b).

We were limited to considering field lines that cross the equator within 20 R_S by the restricted distance range of the plasma density model; it would be informative to extend the plasma density model to establish if eigenperiods of 1-hour extend into the outer magnetosphere beyond 20 R_S. Our model assumes wave perturbations transverse to the background field and a perfectly conducting ionosphere (i.e. $E_\perp = 0$ at the field line boundaries). These assumptions can be justified. Most of the QP60 pulsations map to the auroral zone on closed field lines (Roussos et al., 2016). The highly-conducting auroral regions of the ionosphere satisfy our $E_\perp \sim 0$ condition most closely and should provide sufficiently good reflection for the development of a standing wave. Nevertheless, the fact that these Alfvén waves come in $4-6$ hour wave trains implies a dissipation mechanism, and wave damping by a less than perfectly conducting ionosphere could account for the wave decay. However, a quantitative model of wave decay also requires knowledge of the time-variation of the driving source, which is not readily characterized.

Our work also neglected the effects of Saturn's rotating plasma (similar to Glassmeier et al., 1989). We believe this approximation is valid for the higher resonance modes, for which the plasma is quasi-stationary relative to the MHD wave timescales. An analytical treatment of MHD perturbations in a rotating plasma by Ferrière et al. (1999) shows that the stability of the Alfvén modes either remains unchanged or increases with the inclusion of the Coriolis force, albeit for constant background parameters along the field. Furthermore, the estimates of magnetic Rossby numbers by Glassmeier et al. (1999) show that rotation has no significant impact on any resonant coupling at Jupiter or Saturn.

Although the classical mechanism of field line resonances seems plausible, it is chal-

lenging to identify the energy source that excites the oscillations. Any phenomenon that disturbs a quasi-equilibrium state of the magnetosphere can, in principle, excite field line resonances. Possible sources include such external disturbances as interplanetary shocks or pressure fronts, boundary oscillations driven by the Kelvin-Helmholtz instability or magnetic reconnection, and internal disturbances such as those arising from reconnection in the plasma sheet. Because the third and fourth harmonics map to field lines close to the magnetopause, the possibility of the waves being driven externally by the solar wind buffeting (Mathie & Mann, 2000), or alternatively, by the Kelvin Helmholtz instability at the magnetopause boundary (Fujita et al., 1996) becomes an attractive suggestion. Resonant mode coupling between fast mode magnetopause surface waves and the local Alfvén waves has been previously reported in Saturn's magnetosphere – transverse Alfvén perturbations have been observed two hours after an observation of Kelvin Helmholtz waves of the same period, albeit of 23 min periodicity, not 1 hour (Lepping et al., 1981; Cramm et al., 1998). A proposed explanation for the source of these waves, at least on the day side, is magnetodisk reconnection (Guo et al., 2018). Guo et al. (2018) observed QP60 events for 14 hours during a reconnection event, and the energy flux has been estimated to be high enough to power aurorea ($\sim 2.6\,\mathrm{mWm^{-2}}$). If the QP60 events, including the auroral pulsations, are driven by magnetodisc or magnetopause reconnection, we could estimate the energy input into the FLR's and model their dissipation.

Further data analysis of the distribution, magnitude, and symmetry of the quasi-periodic waves will show if their properties match those of our modeled third to fifth harmonics. Particularly, we would expect to see more pulsations at magnetic latitudes of 60 degrees and higher, where the magnetic field perturbation amplitudes surpass those at the equatorial plasma sheet. As seen in Figure 2.3, the third to fifth mode with a period in the critical range can develop through much of the outer magnetosphere.

CHAPTER 3

Long-period Alfvén waves as signatures of field line resonances in Saturn's magnetosphere

The fool doth think he is wise, but the wise man knows himself to be a fool.

— Shakespeare

3.1 Introduction

Ultralow-frequency (ULF) pulsations have been observed at Jupiter and Saturn since the Pioneer 11 and Voyager missions. Kivelson (1976) reported frequent ULF wave activity in particle fluxes and magnetic perturbations in the Jovian magnetosphere near current sheet crossings. Pulsations with 6 to 18 min periods were prominent in the middle magnetosphere and the turbulent layer near the magnetosheath. Voyager observations also revealed strong transverse magnetic field power in the 10 to 20 min band within the plasma sheet, diminishing rapidly outside of it (Khurana & Kivelson, 1989; Wilson & Dougherty, 2000). Wave periodicities of 15 min (QP15) and 40 min (QP40) period were also found in the Ulysses ion

An edited version of this chapter was submitted for publication in Journal of Geophysical Research (JGR).

data (MacDowall et al., 1993; McKibben et al., 1993). At Saturn, Cramm et al. (1998) examined the Voyager 1 spacecraft observations and found Alfvén waves of roughly 20 min period. They linked them to surface mode waves through resonant mode coupling.

More conclusive observations of ULF waves in the Kronian magnetosphere came later following Cassini's orbital insertion in 2004. The continuous in-situ investigations by the Cassini spacecraft revealed consistent quasiperiodic fluctuations in the magnetometer data, especially in broad band frequencies near 60 min (QP60) period (Dougherty et al., 2004; Bunce et al., 2014; Mitchell et al., 2016; Yates et al., 2016). Kleindienst et al. (2009) characterized the magnetic field fluctuations as mostly Alfvénic with amplitudes between 0.1 and 3 nT and found that they occur nearly uniformly in local time and radial distance. The waves were observed to be organized in short packets of 5 to 6 oscillations and modulated with a periodicity close to Saturn's rotation period (Kleindienst et al., 2009). Quasiperiodic oscillations of nearly one-hour period were also reported in field-aligned electron beams and ion conics (Mitchell, Kurth, et al., 2009; Schardt et al., 1985) and linked to the observations of auroral pulsations by the Cassini UVIS instrument (ultraviolet imagining spectrograph) (Bader et al., 2019; Bunce et al., 2014; Menietti et al., 2020; Mitchell, Krimigis, et al., 2009; Mitchell et al., 2016). An extensive global survey of pulsations in relativistic electron events by Roussos et al. (2016) and Palmaerts et al. (2016) revealed occurrence preference for high magnetic latitudes and the dusk sector, with most of the events seen between 20 and 30 R_S. Carbary et al. (2016) analyzed plasma wave data and found amplitude modulation at approximately 60 min of wave emissions at ∼100 Hz frequencies. They last from ∼2 to ∼20 h and map mostly inside of Titan's orbit at 20 R_S on closed field lines.

A more recent survey of QP60 waves in the magnetometer data identified a rapid wave power decrease beyond 25 R_S both in the morning and afternoon sectors, indicating that the waves are not related to the magnetosheath or the solar wind (Pan et al., 2021). Unlike the QP60 events in the energetic electron and plasma data, the events in the magnetic field data were most frequently seen near noon (Pan et al., 2021). Kleindienst et al. (2009) argued that

due to the size and rapid rotation of Saturn's magnetosphere, the ULF waves are unlikely to be eigenoscillations of the entire magnetosphere. Initial calculations of Alfvén travel times indeed came close to the planetary rotation period (∼10 h), which would prevent the development of global standing modes (Cramm et al., 1998; Glassmeier et al., 2004). More recent estimates of the Alfvén travel times by Bunce et al. (2005) showed that they are closer to 1 h, which would allow global standing modes to develop.

Previous investigations of quasi-periodic waves in the magnetic field were either closely focused on the occurrence of disturbances in a narrow band of frequencies near 60-min period (Pan et al., 2021) or identified general ULF-pulsation characteristics in the data (Kleindienst et al., 2009). In this study, we have undertaken a comprehensive search for waves in the Cassini magnetometer data in a wider range of periods (up to 3 hours) for all 13 years that Cassini was in orbit about Saturn. In section 3.2, we present the methods for our data analysis. In section 3.3, we present our analysis results and compare them to a model of standing waves in a realistic magnetic field. In section 3.4, we summarize the observational results and propose the source of QP wave periodicity. We conclude that the QP30, QP60, and the QP120 waves are even harmonic modes of field line resonances in Saturn's outer magnetosphere, excited by periodic flapping of the magnetotail once a PPO period.

3.2 Methods

We utilized all the fluxgate magnetometer (FGM) data acquired in Saturn's magnetosphere during the Cassini mission at 1-min resolution (Dougherty et al., 2006). Focusing on waves within the magnetosphere, we used the list of magnetopause and bow shock crossings compiled by Jackman et al. (2019) to select the intervals when the Cassini spacecraft was in the solar wind, the magnetosheath and the magnetosphere. The position of the orbiter is displayed by local time and latitude in Figure 3.1a, each dot representing a one-day-long data segment. The black crosses represent flagged (rejected) data and color denotes the

plasma environment of the orbiter: solar wind (red), magnetosheath (orange), or magnetosphere (blue). Cassini's dwell time in different parts of the magnetosphere is non-uniform – for instance there is less coverage of the magnetosphere between 6 and 10 h local time, especially at higher magnetic latitudes, than at other local times.

FGM calibration procedures typically required spacecraft rolls at a period that comes close to the lower end of the period of the waves of our study, and the calibrated data may contain some unwanted leftover signals. Therefore, we rejected data segments that included more than one hour of calibration rolls or contained data gaps larger than 30 min within a single 24-hour data interval. Even with these two data constraints (removal of calibration intervals and of intervals with significant data gaps), we had 4278 days of magnetospheric data, representing nearly 90.7 % of the total 4714 recorded days inside Saturn's magnetopause. Before analysis, we padded each 24-hour data segment with 6 hours of data before and after the segment, or roughly half the Saturn's planetary period oscillation (PPO) period, which is roughly 10.7 h and appears in many magnetospheric phenomena (Carbary et al., 2016). This data redundancy allowed for more reliable identification of events at the start and end of each day.

To understand how the wave activity is distributed through the magnetosphere, we trace along the magnetic field to the surface of the planet using a global magnetic field model of Saturn's field (Khurana et al., 2006) based on the general deformation technique of Tsyganenko (1998). The field line calculations are carried out for a model that adopts nominal solar wind conditions with dynamic pressure $D_P = 0.017\,\mathrm{nPa}$, $B_z = 0.1\,\mathrm{nT}$, $B_y = -0.2\,\mathrm{nT}$. Field lines are traced by using a 4th order Runge-Kutta method in a dipole-centered coordinate system with x pointing towards the Sun (with Saturn's magnetic equivalent dipole being offset $0.04\,R_\mathrm{S}$ northward of the center of mass of Saturn). For Saturn's internal field, the magnetic field model uses magnetic moments derived from Cassini's proximal orbits (Dougherty et al., 2018).

The field line traces grouped by local time and conjugate (sometimes called invariant)

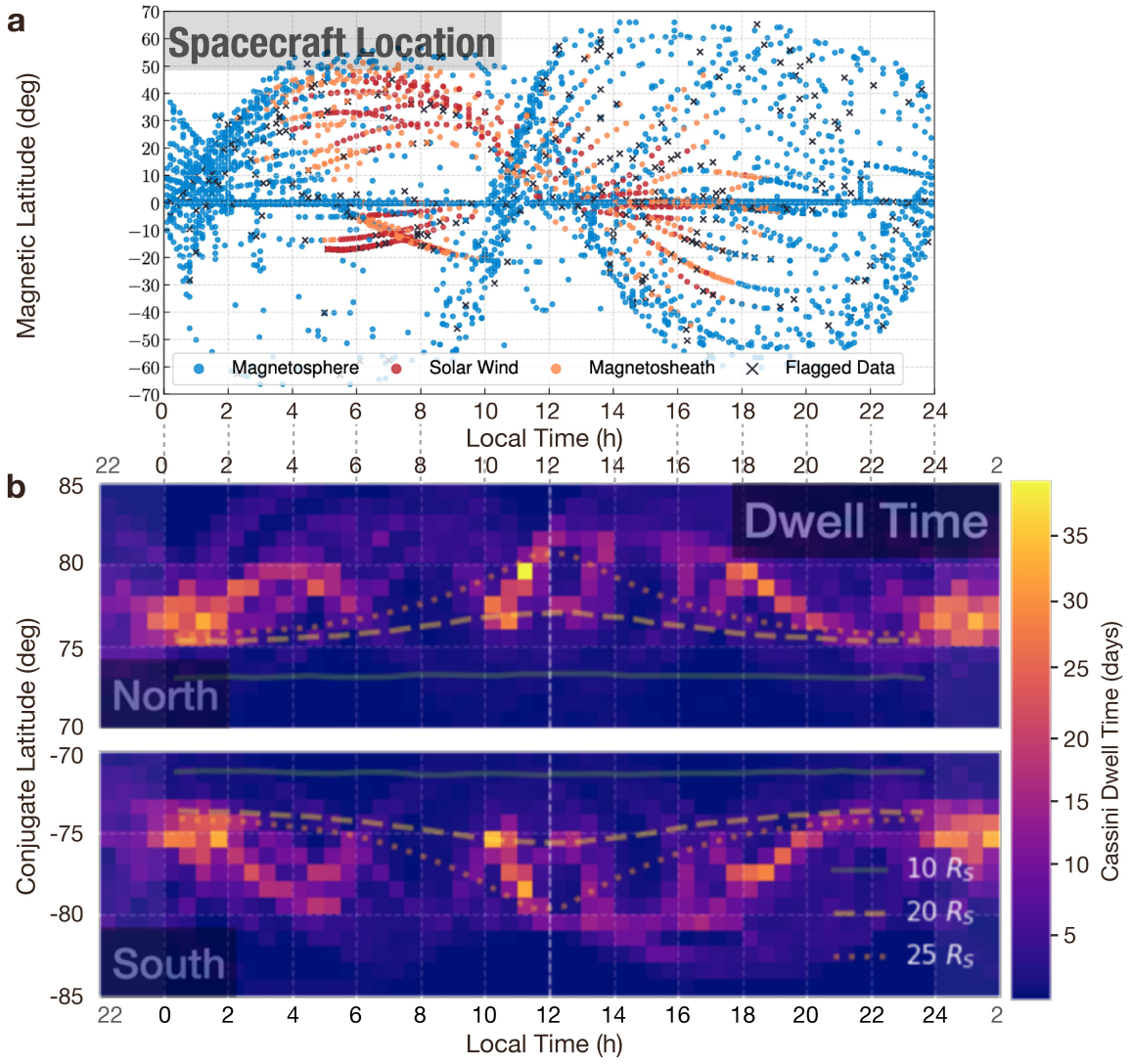

Figure 3.1: (a) The Cassini orbit plotted against local time and magnetic latitude. The colors indicate whether Cassini was in the magnetosphere (blue), the magnetosheath (orange) or the solar wind (red) based on Jackman et al. (2019). Flagged data segments (due to significant data gaps or during calibration times) are marked by black crosses. (b) The time Cassini spent in conjugate latitude and local time bins (see text). The green line gives the position of a shell at 10 R_S, the dashed yellow line a shell at 20 R_S and dotted yellow line a shell at 25 R_S.

latitude mapped to the surface of the planet, and the cumulative Cassini dwell time (in days) in each bin are shown by the color of the bins (Figure 3.1b). The bins extend over 0.5 h in local time and 1° in conjugate latitude. The choice of bin size is a compromise between reasonable resolution and adequate data coverage in each bin. Figure 3.1b clearly displays the asymmetry in local-time coverage seen in the magnetic latitude traces in Figure 3.1a, especially for the 6-to-10-h LT region, which shows the orbiter spending less time at 75 to 80° and −80 to −75° conjugate latitudes in this local time range compared to other local times. The dashed yellow line separates field lines whose equatorial crossing maps outside of $20\,R_S$ from those that map inside. Cassini remains mostly inside the magnetic shell at $25\,R_S$ on the day side (dotted orange line), which is the nominal distance of the nose of the magnetopause. On the night side, Cassini remains outside of $20\,R_S$ most of the time (dashed yellow line). Furthermore, a plot of the Cassini dwell time on typical field lines near the midnight and noon meridians (Figure 3.2), makes it apparent that most of the data come from lower-to-mid-latitudes and that it will be important to normalize cumulative event times by the orbiter's dwell time in different local time-conjugate latitude bins.

Having selected the 36-hour-long data segments that meet our data standards, we transform the data from KSM coordinates into mean-field-aligned (MFA) coordinates to reveal the orientation of the transverse component of the pulsations. Our orthogonal coordinate system is defined by a parallel unit vector along the averaged background magnetic field, $\langle\vec{B}\rangle$, calculated by using a three-hour running average, and a unit vector $\hat{\phi}$ in the azimuthal direction parallel to the kronographic equator ($\hat{\phi}\times\hat{R}$) and positive in the direction of corotation. Saturn is a rotationally dominated magnetosphere, and it is reasonable to assume there will be more symmetry in the azimuthal direction than any other. The other perpendicular unit vector ($b_{\perp 2}$) completes the orthogonal coordinate system. A three-hour-long running average resolves waves of up to approximately three hours, which is adequate resolution for the study of waves with a period of 30 min to 3 h.

The full set of orthonormal vectors for the MFA coordinate system is then:

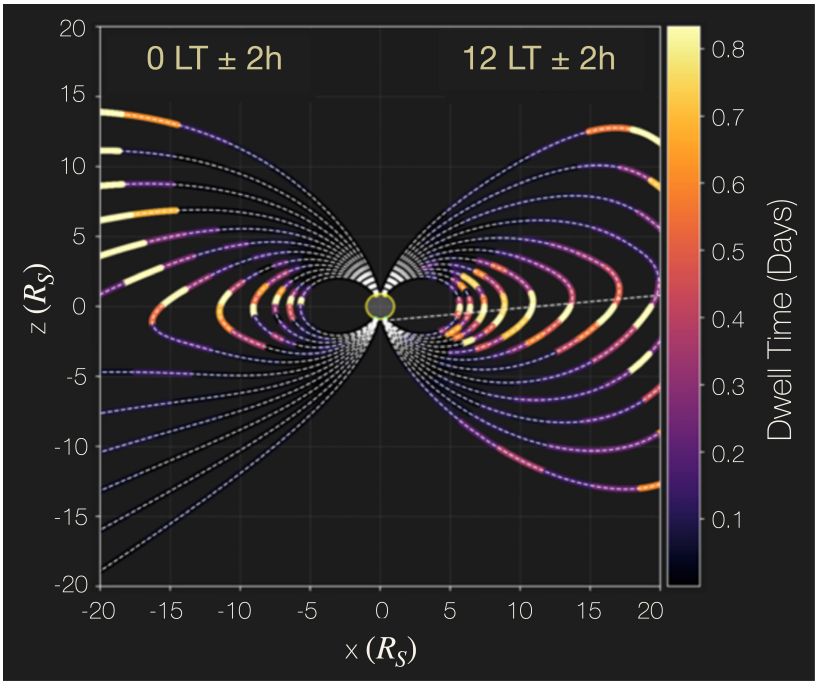

Figure 3.2: Cassini orbiter dwell time, restricted to (0 ± 2) h and (12 ± 2) h LT shown with color in magnetic latitude bins along typical field lines crossing the magnetic equator at different radial distances past $5\,R_{\mathrm{S}}$.

$$\hat{b}_{\parallel} = \langle\vec{B}\rangle/|\langle\vec{B}\rangle| \quad (3.1)$$

$$\hat{b}_{\perp 1} = \hat{\phi} \times \hat{b}_{\parallel}/|\hat{\phi} \times \hat{b}_{\parallel}| \quad (3.2)$$

$$\hat{b}_{\perp 2} = \hat{b}_{\parallel} \times \hat{b}_{\perp 1} \quad (3.3)$$

An example of a typical quasiperiodic wave in field-aligned coordinates is shown in Figure 3.3. Panel 3.3a presents the original MAG data in KSM coordinates, resampled at 1-minute intervals with the background magnetic field ($\langle\vec{B}\rangle$) removed. The Cassini orbiter was on the day-side magnetosphere near the cusp, at around $20\,R_{\rm S}$ from Saturn, and it detected two intense wave trains of ∼60-minute periodicity during the day – one from 7:00 to 12:00 UT and another one shortly after, 16:00 to 22:00 UT. All three components in KSM coordinates – B_x, B_y, and B_z – show clear signatures of 60-minute waves, with smaller amplitudes in B_{tot} during the first interval of activity (panel 3.3a). The MFA coordinate transformation (Figure 3.3b) clarifies that these are mostly transverse perturbations of amplitude 0.2 to 0.3 nT in $B_{\perp 1}$ and $B_{\perp 2}$, with a smaller compressional (B_{tot}) component of amplitude ∼0.05 nT. The peaks of these wave trains are separated by nearly 11 hours, which is close to Saturn's planetary period oscillation (PPO) of ∼10.7 h. We will see below that this is typical of most of the events in the magnetosphere.

Although the measured amplitudes of the QP60 waves in the magnetic field are small (often as low as 0.1–0.2 nT), the Fluxgate Magnetometer had the sensitivity to measure such minuscule perturbations when the sensor was operating in two lowest magnetic field ranges: ±40 nT and ±400 nT, which was true for most of the orbits around Saturn except for those very close to Saturn (Dougherty et al., 2004). The resolutions for these operational modes were 4.9 pT and 0.049 pT, respectively, with the less constrained magnetic field resolution being just sensitive enough to detect 0.1–0.2 nT perturbations.

We quantify the spectral characteristics of the quasiperiodic events by calculating the power density spectrum for individual 36-hour long data segments using a Fourier trans-

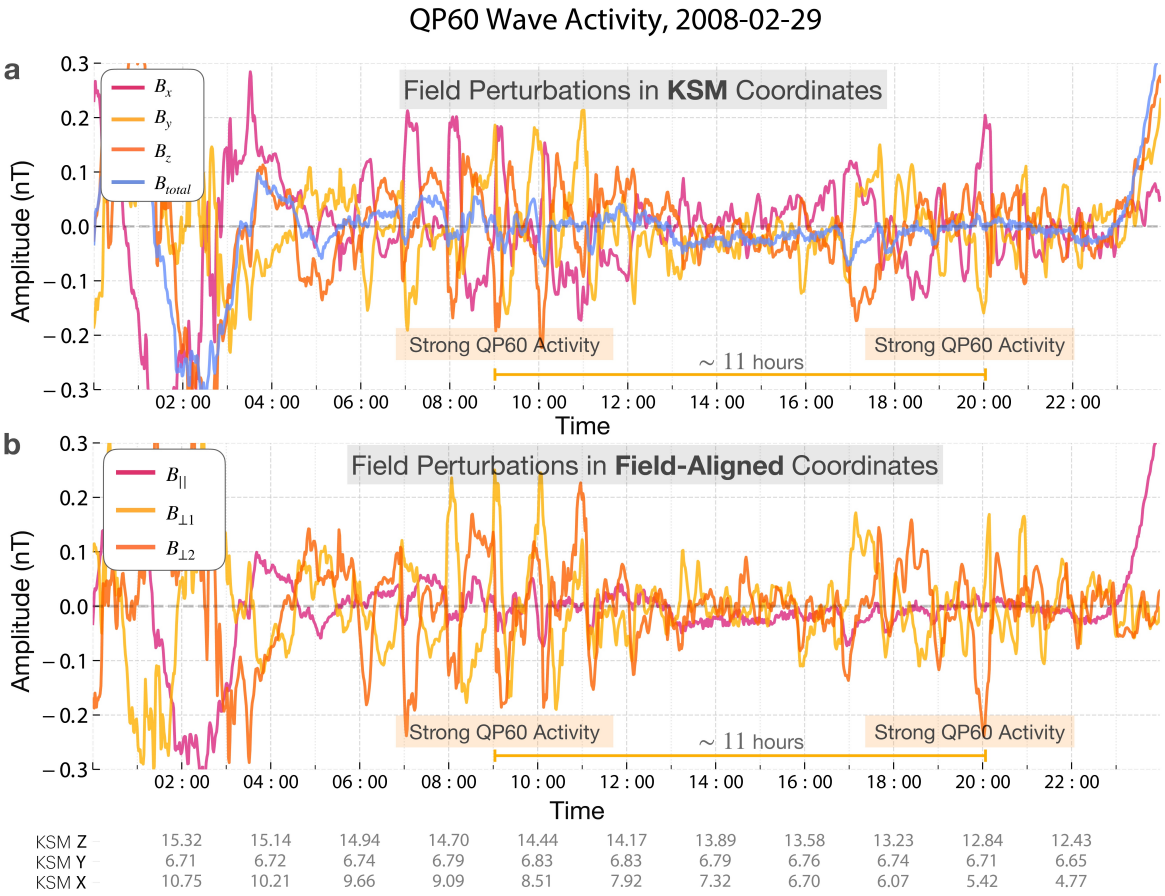

Figure 3.3: (a) Magnetic field perturbations, in KSM coordinates (see text). (b) The same magnetic field perturbations, transformed into a mean field-aligned coordinate system. Two intervals of particularly high amplitude wave signatures are marked as Strong QP60 Activity. An orange line extends over an ∼11-hour interval. Spacecraft ephemeris data (in KSM) are given at the bottom of the plot.

form. With the one-day-long data intervals resampled at one-minute resolution, the Nyquist (smallest to resolve) period is two minutes, and the highest to resolve period is 24 hours. We implement Welch's method of spectral averaging (Welch, 1967) with a data window size of 12 hours and an overlap of 6 hours to decrease the noise, albeit at the expense of diminished frequency resolution due to the shortening of the data segment lengths. We minimize spectral leakage from the frequencies of interest by applying a Hann window function, reducing the power of the spectral sidelobes due to a sinusoidal signal at a small cost to the frequency resolution. The Hann function decays to zero on both sides of the data segment, thereby rendering the correlation between the overlapping data segments negligible. Our method reduces the maximum period resolved to 12 hours, well beyond the range of the wave periods of interest, i.e., 30 min to 3 h, while still preserving good frequency resolution. An example of a data segment with QP60 power is shown in Figure 3.4b. The background power estimate is calculated only over frequencies corresponding to periods of 30 minutes to 4 hours. We used synthetic magnetic field data with sinusoids of varying periodicity between 30 minutes and 2 hours to determine the optimum averaging window. Then we calculated a ratio of each component's power density to the background power density estimate of the total field, $P(\langle B_T \rangle_f)$:

$$r_i = \frac{P(b_i)}{P(\langle B_T \rangle_f)}, \tag{3.4}$$

where r_i is the ratio of the power in the ith component ($b_\parallel$, $b_{\perp 1}$, $b_{\perp 2}$) to the power in the total field (B_T) at frequency f, $\langle B_T \rangle_f$ is the background field estimate of B_T, $P(b_i)$ is the power in the ith component of the field and $P(\langle B_T \rangle_f)$ is the power in the smoothed background field estimate $\langle B_T \rangle_f$, for frequencies corresponding to the period range of 30 to 180 min.

The motivation for examining ratios is that it is easier to identify the signatures of the QP60 waves by plotting the ratio of powers, r_i, than by plotting the power spectra themselves (see Figure 3.4 for an example).

The Fourier spectral analysis technique allows us to identify data intervals with detectable power at the periods of interest but does not provide optimal time and frequency resolution, mainly because the quasiperiodic waves are discontinuous (non-stationary), varying in frequency and amplitude, and non-sinusoidal. For these reasons, it is appropriate to implement a wavelet analysis to characterize the times of intermittent wave activity and improve on the frequency resolution of the Fourier spectral analysis. Wavelet analysis is advantageous compared with classical Fourier analysis in that it unfolds a time series not only in frequency but also in time, which is especially useful when the signal is non-stationary, as in our quasiperiodic events. For our continuous wavelet transform, we choose a Morlet wavelet (Mallat, 2009; Yates et al., 2016) with a kernel function, $\psi(t, \omega)$, expressed as:

$$\psi(t, \omega) = c_w \exp(-t^2/\sigma^2) \exp(i\omega t), \tag{3.5}$$

where c_ω is a normalization factor, and σ is the temporal width of the kernel.

The Morlet kernel function is essentially a sine wave tapered by a Gaussian, suitable for intermittent perturbations in the field. By varying the wavelet's temporal width (or stretch), a continuous wavelet transform can show the time scale (and correspondingly, the frequency) at which an individual pulse most closely matches the wavelet. Furthermore, it provides very high resolution in the time domain, unlike the Fourier transform. Even a Short-Time Fourier Transform, designed to mitigate the problem of irregular, non-sinusoidal pulses, does not provide good resolution in the time domain (Sinha et al., 2005).

In addition to identifying the characteristic time scales of the wave trains that we are examining, we calculate the cross-correlation between the two transverse components of the perturbations, $b_{\perp 1}$ and $b_{\perp 2}$. The maximum of the cross-correlation function indicates the phase shift with which the signals are best aligned. More precisely, the time delay between the two signals, τ_{delay}, is determined by the argument of the maximum, i.e.

$$\tau_{delay} = \text{argmax}_{t\in\mathbb{R}}((f \star g)(t)) \tag{3.6}$$

where f and g are continuous functions of the two transverse components, and their cross-correlation is defined as

$$(f \star g)(\tau) = \int_{-\infty}^{\infty} f^*(t)g(t+\tau)\,dt \tag{3.7}$$

The time delay between the two signals allows us to calculate the polarization of the quasiperiodic waves.

3.3 Results

We calculated the ratio of the power in each magnetic field component in mean-field-aligned coordinates to the power in the background field estimate (equation 3.4). Evaluating the power in components relative to the power in the field magnitude preserves the relative strengths of the power in the components, allowing a comparison of the compressional and transverse perturbation power. Figure 3.4 illustrates the approach for a 24-hour-long data segment on Jan 2, 2007. Panel 3.4a shows the magnetic field perturbations in field-aligned coordinates, smoothed with a three-minute running average and reevaluated at one-minute resolution for equal data spacing. The data show three wave trains that last for 4 to 6 h, centered at 04:00 UT, 15:00 UT, and 23:00 UT, with the most significant perturbations of $\sim$0.2 nT being in the transverse $B_{\perp 1}$ and $B_{\perp 2}$ components. Panels 3.4b and 3.4c show the power densities and the power ratios, r_i, respectively, for each component and for the power in the total field relative to $P(\langle B_T \rangle_f)$. A ratio of one means that the power at the selected frequency is equal to the background power estimate, and anything above it means the component has more power than $\langle B_T \rangle_f$. It is clear from ratios plotted in Figure 3.4c that the power in the transverse components is of order 100 times the power in the smoothed

background, and the peak power near 60 min is easier to distinguish than in the original power density plot (Figure 3.4b).

We group the 24-hour power ratios ri into local time quadrants. The medians of the power ratios and the upper and lower quartiles are shown in Figure 3.5 for four quadrants: (a) (0 ± 3) h, (b) (6 ± 3) h, (c) (12 ± 3) h, and (d) (18 ± 3) h (see the movie S2 for power ratios obtained for other local time ranges). Significant power is present in the transverse magnetic field components at all local times, but the highest relative transverse power of QP60 waves is found in the midnight sector (0 ± 3) h (see Figure 3.5a). The median power peaks at around 50-minutes, close to the ∼60 minutes previously reported, and the period at which the power peaks vary little with local time. At midnight, the transverse power for QP60 waves is nearly 10 times greater than the compressional power, and it is at least 2-to-5 times stronger at other local times. Also, there are significant peaks in power near 30 min and near 2 h in all quadrants, indicating that multiple harmonic modes are present in the transverse magnetic field fluctuations. We will refer to the additional power peaks as the QP30 and QP120 waves, respectively, in the rest of the paper. Since we used a 3-hour running average for the transformation to mean field-aligned coordinates, we cannot resolve the power of waves with periods greater than 3 hours. There is also significant power in the transverse perturbations at frequencies corresponding to periods below 30 min, which probably relate to higher harmonics ($m > 6$), but we excluded such low-period waves from our study because we used data of 1-min resolution.

We next consider whether the three dominant magnetic perturbations – the QP30, QP60, and QP120 waves – arise as harmonics of standing waves on magnetospheric flux tubes. Figure 3.6 contains plots of frequency vs. conjugate latitude of harmonic eigenmodes of field line resonances calculated for a model magnetosphere with a realistic magnetic field and plasma density (Rusaitis et al., 2021). The solid-colored lines represent the frequencies of toroidal eigenmodes in the noon-midnight meridian for modes 1 to 6 in the model; the modes calculated on the dayside are on the left and those for the nightside are on the right. The

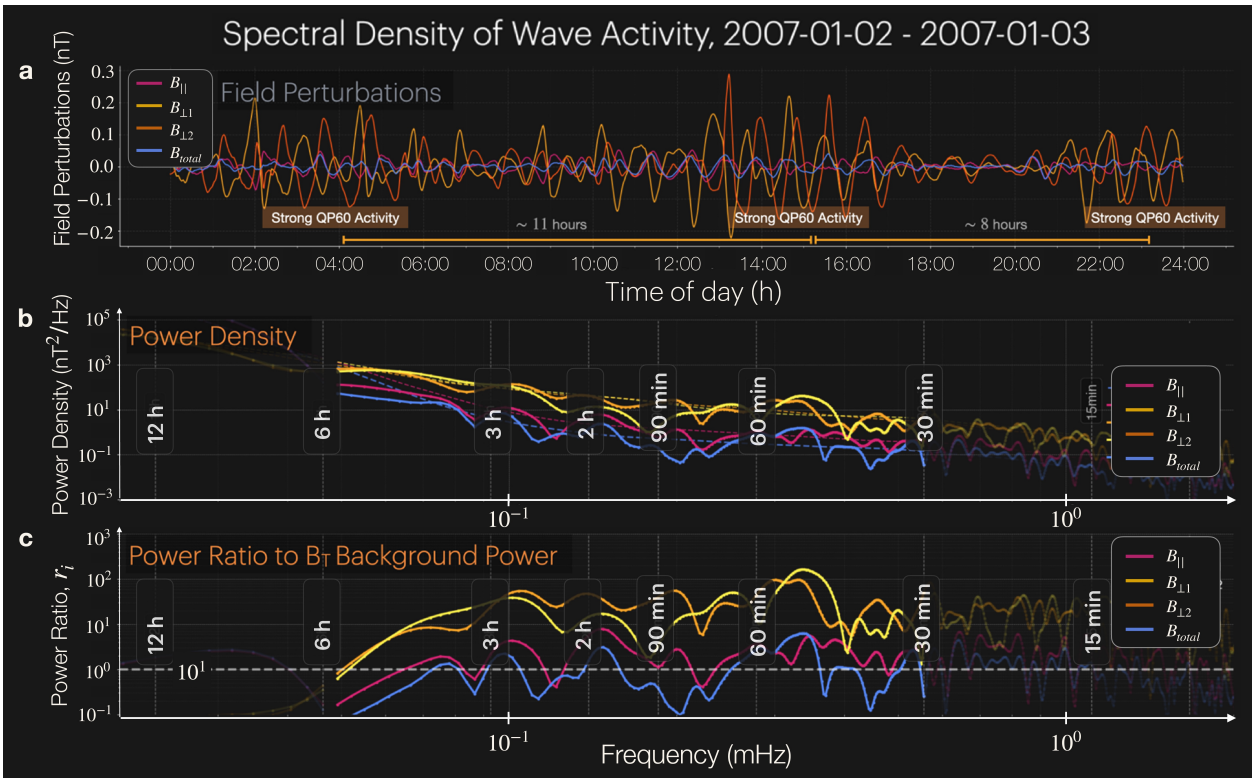

Figure 3.4: (a) Magnetic field perturbations in a mean field-aligned coordinate system and (b) power density for the magnetic field. The colored dotted lines give the estimate of the background power density for the components and the magnetic field magnitude (see text) and (c) gives the ratio of the power density in each component to the background power in the total field. Periods of interest are overlaid in the bottom two panels with dashed vertical lines. The colored dashed lines in panel b represent estimates of the background power density curves in the 30 min to 6 h range.

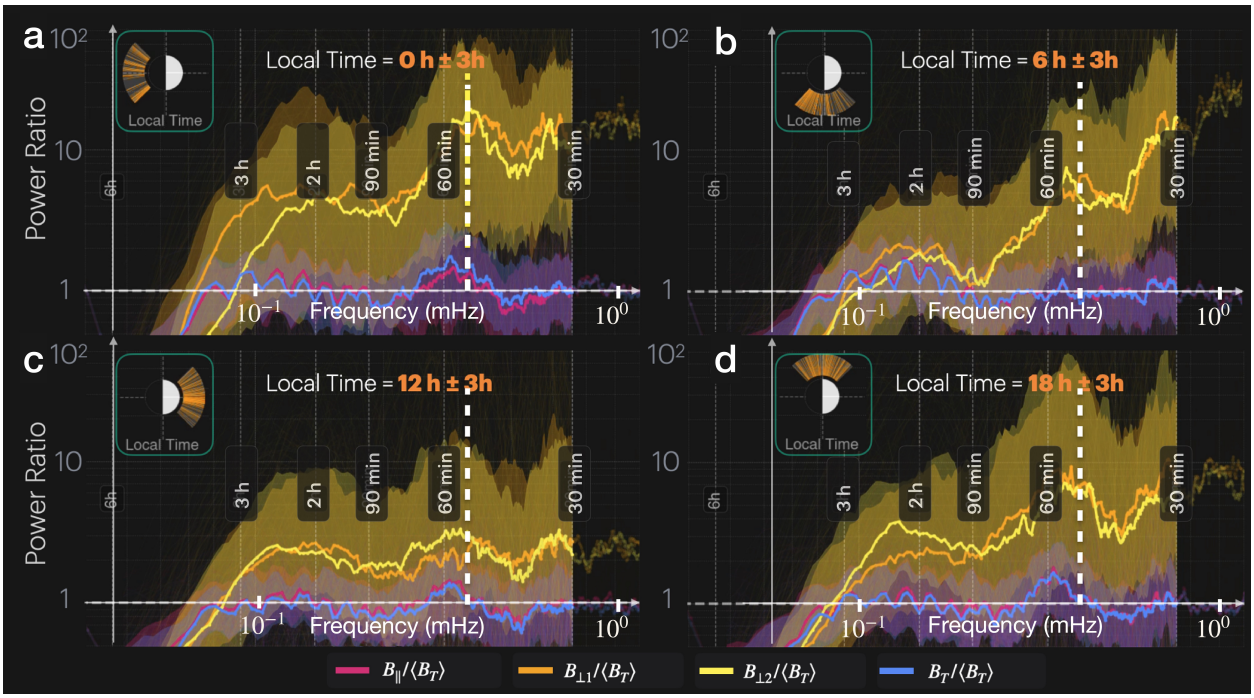

Figure 3.5: Median power ratios of magnetic field perturbations in mean field-aligned coordinates as defined in the text, with solid color lines plotted versus frequency for different ranges in local time: a) local time of (0 ± 3) h, b) local time of (6 ± 3) h, c) local time of (12 ± 3) h, d) local time of (18 ± 3) h. The lower and upper quartiles for each power ratio are shown as the bottom and top of the shaded areas. Periods corresponding to selected frequencies are labeled on the panels. The white dashed lines show the frequency corresponding to 50 min period, the period of the peak in the 0 h LT bin.

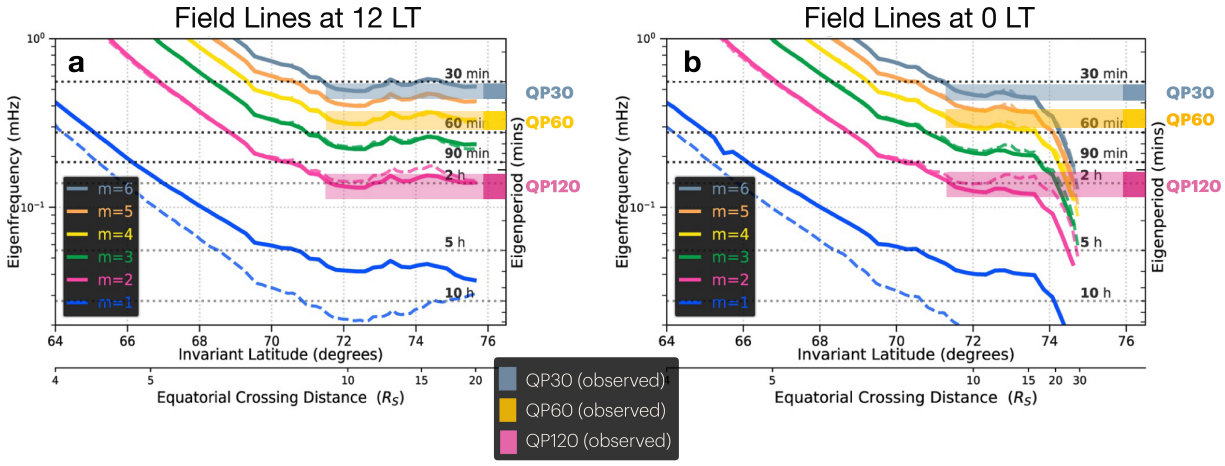

Figure 3.6: Eigenfrequencies for field line resonances in the 12 LT (a) and 0 LT (b) meridians (adapted from Rusaitis et al., 2021). The power spectral peaks for the dominant waves in the Cassini magnetometer data are superposed by using solid-colored bars: QP30 (grey), QP60 (yellow), and QP120 (magenta).

poloidal modes are shown as dashed lines of corresponding color, and for the harmonics above the fundamental, the poloidal frequencies do not differ much from the toroidal frequencies (solid lines). The three dominant frequencies of the observed transverse magnetic power density are overlaid as semi-transparent color rectangles and correspond closely to the even modes of FLR eigenmodes: $m = 2$ for QP120 (magenta), $m = 4$ for QP60 (yellow), and $m = 6$ for QP30 (grey). The comparison with observations is limited to invariant latitudes between 72 to 76° at noon and between 72 to 74° at midnight. These field lines cross the equator between 10 and 20 R_S where the plasma density model is valid, and there are significant observational data from the Cassini orbiter.

Since Cassini did not sample Saturn's magnetosphere uniformly, we normalize the occurrence frequencies to the orbiter's dwell time in discrete regions of the magnetosphere in order to establish the probability of occurrence in different sectors. We find that the event occurrence rate typically peaks at latitudes of 40 to 60° (Figure 3.7), except in the dawn sector where the event occurrence rate near the equator (Panel 3.7b) is significant. The plasma

sheet is expected to be thinner at dawn than at noon and dusk due to a strong stretching of the field at dawn and subsequent dipolarization of the field at noon (Jia & Kivelson, 2016). Thus, the higher event rate at equatorial dawn would be surprising if it we did not take into the account the bias in the orbiter's residence time in the plasma sheet. By counting the dwell time in a weak magnetic field of 2 nT less with an orientation of $\pm 30^\circ$ to the magnetic equator, we estimate the orbiter's residence in the plasma sheet. We find a dawn bias of residence time compared to other local times, especially during the southern solstice, which may partially account for the higher event rate at the dawn equator. There is also a larger event detection rate in the southern hemisphere compared to the north by a factor of 2 to 3, except at noon. During the southern summer season, the southern hemisphere is expected to have a higher Pedersen conductance than the north by a factor of 3 (Jia & Kivelson, 2012). However, the seasonal changes in the conductivities of the hemispheres and the effects of such north-south asymmetries on the field line resonances are not yet fully understood.

The bias towards high magnetic latitude occurrences is compatible with the field line resonance model because in the non-uniform field and plasma conditions of Saturn's magnetosphere, the magnetic amplitudes of the eigenmodes peak at high latitudes (see Figure 3.2b, Rusaitis et al., 2021, for a model field line crossing the equator at $20\,R_S$). This property implies that the waves are more readily detectable at high magnetic latitudes. The amplitudes of the magnetic field perturbations, indeed, become comparable to or larger than those at the equatorial plasma sheet above $\sim 60^\circ$ latitude where the event occurrence is high. At the magnetic equator, however, the occurrence rate is low, except at dawn, but that may be due to the nodes of the harmonics being tightly confined within the thin plasma sheet ($\pm 10^\circ$ latitude), as in the model. During Cassini's nominal mission between 2004 and 2008, the plasma sheet was bent in a bowl shape due to the interaction with the solar wind (Arridge et al., 2008), leaving most of the equatorial orbits below the plasma sheet. Multiple crossings of the plasma sheet were recorded in 2006, but the orbiter spent only a small fraction of the time within the thin current sheet (Arridge et al., 2011). Since individual passes through

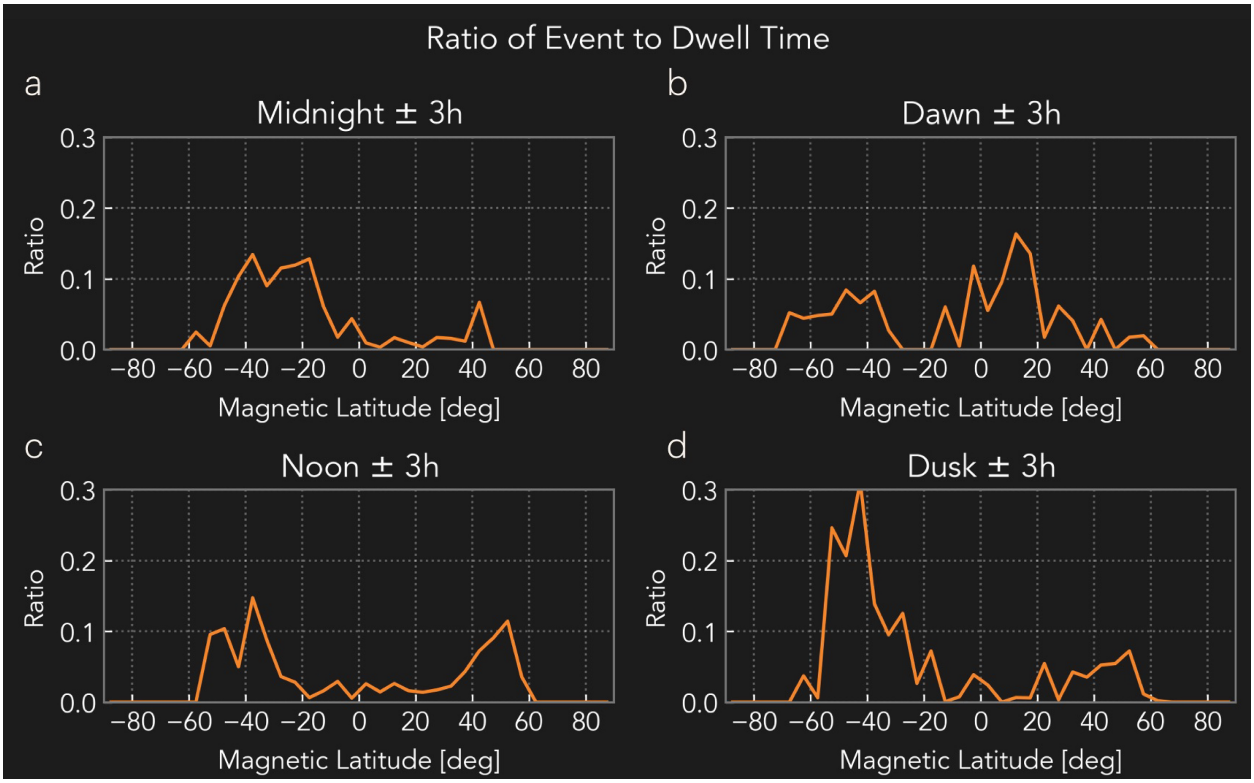

Figure 3.7: Ratio of cumulative event time to orbiter dwell time against magnetic latitude for four local time sectors: (a) (0 ± 3) h LT, (b) (6 ± 3) h LT, (a) (12 ± 3) h LT, (a) (18 ± 3) h LT.

the sheet frequently last less than 2 h, it is not possible to detect at least four continuous oscillations of standing Alfvén waves on all passes (see, e.g., Figure 9, Arridge et al., 2011). As for the occasional times when Cassini was fortuitously within the thin current sheet for a longer interval, it would have had to present at the right phase of the 10.7-hour cycle to detect multiple periods of the QP60 events.

Normalizing the cumulative event time in local time–invariant latitude bins by the time spent in each bin, we find the occurrence rate is highest on the dusk-side by a factor of two, and lowest in the morning region of 6 to 10 LT (Figure 3.8). This asymmetry in local time has been reported previously (Roussos et al., 2016; Palmaerts et al., 2016). The asymmetry may arise because Cassini dwelt on closed field lines for longer intervals on the dusk side than on the dawn side. To investigate, we used the Khurana field model with nominal IMF and solar wind conditions to calculate the cumulative time Cassini spent on closed magnetic flux tubes (see the Methods section 3.2) in different local time–magnetic latitude bins. The fraction of time that Cassini was on closed field lines was lowest in the morning sector between 6 and 10 LT. At mid-to-high latitudes of 40 deg and above, the spacecraft had the highest residence time fraction on closed field lines post-dusk. Therefore, we suggest that Cassini would have fewer QP60 observations in the morning sector because it spent a smaller fraction of its dwell time on closed field lines.

The quasiperiodic perturbations in the magnetic field typically come in short bursts with amplitudes of 0.1 to 0.5 nT for 4 to 6 h before decaying and amplifying again, with peaks in power separated approximately by 11 hours, as seen in the examples in Figure 3.3 and Figure 3.4. We estimated the separation in time between consecutive bursts by finding separations between times of peak power in the wavelet transform matrix. A histogram of the wave train separation times shows a distribution skewed towards longer separations with a median of 10.73 h (Figure 3.9). There is a minor peak at $\sim$21 h. This longer time separation of wave packets could be explained if an intervening packet was too weak to detect by our method, or if the orbiter was passing through regions of the magnetosphere that are not favorable for

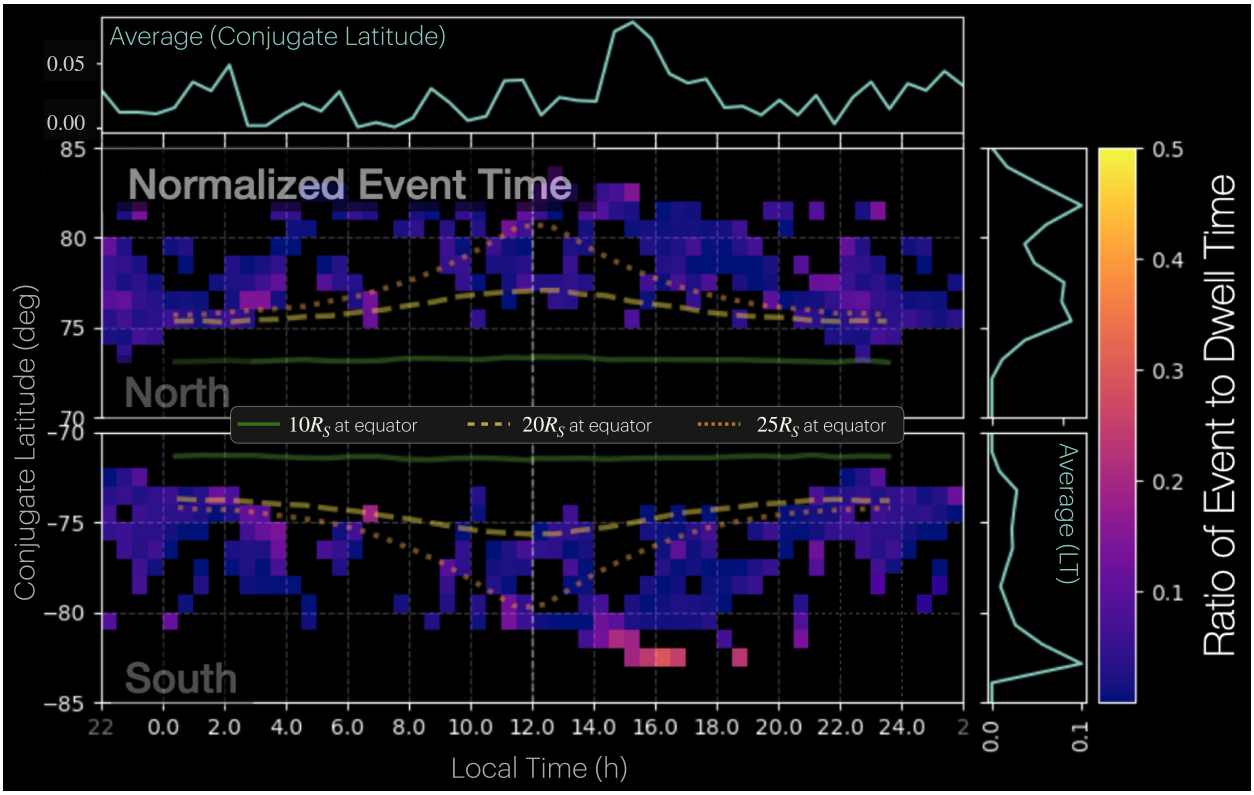

Figure 3.8: Ratio of normalized QP60 cumulative event time to Cassini dwell time in local time – conjugate latitude bins. The cyan lines are averages in local time (top) and conjugate latitude (right).

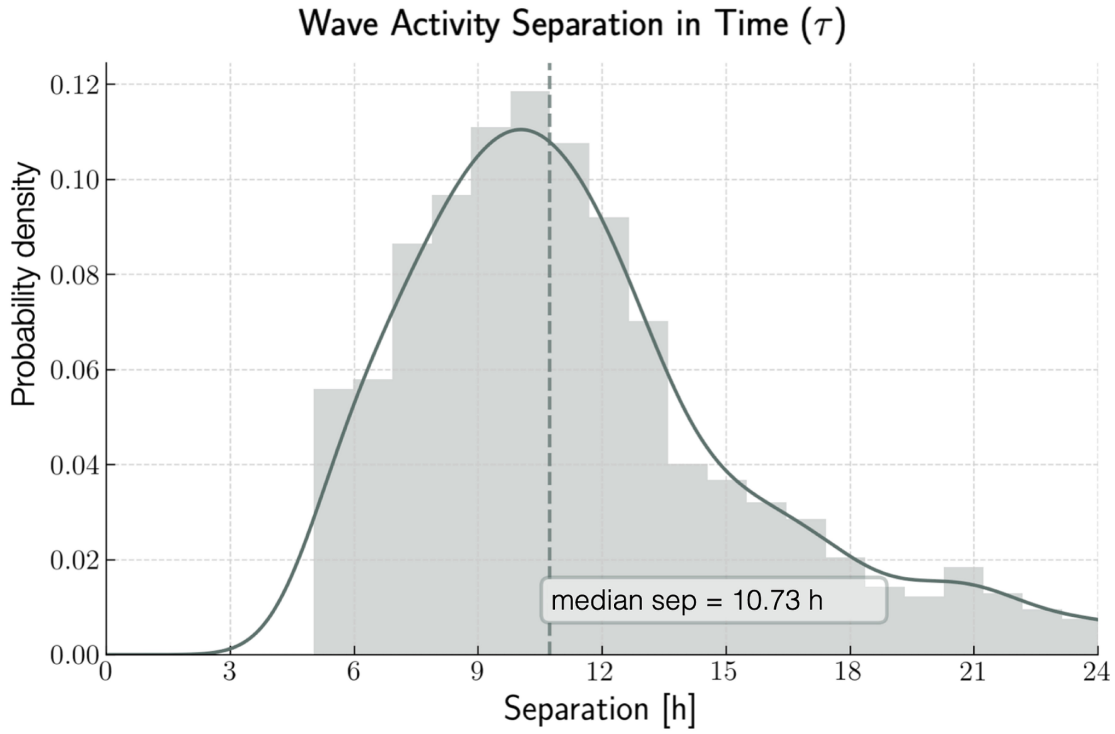

Figure 3.9: Normalized probability distribution of wave train separation time for (60±10) min waves (thick gray line), and the original histogram used for the calculation of the probability distribution (gray bars). The median separation of 10.73 h is shown with a vertical dashed line.

observing the waves, leading to a detection of consecutive events separated by ∼21–22 h.

We calculated the cross-correlation of the transverse components of the perturbation field (equations 3.7) to determine the polarization of the quasiperiodic waves. Two typical examples of cross-correlation of QP60 waves are shown in Figure 3.10. Panels 3.9a-b show two wave trains (seen in the field perturbation plots) with mainly a 90° phase shift and panels 3.9c-d show three wave trains with 90, 180 and 180° phase shifts, respectively. Most of waves we studied have a 90° phase shift between the transverse components as in Figure 3.9a, implying the waves are predominantly circularly polarized.

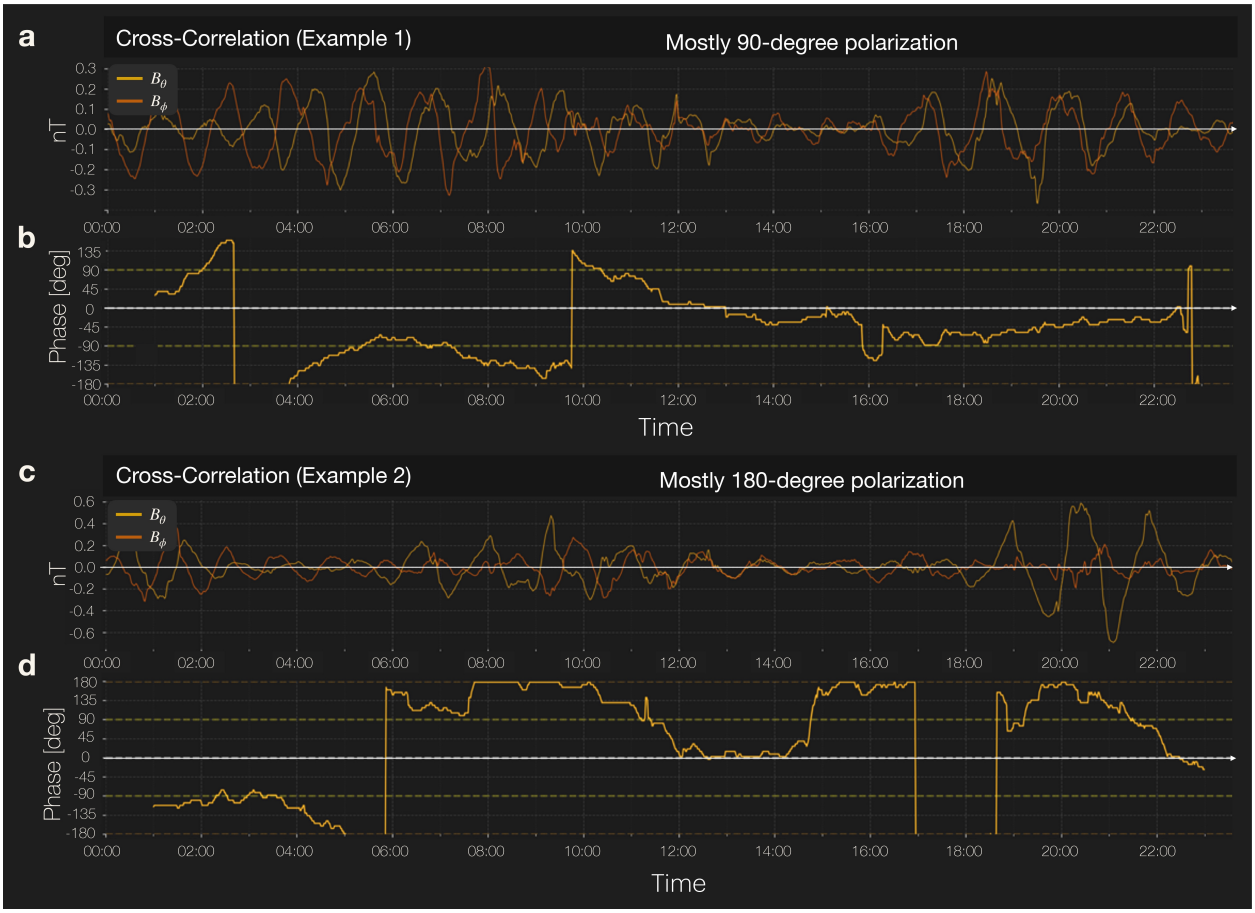

Figure 3.10: Cross-correlation between the two components perpendicular to the background field ($b_{\perp 1}$ and $b_{\perp 2}$), shown for two sample data intervals. Panel (a) gives a time series plot for the first example, with the cross correlation for that interval plotted in (b). The cross-correlation shows mostly a 90° phase difference (circular-polarization, most common). Panel (c) gives the time series for the second interval. The cross-correlation for the second interval in (b) has mostly a 180° phase difference (linear polarization).

3.4 Discussion

We have undertaken a comprehensive study of quasiperiodic waves of periods between 30 min and 3 h in the magnetic field data spanning all the Cassini orbits within Saturn's magnetosphere. The highest observed power is found for waves at 60-min period (QP60) with relatively high power also in 30-min (QP30) and 120-min (QP120) waves. The periods match the even harmonics in a realistic field line resonance model (Rusaitis et al., 2021). The highest transverse power relative to the compressional component is found in the pre-midnight sector, indicating that the post-dusk region is important for the initiation of these waves. The QP waves are typically observed in 4-to-6-h long wave packets, reoccurring once a PPO cycle of ∼10.7 hours. The consistent modulation of the waves at this period highlights the importance of the PPO-generating mechanism for QP waves. We suggest that impulses that drive the periodic flapping of the magnetotail at the PPO period in the post-dusk sector are responsible for the excitation of even-mode field line resonance harmonics.

Our study matches some of the previously reported characteristics of the QP60 waves in several types of magnetospheric data. In the energetic electron injection and plasma data, the frequency and wave packet duration of the quasiperiodic waves closely match the values found in our study (Roussos et al., 2016; Palmaerts et al., 2016; Carbary et al., 2016). They were observed at all local times, and over a wide range of radial distances and latitudes, mostly on closed field lines. The occurrence rates were highest in the dusk sector and lowest in the pre-dawn region of (3 ± 2) h LT. The probability of the events, as well as the growth and decay rate of amplitudes in the coincident auroral hiss waves were highest at mid-to-high latitudes, both in the particle and plasma data. Palmaerts et al. (2016) suggested this may be indicative of a high latitude source for the energetic electron emissions and hiss waves. Coincident oscillations in the B_ϕ component of the magnetic field were also observed ∼20 % of the time, especially at mid-to-high latitudes (Palmaerts et al., 2016). Independent studies of the QP60 waves in the magnetic field showed the waves to be mostly Alfvénic with

amplitudes of 0.1 to 0.5 nT (Dougherty et al., 2004; Bunce et al., 2014; Mitchell et al., 2016; Kleindienst et al., 2009; Yates et al., 2016). The occurrence rate was found to be highest near noon and at high latitudes, though secondary peaks were observed pre-and-post midnight (Pan et al., 2021). The spectral study by Pan et al. (2021) found the wave power to be rapidly decreasing beyond 25 R_S in the dawn and noon sectors, indicating that they are unlikely to be generated at the magnetosheath or magnetopause boundary. The wide-spread occurrence of QP60 waves with local time and radial distance in several types of the magnetospheric data, coupled with a notable dawn-dusk asymmetry, suggests existence of several different excitation mechanisms, whereas the observed frequencies, decay and reoccurrence rates are characteristic of the general configuration of Saturn's field, plasma density, and PPOs that change slowly with time.

The properties of quasiperiodic oscillations identified in our study differ in some ways from those found in other magnetospheric data. Notably, the reoccurrence of the wave packets is more frequent and periodic than that observed in the electron injection and plasma data. Electron flux oscillations were observed every ∼4 days in the dusk sector and every 40 days in the dawn sector (Palmaerts et al., 2016). The plasma waves in the 100 Hz band together with QP60 waves were seen even less frequently, averaging ∼1 event per month over an 11-year period, almost solely at high latitudes (Carbary et al., 2016). As observed by Palmaerts et al. (2016), coincident QP60 signatures in the plasma and magnetic field data with the electron injections occurred less than a quarter of the time. These different QP60 signatures seem to be related, but were not reported to be coincident most of the time. It is likely that many quasiperiodic magnetic perturbation events of small magnitude (0.1 nT and less) were missed in the previous studies. Faint signatures of the perturbations are easy to miss by visual inspection, or even in Fourier transforms due to their intermittent nature. Our wavelet analysis procedure, which computes the power ratio in each frequency band to that of the background estimate, allows for identification of much weaker oscillation signatures. In order to reduce the number of missed events, we also use overlapping data segments (see Methods

section 3.2) to be able to detect 6-hour-long events at the start or end of each data interval. We find the QP60 perturbations in the magnetic field are observed frequently, usually every PPO cycle, including at equatorial latitudes. The modulation of the magnetic perturbations at the PPO period has been noted previously before for select intervals by Yates et al. (2016), and our analysis shows this to be true for the duration of Cassini's residence at Saturn.

The second main difference between our study and other surveys of the QP events is that we investigated a wider range of selected wave periods than has been previously analyzed and we report on the occurrence of QP30 and QP120, in addition to QP60 waves. The longer periods have not been reported in the particle or plasma data, possibly because they have been outside the focus of most studies. For example, the quasiperiodic electron injection surveys by Roussos et al. (2016) and Palmaerts et al. (2016) were limited to periods of 40 to 80 min. The auroral hiss emission study by Carbary et al. (2016) accepted a wider period range of 40 to 120 min, but the overall event count was low (138) and required a visual examination of a smoothed 100 Hz profile in time that could miss the weaker signatures of the QP120 waves if present. A more recent statistical survey of magnetic field fluctuations by Pan et al. (2021) did find significant power ranging from 30-to-60 min, with minor peaks near 30 and 50 min, but the survey used a cut-off at a period of 60 min. Although we find that the QP30 waves to have similar power to QP60 waves (Figure 3.5), they tend to occur simultaneously with the QP60 waves of varying power, and thus may be hard to resolve, especially by visual inspection. The QP120 waves, in comparison, have much weaker transverse power than both the QP30 and QP60 waves and are accordingly even harder to detect.

We argue that the post-dusk region is important for the generation of the quasiperiodic waves for several reasons. First, MHD simulations of Saturn's magnetosphere show a larger region of closed magnetic field lines post dusk than post-midnight (Jia, Hansen, et al., 2012; Ramer et al., 2017). That Cassini was resident on closed-field lines more frequently post-dusk than at other local time, potentially explains the higher observed occurrence rate at dusk,

but not the higher transverse magnetic perturbation power post-dusk. Secondly, we find that events occur typically once per PPO cycle in the region where the changes in the magnetic field configuration at a PPO period are particularly large in the simulations (Ramer et al., 2017). Although the PPO period has been observed to differ slightly between seasons and northern and southern hemispheres, our median event separation of 10.73 h (Figure 10) is a close match to the known PPO period range of 10.6 to 10.8 h (Galopeau & Lecacheux, 2000; Gurnett et al., 2005, 2007; Jia & Kivelson, 2012; Provan et al., 2016; Hunt et al., 2014, 2015). The proposed vortical asymmetric flows adopted by Jia, Kivelson, and Gombosi (2012) generate field-aligned currents and associated pressure pulses that drive many of the observed PPO signatures in the magnetic field. This leads to global-scale compressions and expansions (termed breathing by Ramer et al., 2017), as well as north-south motion of the magnetotail (flapping) at the PPO period of 10.7 h. The flapping motion is most intense post-dusk and beyond 15 R_S, a region where most of the QP60 magnetic perturbations are observed (between ∼10 and ∼30 R_S. The azimuthal and radial flows end up stretching the equatorial segments of the flux tubes, but this leads to perpendicular components of the perturbation field that are antisymmetric about the equator (see Jia, Kivelson, & Gombosi, 2012, Figure 4). We propose that the vertical flapping of the magnetotail once a PPO cycle excites the even, but not the odd harmonics of the field lines.

Models of field line resonances in realistic field and plasma configurations match many observed QP wave characteristics (Rusaitis et al., 2021). The even-mode harmonics match the observed periods of QP30, QP60, and QP120 waves (Figure 3.6), and the eigenfrequencies vary little with distance and local time in the outer magnetosphere between 10 and 20 R_S. Furthermore, the magnetic perturbation amplitude is highest on the portions of flux tube closer to the ionosphere (magnetic latitude >60°), compatible with higher observation rates at mid-to-high latitudes. Nevertheless, events near the equator are observed, though less frequently. Since the nodes of the harmonics of field line resonances are tightly confined within the plasma sheet (within ±10° magnetic latitude), and the current sheet is expected

to be flapping and stretching (Ramer et al., 2017), Cassini is unlikely to be resident within the plasma sheet for long intervals of time (Arridge et al., 2008, 2011). As mentioned before, the plasma sheet was often bent into a bowl shape, and intermittent encounters with the plasma sheet at equatorial orbits were rarely longer than 1 or 2 hours (Arridge et al., 2008, 2011). This would make the detection of at least 4 continuous oscillations of ∼1 h waves rare but could potentially explain the high relative transverse power we observe in the 30 min waves at low latitudes, sometimes higher than the QP60 equivalents. Lastly, the temporal variability of Saturn's magnetosphere prevents the observed field line resonances from being as narrow banded as in the model. The varying density of the equatorial plasma sheet (Provan et al., 2012) potentially explains why the wave periods observed are not fixed but vary by ∼20 % or more.

Several questions regarding the quasiperiodic fluctuations in the magnetic field remain unanswered. Although we argue that the stretching and flapping of the magnetotail lead to kinked field lines with an anti-node just off the equator, suitable for triggering of the even-mode harmonics, this does not explain why the odd harmonics are not produced by other triggers. One such trigger could potentially be the periodic global contractions and expansions of the field by the PPO-generating mechanism. The absence of odd-mode harmonics in the data lead us to conclude that they are either not excited or are too weak for our detection algorithm. Secondly, the QP30 and QP120 waves reported in this study were not found in the previous surveys of magnetospheric data, but as mentioned already, this may be due to the selection criteria used in previous studies. Therefore, it would be useful to extend the global QP60 surveys of Roussos et al. (2016) and Palmaerts et al. (2016) to a wider frequency range. We also observe more frequent observations of the QP60 waves in the southern hemisphere. The effects of the seasonal variation of the ionospheric Pedersen conductance, as well as the asymmetry in the conductances between the hemispheres on the observed field line resonances and the higher southern-hermisphere observational rates, remain to be studied.

We found a higher occurrence rate of events in the southern hemisphere over the whole Cassini mission at Saturn (Figure 3.7) and have not accounted for that difference. A future study accounting for effects of the north polar shift of the effective dipole (Smith et al., 1980) and the difference in solar illumination in the two ionospheres on the ionospheric conductance and field line resonances would be worthwhile. The connection of the QP events to magnetic reconnection phenomena also remains unclear. It has been noted that the locations of QP60 waves trace to sites where reconnection is expected to take place (Roussos et al., 2016), but the connection has not been causally established. Delamere et al. (2015) found the highest rate of magnetodisk reconnection at dusk, but the apparent collocation of QP60 waves may be coincidental. Of course, recognizing that there are multiple ways to excite resonant waves, it is also possible that the periodic flapping of the magnetotail is only one of the triggers of the QP perturbations. Other mechanisms linked, directly or indirectly, to magnetopause or magnetodisk reconnection, Kelvin-Helmholtz instabilities, or solar-wind induced storms may be operating, as suggested by Roussos et al. (2016). However, since the power of the QP60 oscillations in the magnetic field diminishes quickly beyond $25\,R_{\mathrm{S}}$ (Pan et al., 2021), most of the events are likely to be driven internally rather than externally to the magnetosphere.

The striking periodic modulation of the QP waves in the magnetic field at the PPO period suggests that one of the leading mechanisms for the generation of the waves is the flapping motion of the stretched dusk-side magnetotail. We detect three frequency bands in the magnetic field data of significant power that we label as QP30, QP60, and the QP120 waves, and classify them as even-mode harmonics of field line resonances as in the model of Rusaitis et al. (2021). QP60 waves, being the most powerful, have been previously linked with various other signatures in the energetic electron data, ion conics, auroral pulsations, and plasma waves. It remains to be seen if these signatures are present only in the magnetic field data or are detectable in other magnetospheric data.

CHAPTER 4

Frequencies of ULF waves in realistic models of the terrestrial magnetosphere

4.1 Introduction

The truth is rarely pure and never simple.

— Oscar Wilde

Magnetohydrodynamic (MHD) waves with frequencies ranging from roughly a mHz to a few Hz are routinely observed in Earth's magnetosphere by in-situ instrumentation and ground-based magnetometers. Ultra-low frequency (ULF) waves in this frequency range are commonly known as Pc1-Pc5 waves, corresponding 0.2 to 600 second period (Jacobs et al., 1964). Pc3-5 ULF waves have fundamental wavelengths of the order of the magnetospheric cavity and are important mediators of energy and momentum transport in the magnetosphere (Ellington et al., 2016).

Following Dungey's (1955) suggestion that the ULF waves observed by the ground-based magnetometers are signatures of standing Alfvén waves on closed magnetic field lines, the field line resonance (FLR) theory was developed to explain the excitation and properties of the resonant ULF waves (Tamao, 1965; Southwood, 1974; Chen & Hasegawa, 1974). The groundwork of MHD wave theory was mostly developed in magnetospheric box models,

where the Earth's magnetic field is stretched into a uniform field along the z axis with highly conductive ionospheres at each end (Radoski, 1967a; Southwood, 1974; Southwood & Kivelson, 1986). The wave equations for field line resonances in dipolar fields were developed by Cummings et al. (1969) and a generalized theory of standing waves in arbitrary magnetic field models was formalized by (Singer et al., 1981). However, despite the developments in the theory of standing Alfvén waves, many approximations continue to be used to estimate the eigenfrequencies of field line resonances.

One common approximation, especially for field line resonances inside of L (equatorial field line crossing distance) of 6, is the use of a dipole field to approximate Earth's magnetic field (Cummings et al., 1969). The Earth's magnetic field is known to be close to dipolar at such close distances to the planet. However, the dipole approximation is sometimes used for $L > 6$, where the deviation of the field from dipolar is significant.

The second approximation that is seen in the literature (e.g., Sandhu et al., 2018) is to estimate the fundamental eigenperiods by using the Wentzel-Kramers-Brillouin (WKB) method, sometimes referred to as time-of-flight approach (Wentzel, 1926; Kramers, 1926). The period of the fundamental mode using the WKB approximation is given by $2 \int ds/v_A$ (Warner & Orr, 1979), where v_A is the Alfvén velocity and the integration is performed along the field line. Wild et al. (2005) found the time-of-flight technique in a realistic magnetic field model such as Tsyganenko (1996) a considerable improvement over the time-of-flight approach in a dipolar approximation. A smaller improvement was seen by using the Singer et al. (1981) numerical technique instead of the Alfvén transit time (see Figure 1, Wild et al., 2005). Typical deviations between the time-of-flight and the numerical technique were found to be within 5 to 30 % for field lines with magnetic latitudes of 60 to 75°.

Finally, there is significant uncertainty in the mass density distribution along the field lines. Although there are several equatorial plasma density models available covering radial distances up to $L = 10$ (e.g., Sandhu et al., 2017; Li et al., 2010; Denton et al., 2022, private communication), only Sandhu et al. (2017) provide the distribution along the field that is a

function of geomagnetic activity, MLT, and L. Typically, a simple power law for the mass density is assumed (Denton et al., 2006). Denton et al. (2006) showed that the power law index, controlling the gradient of the mass density increasing or decreasing off the equator, varies with L and MLT. For field lines with $L > 6$, a significant equatorial enhancement of the mass density develops (see Figure 8, Denton et al., 2006). Takahashi (2004) also observed a concentration of heavy ions at the magnetic equator, in agreement with Denton et al. (2006). Electron density, however, was found to have a minimum at the magnetic equator in several studies (Goldstein et al., 2001; Denton, 2002; Denton et al., 2002), in contrast to Sandhu et al. (2017) who found a local maximum.

In this study, we calculate the numerical eigenperiods using the Singer et al. (1981) approach in the realistic field model of Tsyganenko (1996) (hereafter, referred to as T96) and two plasma density models by Sandhu et al. (2017, which we will refer to as the S2017 model) and by Denton et al. (2022, which we will refer to as the D2022 model) that cover the radial distances up to $L = 10$ at all local times. Both the T96 and the plasma density models depend on the geomagnetic activity and the solar wind parameters, allowing us to investigate the field line resonance response to increasingly active geomagnetic times from quiet time ($Dst = 0$ nT) to moderate activity ($Dst = -100$ nT). We evaluate the fundamental eigenperiods for a dipolar field and Alfvén wave transit time approximations and compare the eigenperiod deviations between these approximations and the numerical calculations using the Singer et al. (1981) approach. Additionally, we evaluate the effect on the fundamental eigenperiods from using different mass distributions along the field lines, as the power law index is not known accurately.

Understanding the effect of increasing geomagnetic activity and the field line configuration on standing wave resonances is important for understanding many dynamic processes in the magnetosphere. Field line resonances are also a vital tool for magnetoseismic techniques for estimating the plasma mass density along the field lines from the measured ULF frequencies by the in-situ spacecraft and ground magnetometers (Takahashi, 2004; Menk &

Waters, 2013). By understanding the limitations of the field line resonance calculations and the associated approximations, we can refine the the mass-inversion techniques and better our understanding of momentum and energy transport throughout the magnetosphere.

Following this introduction in section 4.2, we describe the models used in this study and the method for calculating the field line resonances. The magnetospheric activity has been parameterized in the models by using various activity indices (Dst, AE, K_p etc.). In section 4.2.3, we describe the way in which we select values of the indices. Then, in section 4.3, we present the results of this study in which we calculate the field line resonance periods for three activity levels and use two different models for electron density and ion mass. In section 4.4, we discuss how the waves respond to different models and activity levels. Finally, we summarize our results and compare them to some of the observations of ULF waves.

4.2 Methods

4.2.1 Magnetic Field Model

We use an empirical data-based magnetic field model by Tsyganenko (1995, 1996) (T96). The T96 model includes contributions from all magnetospheric current systems, has a realistic shape and size of the magnetopause, and is parameterized by the solar wind dynamic pressure and the interplanetary magnetic field (IMF). The T96 model is based on a large number of observations and is considered valid sunward of $x{=}{-}25\,R_{\mathrm{E}}$. Since we limit this study to $x > {-}10\,R_{\mathrm{E}}$ in the magnetotail, the field model is sufficient for this study. Our choice of the magnetic field model is restricted by the density models investigated. The plasma density model by Sandhu et al. (2017) uses T96 for field line tracing, making T96 most appropriate for our study.

The T96 user's manual states that the field model parameters are valid for solar wind dynamic pressures between 0.5 and 10 nPa, Dst values between -100 and 20 nT, and B_y and B_z IMF between -10 and 10 nT. This is suitable for our choice of density models which

are valid for Dst values between -100 and 0 nT. In our calculations, we ignore the effects of seasonal dipole tilt and use the time of the spring equinox, 2000 (Mar 19th, 2000, 11:35PM UT) to give a symmetrical field line configuration.

4.2.2 Plasma Density Model

Most studies of the magnetospheric density distributions use a power law form to describe the distribution of mass density with radial distance from Earth (Denton et al., 2006), given by

$$n_e = n_{e0} \left(\frac{r}{L} \right)^{-\alpha} \tag{4.1}$$

where n_{e0} is the electron density at the equatorial crossing point of a field line, α is a power law index that can depend on L (the equatorial crossing distance of the field line) MLT, and geomagnetic activity.

Both plasma density models use the power law for the general distribution of electron density and ion mass with radial distance from the Earth, although the model by Sandhu et al. (2017) also has a term for an equatorial density enhancement/depletion.

4.2.2.1 Denton et al. (2022) Plasma Density Model

We choose the mass and electron density model by Denton et al. (2022, private communication) for its large radial range of validity ($3 \leq L < 10$) and the use of data from multiple spacecraft.

The mass density, ρ_m, is inferred from magnetospheric Alfvén frequencies measured by in-situ spacecraft. For the electron density, n_e, the Denton model used the plasma wave data from CRRES (Combined Release and Radiation Effects Satellite) and RBSP (Radiation Belt Storm Probes) or the THEMIS (Time History of Events and Macroscale Interactions during

Substorms) spacecraft potential.

The mass density at the magnetic equator is given by

$$\begin{aligned}\log_{10}(\rho_m) &= 1.178 + \frac{6.978}{L} - 0.1516L + 0.003690F_{10.7} \\ &+ 0.1692\cos((MLT - 16.47)\pi/12) \\ &- 0.8367\tanh(0.1401LK_p) + 0.04878P_{dyn} \end{aligned} \tag{4.2}$$

where L is the equatorial crossing distance of the field line, $F_{10.7}$ is a 3-day running average of 10.7 cm solar radio flux, MLT is the magnetic local time, K_p is a 12-h running average of the K_p index, and P_{dyn} is a 24-h running average of the solar wind dynamic pressure.

The average ion mass, M, is given by

$$\begin{aligned}\log_{10}(M) &= -0.5938 + 0.08103K_p + 0.002886F_{10.7} + 0.04025L \\ &+ 0.0005228A_e + 0.06669K_p\cos((MLT - 3.48)\pi/12) \end{aligned} \tag{4.3}$$

where K_p is a 6-h running average of the K_p index and Ae is a 12-h running average of the auroral electrojet index. We use the power law (4.1) with a power law index (α) of 1 to model the distribution of the mass and electron densities along the field line.

4.2.2.2 Sandhu et al. (2017) Plasma Density Model

We use a Dst-index dependent model of the electron density and average ion mass by Sandhu et al. (2017). This model uses Cluster data spanning 2001-2012, particularly the WHISPER (Waves of High frequency and Sounder for Probing of Electron density by Relaxation) for electron density and CODIF (Composition and Distribution Function analyzer) for average ion mass data, The data are binned into six Dst bins between -100 and 10 nT. This plus the restrictions on the T96 model limits our investigation of the model to relatively weak

geomagnetic activity. An alternative formulation in terms of K_p dependence is also provided by Sandhu et al. (2017), but we chose a Dst-index version to use the same geomagnetic index as the field model.

The electron density model covers all MLT sectors for $4.5 \leq L < 9.5$. A power law distribution represents the higher-latitude regions of the field lines, and a Gaussian function describes the equatorial region:

$$\begin{aligned} n_e &= n_{e0} R_{norm}^{-\alpha} && \text{for } R_{norm} \leq 0.8 \\ &= a \exp\left[-\frac{1}{2}\left(\frac{R_{norm}-1}{0.1}\right)^2\right] + n_{e0} && \text{for } R_{norm} > 0.8 \end{aligned} \tag{4.4}$$

and

$$R_{norm} = r/L \tag{4.5}$$

$$n_{e0} = 10^{1.6+0.00667Dst}(1-0.0952)L + 3.68\cos(15MLT + 83 - 1.18Dst) \tag{4.6}$$

$$\alpha = 0.211 + 0.0616 + 0.423\cos(15MLT + 223) \tag{4.7}$$

$$a = 10^{0.785+0.00681Dst} + 3.47\cos(15MLT + 324) \tag{4.8}$$

where n_{e0} is the equatorial electron density, α is the power law index, and a is the maximum value of the density enhancement at the equator.

The average ion mass, m_{av}, averaged over all measurements in an MLT-L-Dst bin, is calculated using a modified version of the power law in (4.1):

$$m_{av} = m_{av0} R_{norm}^{-\beta} \tag{4.9}$$

where

$$
\begin{aligned}
m_{av0} &= 19.4 + 0.164 D_{st} - (1.62 + 0.0247 D_{st}) L \\
&+ 2.52 \cos(15 MLT + 61)
\end{aligned} \tag{4.10}
$$

and

$$
\beta = -1.91 + 0.165 L + (0.851 + 0.00559 D_{st}) \cos(15 MLT + 270) \tag{4.11}
$$

where m_{av0} is the average ion mass at the magnetic equator and β is the power law index. The average ion mass model covers all MLT sectors in the region of $5.9 \leq L < 9.5$.

4.2.3 Solar Wind and Interplanetary Magnetic Field Parameters

There exist many indices to parameterize the magnetospheric and geomagnetic activity at Earth. For example, ring current activity is usually estimated by the *Dst* index obtained from magnetometer stations near the equator and is a good indication of a storm. The auroral activity, which correlates with substorm times, is better forecasted with the *Ae* index derived from horizontal deviations in the geomagnetic field at observatories in the northern auroral zone. There are also global magnetic activity indices, most popularly the K_p index, which has been reliably used for over 70 years as an indicator of geomagnetic variation (Matzka et al., 2021). Since our chosen field model (T96) already utilizes the *Dst* index as an input parameter, we use *Dst* instead of the K_p index to quantify the strength of the geomagnetic activity.

We use available *OMNIWeb* data (`https://omniweb.gsfc.nasa.gov/`) between 1995 and 2022 for *Dst* and K_p indices, interplanetary magnetic field, and solar wind dynamic pressure (see Figure 4.1). We bin the required solar wind and IMF parameters into 10 *Dst* bins between -100 and 0 nT and use the median values in each bin for our analysis. We characterize quiet time as a *Dst* range of -30 nT $<$ *Dst* $<$ 0 nT, weak storm periods when

-30 nT > Dst > -50 nT, and moderate storm activity when -50 nT > Dst > -100 nT, like Borovsky and Shprits (2017).

We use median values of K_p for each of the Dst bins in the -100 and 0 nT range (Figure 4.2), since one of our chosen density models has a K_p index dependence. The median of K_p index reaches 5 at -100 nT Dst, which is characterized as a minor disturbance by the NOAA space weather scale (`https://www.swpc.noaa.gov/noaa-scales-explanation`). Therefore, by limiting our density models to $K_p < 5$ we will remain in the valid range for the T96 model.

The median of the solar wind dynamic pressure correlates with the geomagnetic activity index (Dst) from 1.4 nPa at quiet times to 2.7 nPa for Dst of -100 nT (Figure 4.3). The averages for each Dst bin (grey triangles) and the range of the data (grey whiskers, or 1.5 times the interquartile range) increase significantly more than the medians.

As the B_z component of the IMF decreases below zero, the Dst index generally decreases. At quiet time (Dst = 0 nT), B_z is nearly zero. A median B_z value of -5 nT roughly corresponds to a moderate activity of Dst of -100 nT, which is the limit of our investigation (Figure 4.4). The median of the B_y component does not correlate with increased geomagnetic activity, as expected (Figure 4.5). The B_y component of the IMF can induce a nonuniform B_y in the closed magnetosphere, leading to asymmetries in the field line foot points and azimuthal flow in the ionosphere (Tenfjord et al., 2015), but we ignore such effects to focus on a symmetrical magnetosphere configuration in this study. The B_x and B_y components are not usually significant for geomagnetic storms, and, therefore, we set B_y and B_x IMF to zero for all levels of geomagnetic activity.

The 10.7 cm solar radio flux ($F_{10.7}$) is kept constant at 150 sfu (solar flux units), which is roughly the average value observed during the spring equinox of 2000 (Tapping, 2013).

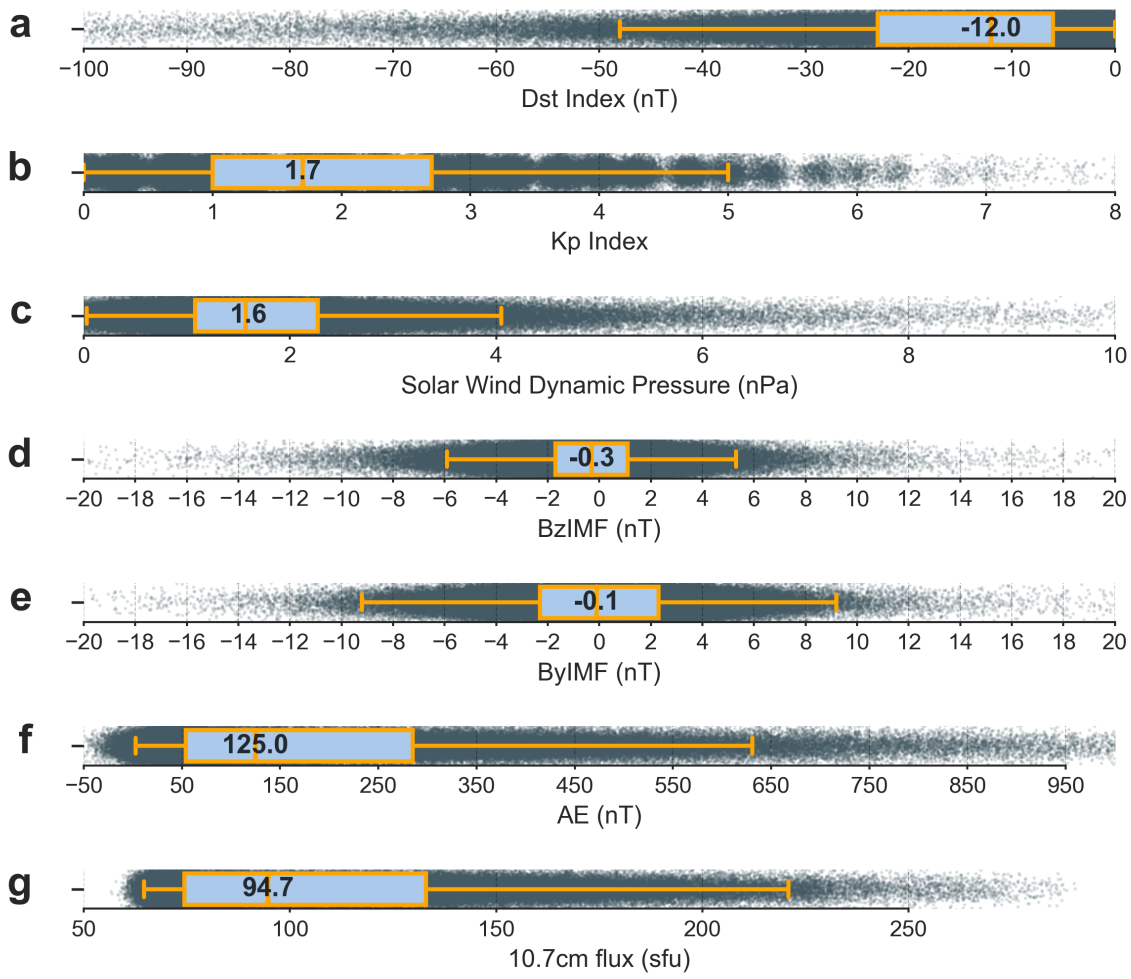

Figure 4.1: OMNIWeb data between 1995 and 2022, shown as grey dots for each data point for: (a) *Dst* index, (b) K_p index, (c) solar wind dynamic pressure, (d) B_z IMF, (e) B_y IMF (f) auroral electrojet index (AE), and (g) 10.7cm flux. The superimposed box plots show the lower, second, and upper quartiles. The second quartiles (medians) are plotted with vertical orange lines and text inserts. The lower and upper whiskers (error bars) outside the box plots denote the deviations from the lower and upper quartiles by 1.5 interquartile ranges (difference between the upper and the lower quartile).

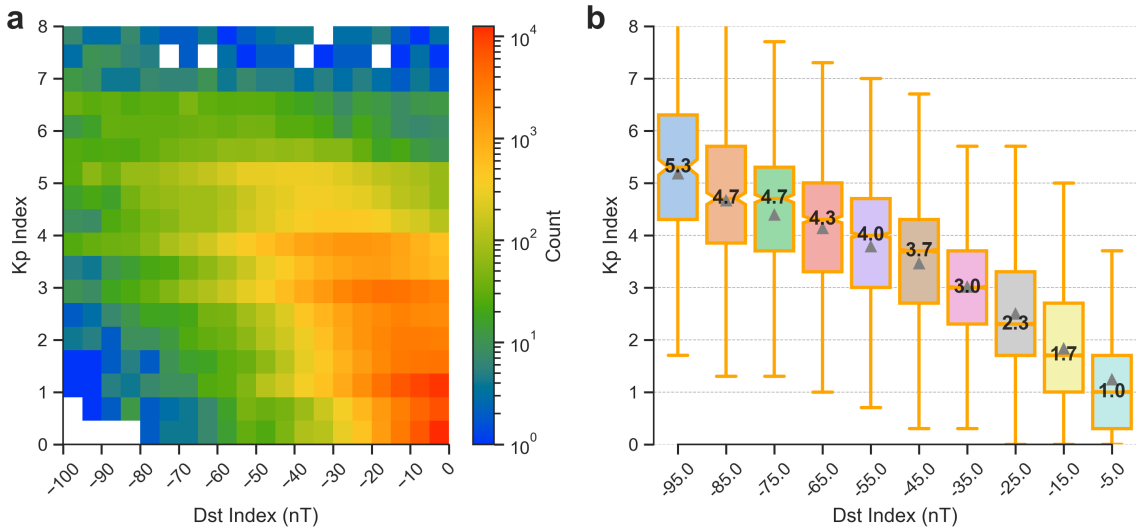

Figure 4.2: K_p index against Dst index from OMNIWeb data between 1995 and 2022, shown in (a) as a 2d histogram showing counts in each $K_p - Dst$ bin, and (b) as K_p box plots for each of the ten Dst bins between -100 nT and 0 nT. The box plots show the lower, second, and upper quartiles. The medians are indicated with horizontal orange lines and text inserts. The lower and upper whiskers outside the box plots denote the deviations from the lower and upper quartiles by 1.5 interquartile ranges.

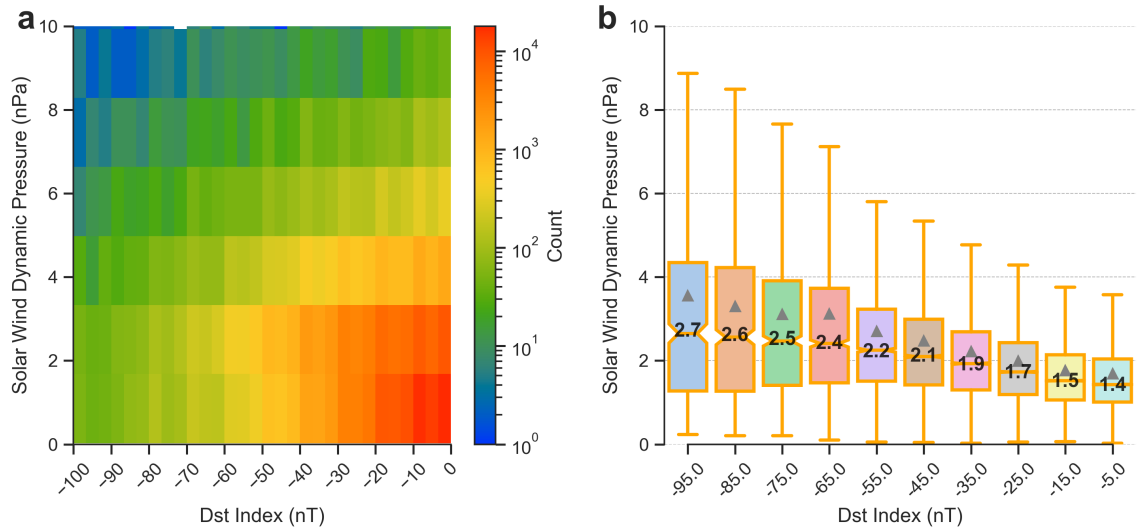

Figure 4.3: Solar wind dynamic pressure (Pdyn) against Dst index from OMNIWeb data between 1995 and 2022, shown in (a) as a 2d histogram showing counts in each $P_{dyn} - Dst$ bin, and (b) as P_{dyn} box plots for each of the ten Dst bins between -100 nT and 0 nT. The box plots show the lower, second, and upper quartiles. The medians are indicated with horizontal orange lines and text inserts. The lower and upper whiskers outside the box plots denote the deviations from the lower and upper quartiles by 1.5 interquartile ranges.

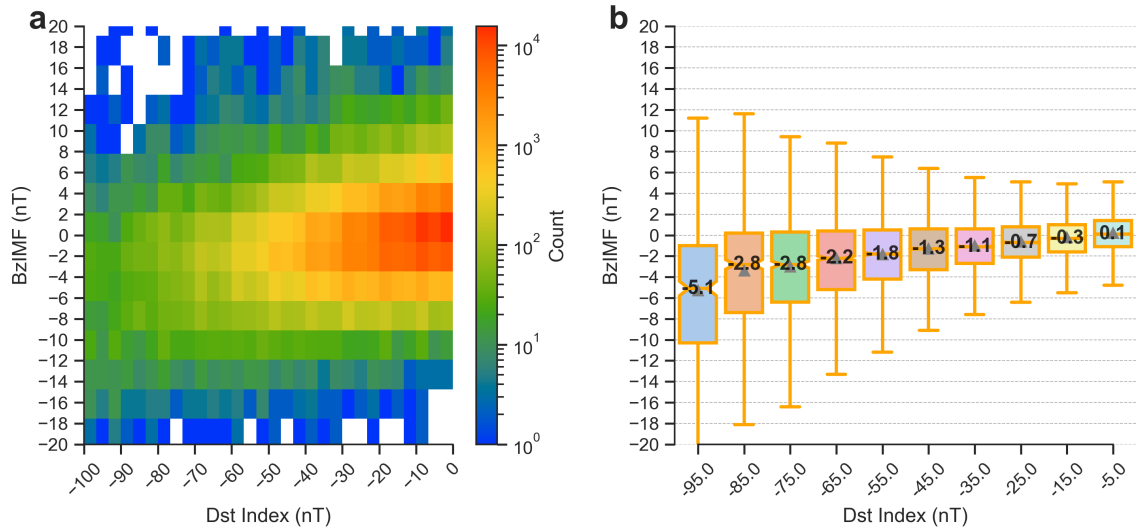

Figure 4.4: B_z of the interplanetary magnetic field (BzIMF) against Dst index from OMNI-Web data between 1995 and 2022, shown in (a) as a 2d histogram showing counts in each $B_z - Dst$ bin, and (b) as B_z box plots for each of the ten Dst bins between -100 nT and 0 nT. The box plots show the lower, second, and upper quartiles. The medians are indicated with horizontal orange lines and text inserts. The lower and upper whiskers outside the box plots denote the deviations from the lower and upper quartiles by 1.5 interquartile ranges.

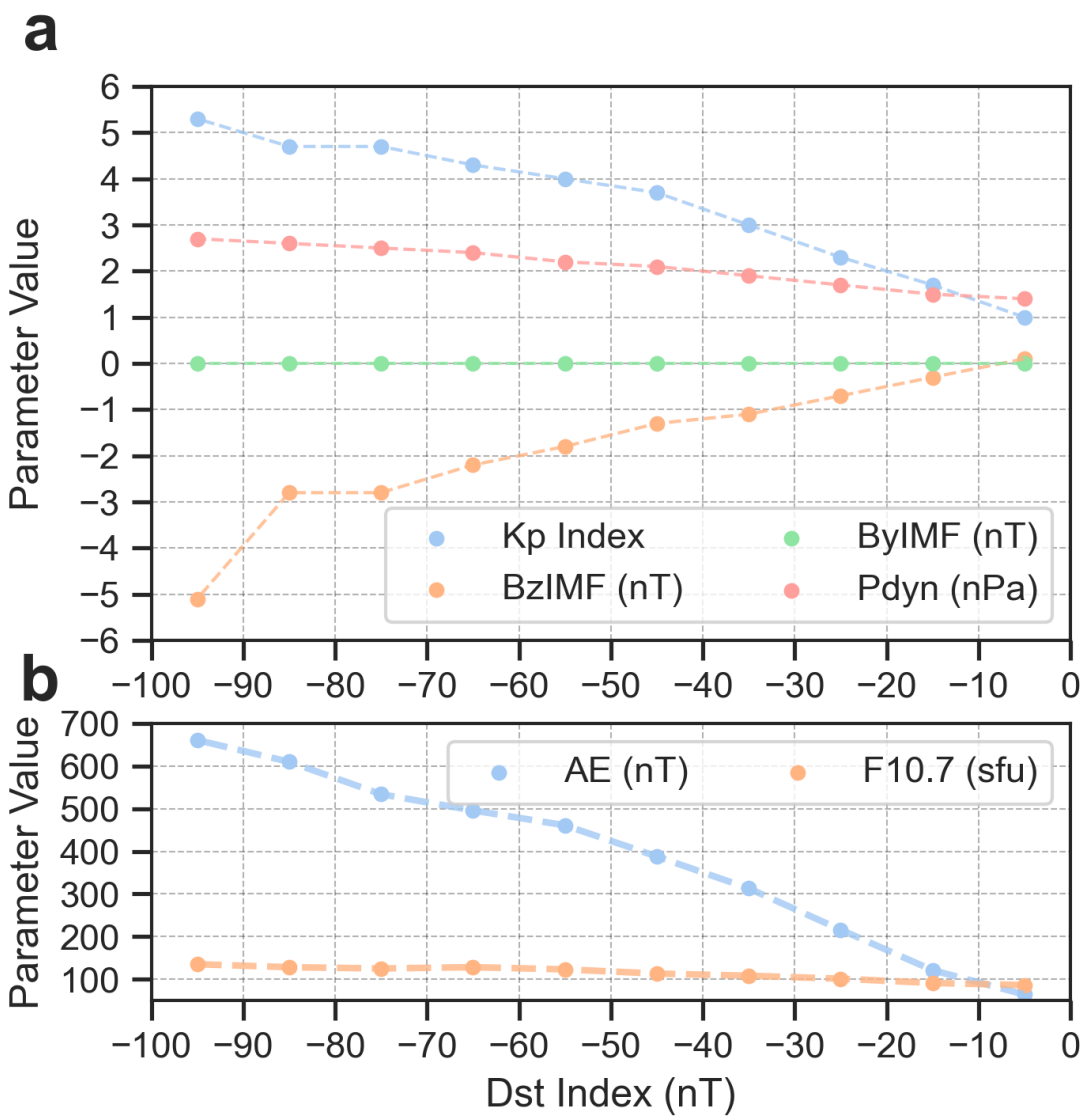

Figure 4.5: Magnetospheric and solar wind parameters inferred from the medians binned by *Dst* index bins in OMNIWeb data show in (a) for K_p, B_y IMF, B_z IMF, and P_{dyn} and (b) for *AE* index and 10.7cm flux ($F_{10.7}$).

4.2.4 Standing Wave Model

The field line eigenfrequencies are calculated in a realistic magnetic field model and the plasma density models given above using the method of Singer et al. (1981). The same approach has been used to calculate the field line resonances in Saturn's magnetosphere in Rusaitis et al. (2021), and the code (available at `https://github.com/rusaitis/AlfvenWaver`) has been adapted in this study for Earth's magnetosphere.

4.3 Results

Using an adaptation of the Rusaitis et al. (2021) model for Earth's magnetosphere, we calculate the eigenperiods using the T96 magnetic field model with the plasma density (1 proton/cm^3) used by Singer et al. (1981). A comparison of the $m = 1$ eigenperiods for midnight field lines in the T96 magnetic field model to those that Singer et al. (1981) obtained using the Olson-Pfitzer model (cf. Figure 3 of Singer et al., 1981) is shown in Figure 4.6. Panel 4.6a shows a close match between the Singer et al. (1981) eigenperiods (dotted yellow line) and the eigenperiods from the T96 model (solid red line). The match is even closer to the eigenperiods calculated for dipolar field lines (dashed red line), which is not surprising since the Olson-Pfitzer field model field lines (e.g., see Figure 15 of Walker, 1976) are more dipolar than those in the Tsyganenko model. Despite the differences in the two magnetic field models, the deviations of the eigenperiods from the two models and a dipole field are similar within $12\,R_\mathrm{E}$ (Panel 4.6b). Close to the planet within $6\,R_\mathrm{E}$ the higher order multipoles of the internal field contribute little, and the eigenperiods in a realistic field model differ by only a few percent percent from those in a dipole. Outside of $6\,R_\mathrm{E}$, the deviation between the eigenperiods increases significantly to nearly 20% at $L = 12$. Beyond $L = 12$, the Olson-Pfitzer magnetic field model differs greatly from the T96 model, and our calculations diverge from those reported in Singer et al. (1981).

We calculate the eigenmodes for T96 field lines at all magnetic local times between 3

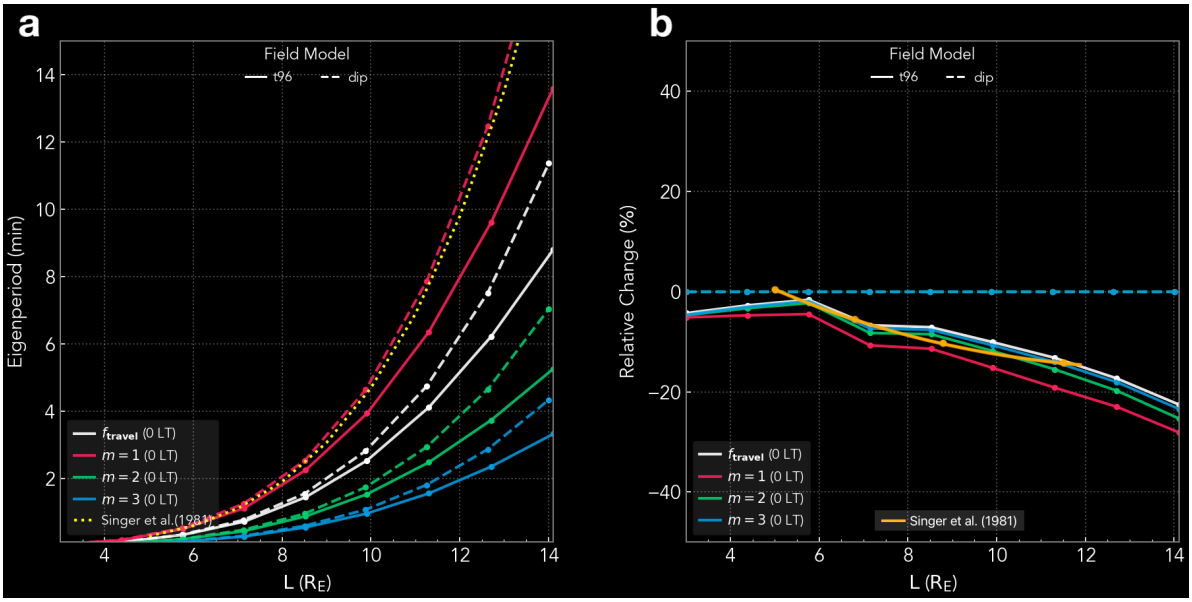

Figure 4.6: (a) Field line eigenperiods for the first three modes (shown as red, green, and blue lines) against equatorial field line crossing distance, L, fundamental eigenperiod estimate by using the Alfvén transit time (white lines), and the equivalent calculation for the $m = 1$ mode by Singer et al. (1981) in the Olson-Pfizer field model, shown with a yellow dotted line. The dashed lines show the corresponding calculations in dipolar field lines starting from the same equatorial positions as T96 field lines (solid lines). (b) Percent deviation of the corresponding eigenperiods from eigenperiods of dipolar field lines against L. The deviation of the fundamental mode in the Olson-Pfizer field model is shown in yellow.

and 10 R_E using the data-based plasma density models of Sandhu et al. (2017, Equations 4.4-4.10) and Denton et al. (2022, Equations 4.2-4.3). Since the T96 magnetic field model and the two plasma density models are parameterized by the Dst or the K_p indices, as well as the solar wind and the interplanetary magnetic field (IMF), we use the median values of the input parameters (K_p index, solar wind dynamic pressure, B_z component of the IMF, and the Ae index) from Figure 4.1 for each Dst bin. For most of the results in this section (Figures 7-21), we show calculations for three values of the Dst index and the corresponding parameters: 0 nT for quiet times, -50 nT for weak storm times, and -100 nT for moderate geomagnetic activity.

The equatorial electron densities for the two plasma density models between 3 and 10 R_E at all magnetic local times are shown in Figure 4.7. The left-side panels show electron densities for the S2017 model and the right-side panels are showing the corresponding densities for the D2022 model. Top-to-bottom, the panels show the electron densities for increasing geomagnetic activity from 0 to -100 nT. Most notably, the electron densities in the S2017 model decrease significantly from 20 cm^{-3} at $L = 5$ for $Dst = 0$ nT to ~ 10 cm^{-3} at $L = 5$ for $Dst = -50$ nT and fall below 1 cm^{-3} at dusk for $Dst = -100$ nT. With decreasing values of Dst, the densities become less uniform in azimuth, with the dawn sector becoming denser than other local times. In comparison, the electron densities in the D2022 model are more isotropic and show little change with decreasing Dst. The two model densities are closest to each other near $L = 6$ for all Dst and most local times, but the S2017 densities are higher than D2022 for $L > 6$ and lower for $L < 6$, except for the severe depletion in the dusk-side $L > 5$ sector. It is important to note that the model of S2017 is valid for a narrower radial range (between 4.5 and 9.5 R_E) than the D2022 model (3 to 10 R_E).

The equatorial average ion masses are also significantly different in the two models (Figure 4.8). The average ion masses remain highest in the post-dusk sector at all values of Dst in the S2017 model (Panels 4.8a,c,e). The average ion masses in S2017 model decrease with decreasing Dst for $L < 5$ and increase for $L > 5$. In contrast, the average ion masses increase

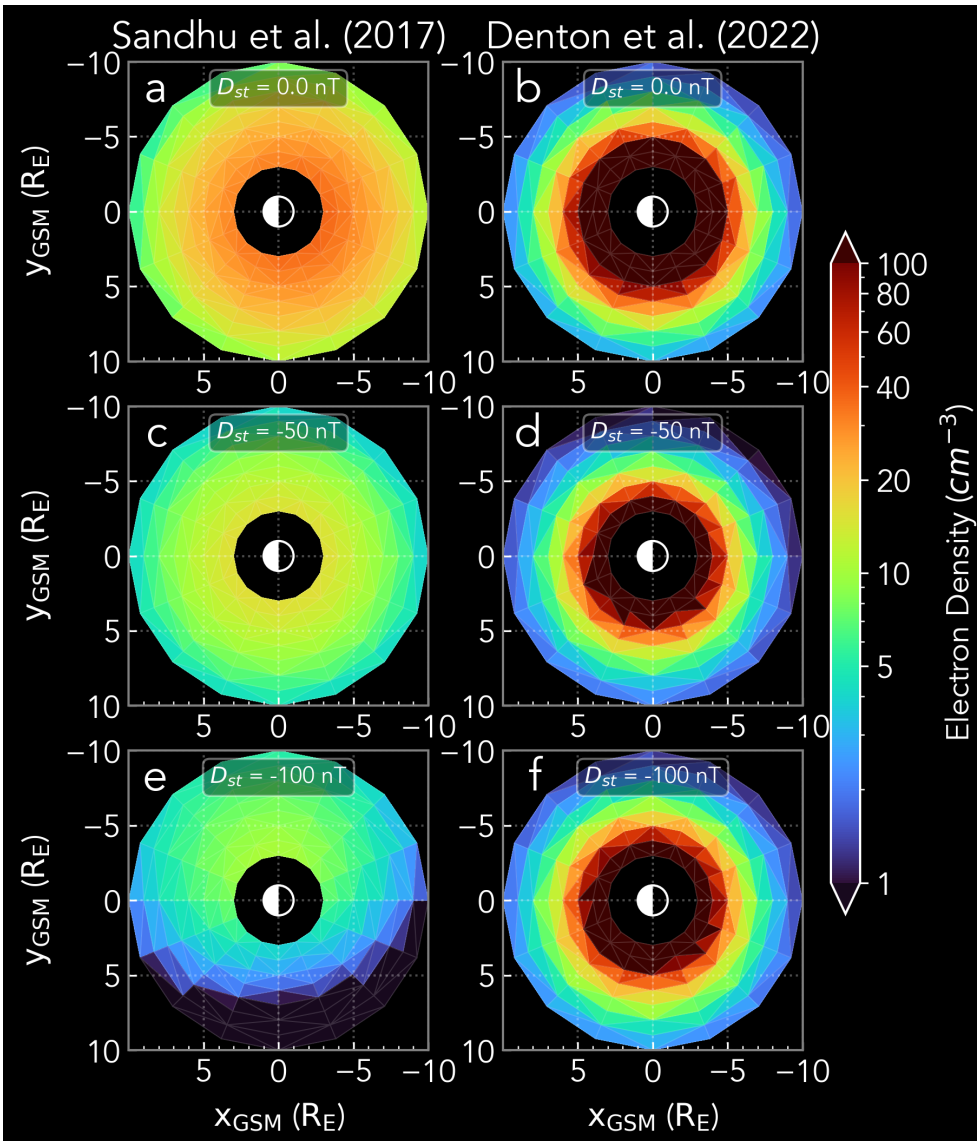

Figure 4.7: Equatorial electron densities in GSM coordinates between 3 and 10 R_E, separated left-to-right by the plasma density model: (a), (c), (e) for Sandhu et al. (2017) and (b), (d), (f) for Denton et al. (2022). Vertically, the panels are labeled with the corresponding Dst index: (a), (b) for 0 nT, (c), (d) for -50 nT, and (e), (f) for -100 nT. The sunward direction is towards the left (positive x), also shown by the illuminated Earth cartoon.

with decreasing Dst in D2022 model for all MLTs and radial distances but remain highest in the post-midnight sector at all levels of geomagnetic activity. The starkest difference between the models is at quiet time ($Dst = 0$ nT), for which the average ion mass is about 1 amu at all local times and radial distances in the D2022 model but is nearly 8 amu at $L = 5.5$ for the S2017 model. The average ion mass in the Denton2022 model increases rapidly with decreasing Dst, up to oxygen mass (16 amu) and above at $Dst = -100$ nT in the post-midnight sector.

The noon-midnight meridian electron densities and average ion masses along the field lines are shown in Figure 4.9 and Figure 4.10 for field lines traced from the equator between 3 and 10 R_E. Although both density models use a power law in r (radial distance) (Equation 4.1) from which the variation of density along the field can be extracted, the S2017 model has an equatorial electron density enhancement that is especially visible in the magnetotail plasma sheet at $Dst = -100$ nT (Panel 4.9e). In comparison, the electron densities in the D2022 model change more gradually along the field for the choice of power law index $\alpha = 1$ (Panels 4.9b,d,f). For the D2022 model, we let the equatorial ion masses populate the whole field lines. In the S2017 model, the mass varies as a power law in r, with heavy ion population found mostly near the equator at $Dst = 0$ nT (Panel 4.10a). Interestingly, despite the differences in the electron densities and the average ion masses between the two models, the Alfvén velocities along the field show many similarities (Figure 4.11). In both models, the Alfvén velocity drops to nearly 100 km/s in the midnight plasma sheet for $L > 5$ within $\pm 1\, R_E$ from the magnetic equator. At higher magnetic latitudes ($\lambda > 30°$), the Alfvén velocities reach 1000 km/s or more due to much stronger magnetic field. The noon-meridian Alfvén velocities in the two models are similar, with faster speeds at lower-latitude ($\lambda < 30°$) in the D2022 model for $L > 5$, but slower near the equator for $L < 5$.

We can see the midnight-meridian field line electron densities and the resulting eigenfrequencies in more detail in Figures 4.12 to 4.17. The results for the Sandhu et al. (2017) model for Dst index values of 0 nT, -50 nT, and -100 nT are shown in Figures 4.12, 4.13,

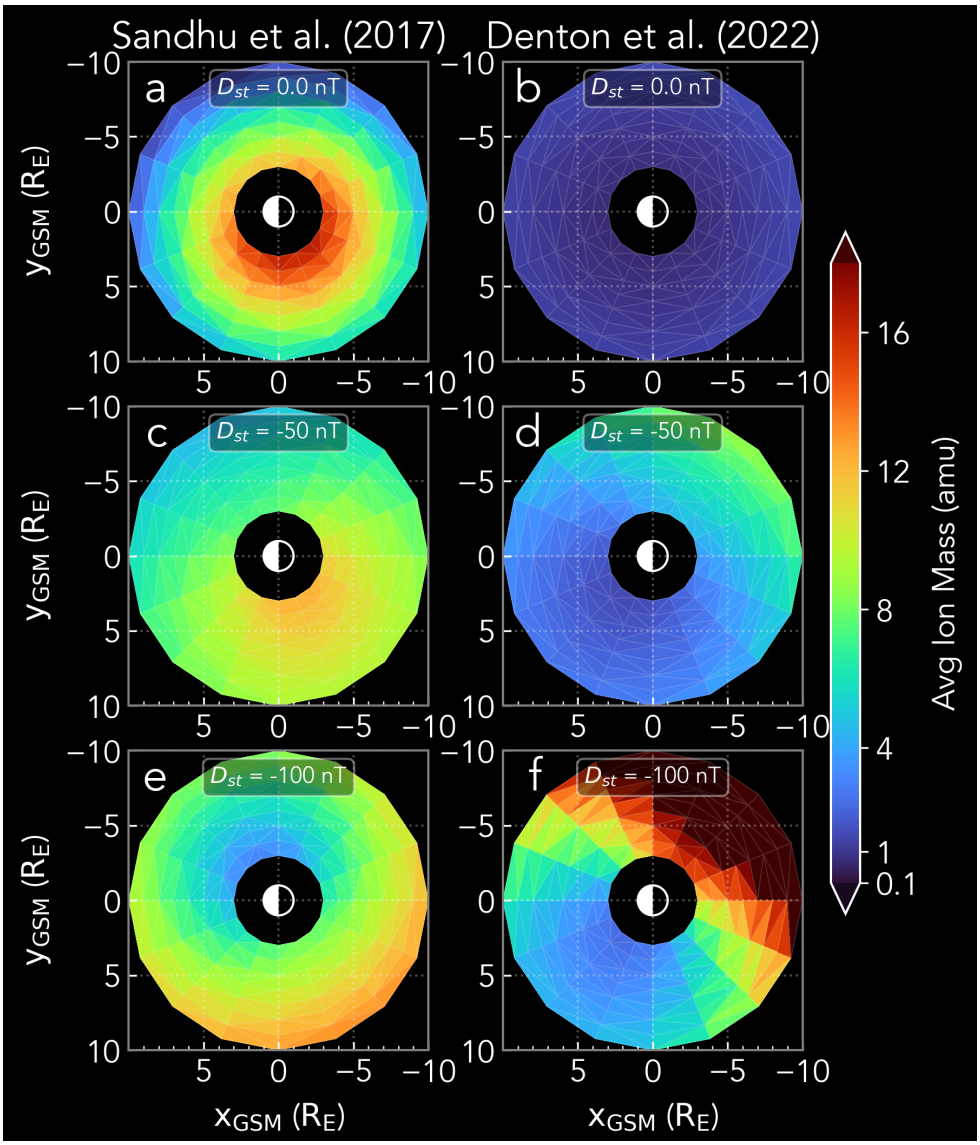

Figure 4.8: Equatorial average ion masses in GSM coordinates between 3 and 10 R_E, separated left-to-right by the plasma density model: (a), (c), (e) for Sandhu et al. (2017) and (b), (d), (f) for Denton et al. (2022). Vertically, the panels are labeled with the corresponding *Dst* index: (a), (b) for 0 nT, (c), (d) for -50 nT, and (e), (f) for -100 nT. The sunward direction is towards the left (positive x), also shown by the illuminated Earth cartoon.

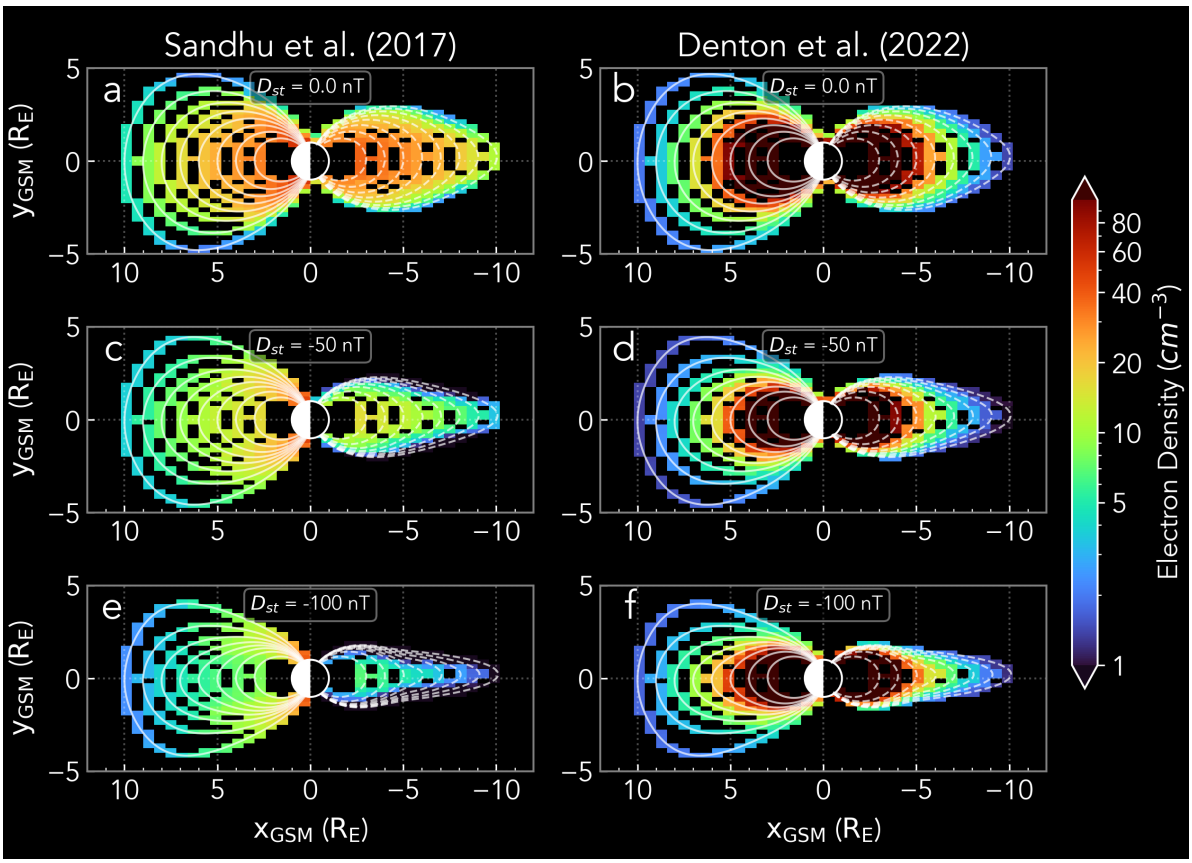

Figure 4.9: Noon-midnight meridian plots of electron densities along the field lines in GSM coordinates, separated left-to-right by the plasma density model: (a), (c), (e) for Sandhu et al. (2017) and (b), (d), (f) for Denton et al. (2022). Vertically, the panels are labeled with the corresponding *Dst* index: (a), (b) 0 nT, (c), (d) -50 nT, and (e), (f) -100 nT. The sunward direction is towards the left (positive x), also shown by the illuminated Earth cartoon. The field lines are traced at noon and midnight from the same equatorial positions between 3 and 10 R_E in the T96 magnetic field model.

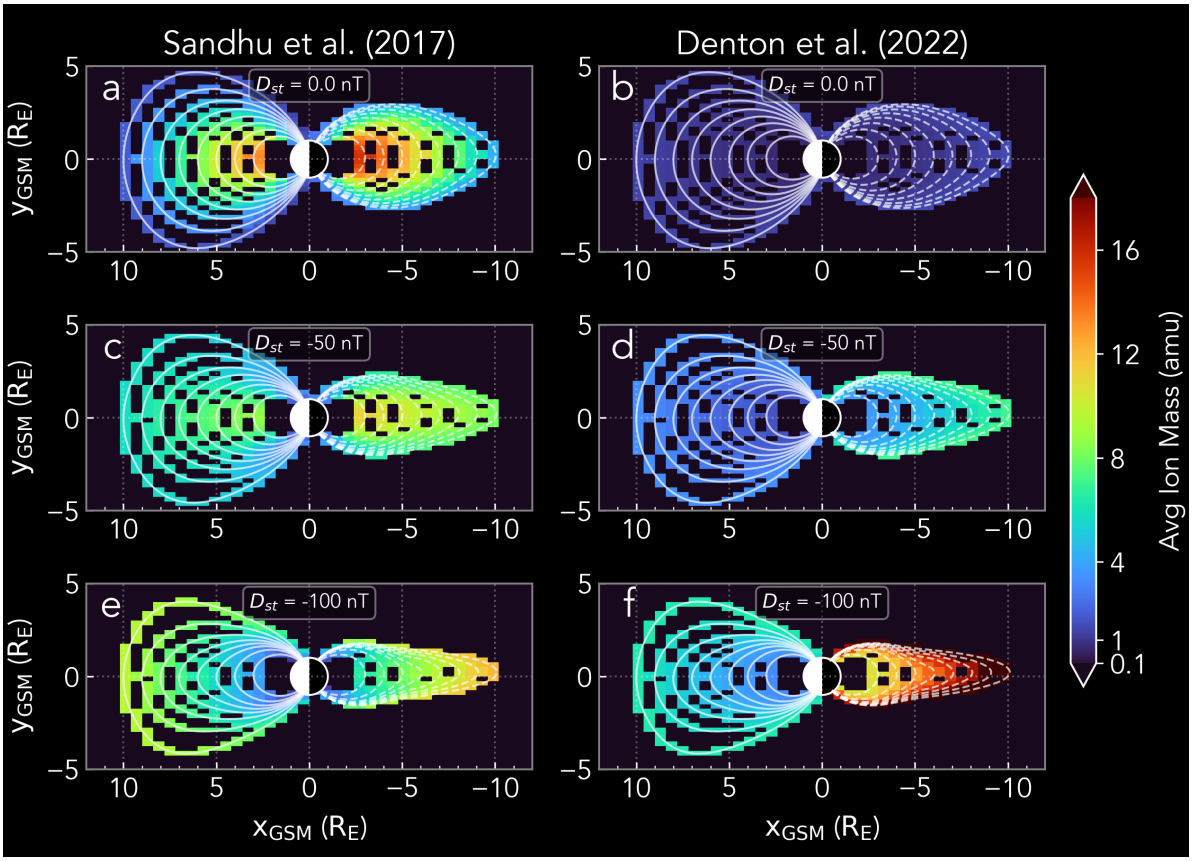

Figure 4.10: Noon-midnight meridian plots of average ion masses along the field lines in GSM coordinates, separated left-to-right by the plasma density model: (a), (c), (e) for Sandhu et al. (2017) and (b), (d), (f) for Denton et al. (2022). Vertically, the panels are labeled with the corresponding *Dst* index: (a), (b) 0 nT, (c), (d) -50 nT, and (e), (f) -100 nT. The sunward direction is towards the left (positive x), also shown by the illuminated Earth cartoon. The field lines are traced at noon and midnight from the same equatorial positions between 3 and 10 R_E in the T96 magnetic field model.

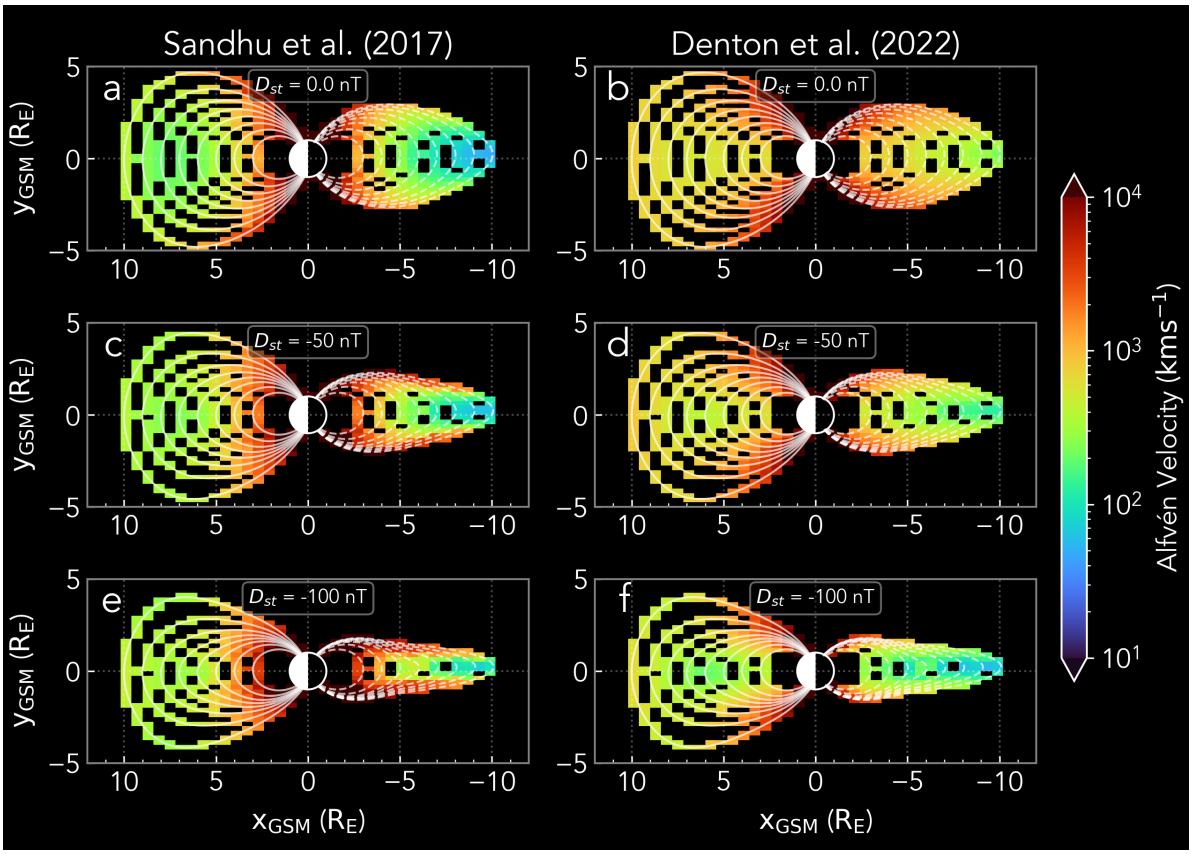

Figure 4.11: Noon-midnight meridian plots of Alfvén velocities along the field lines in GSM coordinates, separated left-to-right by the plasma density model: (a), (c), (e) for Sandhu et al. (2017) and (b), (d), (f) for Denton et al. (2022). Vertically, the panels are labeled with the corresponding *Dst* index: (a), (b) 0 nT, (c), (d) -50 nT, and (e), (f) -100 nT. The sunward direction is towards the left (positive x), also shown by the illuminated Earth cartoon. The field lines are traced at noon and midnight from the same equatorial positions between 3 and 10 R_E in the T96 magnetic field model.

and 4.14, and the corresponding results for the Denton et al. (2022) model are shown in Figures 4.15, 4.16, and 4.17. Panel 4.12a shows quiet-time ($Dst = 0$ nT) midnight electron densities of Sandhu et al. (2017) for field lines between 3 and 10 R_{E} in the noon-midnight meridian plane, with solid lines showing results for T96 field model, and dashed lines showing field line properties for dipolar field lines traced from the same equatorial positions. The equatorial enhancements of Sandhu et al. (2017) are clearly evident in Panel 4.12b showing the electron densities against magnetic latitude for the field lines selected in Panel 4.12a. The enhancement is confined to 10 to 20° off the magnetic equator and is strongest at larger L.

The eigenfrequencies for the first four modes for midnight magnetotail field lines are shown in Panel 4.12c with red, green, blue, and magenta lines. The eigenfrequency estimates based on the WKB approximation are shown with white lines. The calculations in T96 field model are shown with solid lines, and the equivalent calculations for dipolar field lines (with the same density model and equatorial crossing points) are shown with dashed lines. The eigenfrequencies for the dipole field are nearly identical to those in T96 inside of 6 R_{E}. This is expected due to the T96 model differing little from a dipole inside of 6 R_{E}. For $L > 6$, the eigenperiods calculated in T96 model diverge from those calculated in a dipole field (Panel 4.12d). The panel shows the difference between T96 eigenperiods (T_{T96}) and those from the dipole (T_d) as a percentage of the dipole eigenperiods ($(T_{T96} - T_d)/T_d \times 100\%$). The eigenperiod deviation is within 5 % inside of $L = 6$ but gets larger to 15 to 20 % at $L = 10$ for all modes. The deviation is negative for all values of L, meaning that the eigenperiods in the T96 field model are shorter than those in a dipole field for field lines that cross the equator at the same radial distance.

For weak geomagnetic activity ($Dst = -50$ nT), Figure 4.13 shows results for the S2017 density model for field lines traced from the same equatorial positions as in Figure 4.12. The magnetotail field lines are more stretched tailward as seen in Panel 4.13a, and the equatorial electron density enhancement is significantly larger and more narrowly confined in magnetic

latitude than at the quiet time configuration (Panel 4.13b). The electron densities also decrease by a factor of 2 to 3 at all magnetic latitudes and radial distances, and for $L > 8$ field lines the densities get lower than 1 cm^{-3}. The eigenfrequencies start to diverge from those in a dipole field outside of $L = 5$. At $L = 10$, the percent deviations in the eigenperiods for all modes decrease to negative 35 %, whereas within $L = 5$ the T96 eigenperiods match those of a dipole even more closely than at quiet times.

At moderate geomagnetic activity of -100 nT Dst, the trend seen for lower Dst continues: the field lines get more stretched, the electron densities become lower by a factor of 2 to 4, the enhancement gets confined closer to the equator, and the eigenperiods of all modes deviate even more from their values in a dipole field, decreasing by 40-45% at $L = 10$ (Figure 4.14). Inside of $L = 5$, however, there is a significant positive deviation of up to 20% – the T96 eigenperiods become larger than those in a dipole.

Similar changes to eigenperiods with increasing geomagnetic activity are observed in the D2022 density model (Figures 4.15 to 4.17). The electron density model does not have an equatorial enhancement term like Sandhu et al. (2017); thus, the electron density variations along the field look more gradual (Panel 4.15a). However, the equatorial electron densities are generally lower than Sandhu et al. (2017), but higher close to the ionosphere at high magnetic latitudes. The resulting eigenperiods are lower than the ones calculated in the S2017 model: the first four modes have eigenperiods between 1 and 10 min at $L = 10$ for Denton et al. (2022) but are roughly between 5 and 25 min for Sandhu et al. (2017) in the quiet-time magnetosphere. Nevertheless, the deviation of the eigenperiods in T96 from eigenperiods in a dipole model is like that in the S2017 density model: at $L = 10$ and $Dst = 0$ nT, the deviation is nearly negative 20 % for the $m = 1$ mode (Panel 4.15d).

For weak geomagnetic activity ($Dst = -50$ nT), the midnight electron densities in the D2022 model decrease by a factor of 2 or less (Panel 4.16b) and eigenperiods decrease by a few minutes to respective values for dipolar field lines (Panel 4.16c). At $L = 10$, the deviation of the eigenperiods in T96 from those calculated in a dipole field increases to negative 30 %

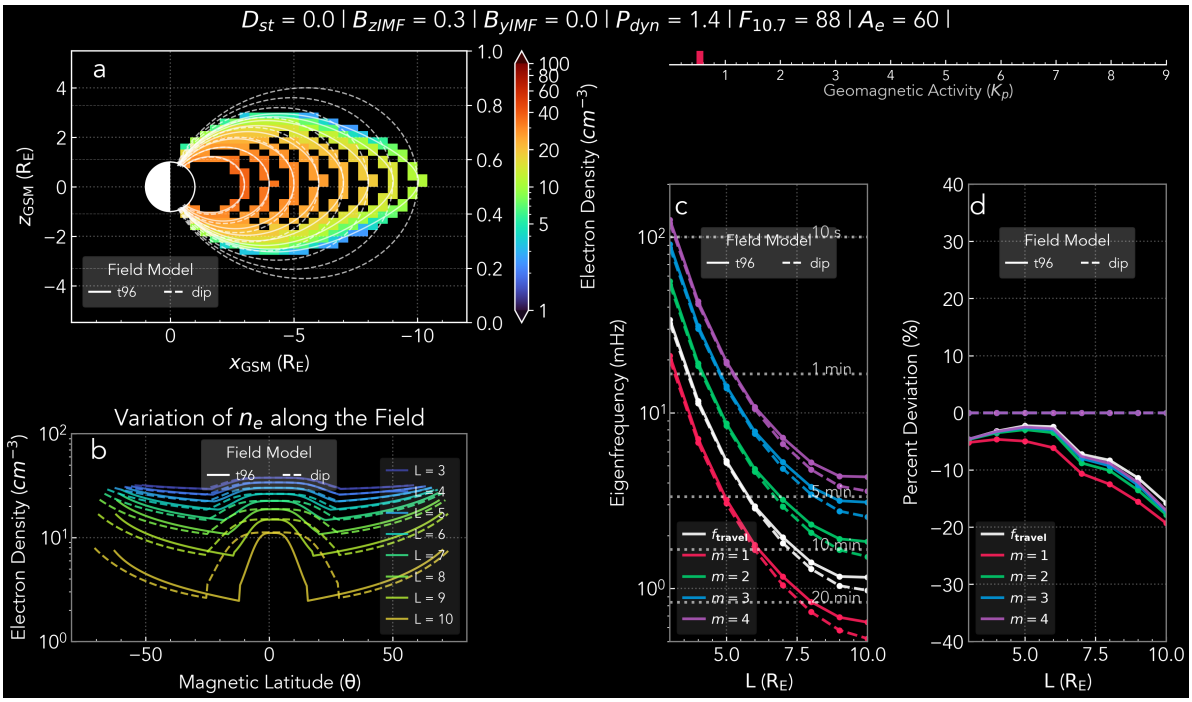

Figure 4.12: Field line parameters and eigenfrequencies in the midnight magnetotail for Sandhu et al. (2017) plasma density model and T96 magnetic field model for Dst index of 0 nT. Panel (a) shows electron densities along the field lines in the noon-midnight meridian, panel (b) shows the electron densities along the field against magnetic latitude, panel (c) shows the eigenfrequencies for the first 4 modes (red, green, blue, and magenta lines) and the frequency of the fundamental mode calculated from the Alfvén transit time (white lines), and panel (d) shows the percent deviations between the eigenperiods calculated for T96 magnetic field model and dipole field lines, with a negative deviation representing a slower eigenperiod for the T96 field lines compared to the dipole field lines that cross the equator at the same radial distance. The dotted lines in the panels (a), (b), and (c) show the results for dipolar field lines, and solid lines show results for field lines in T96.

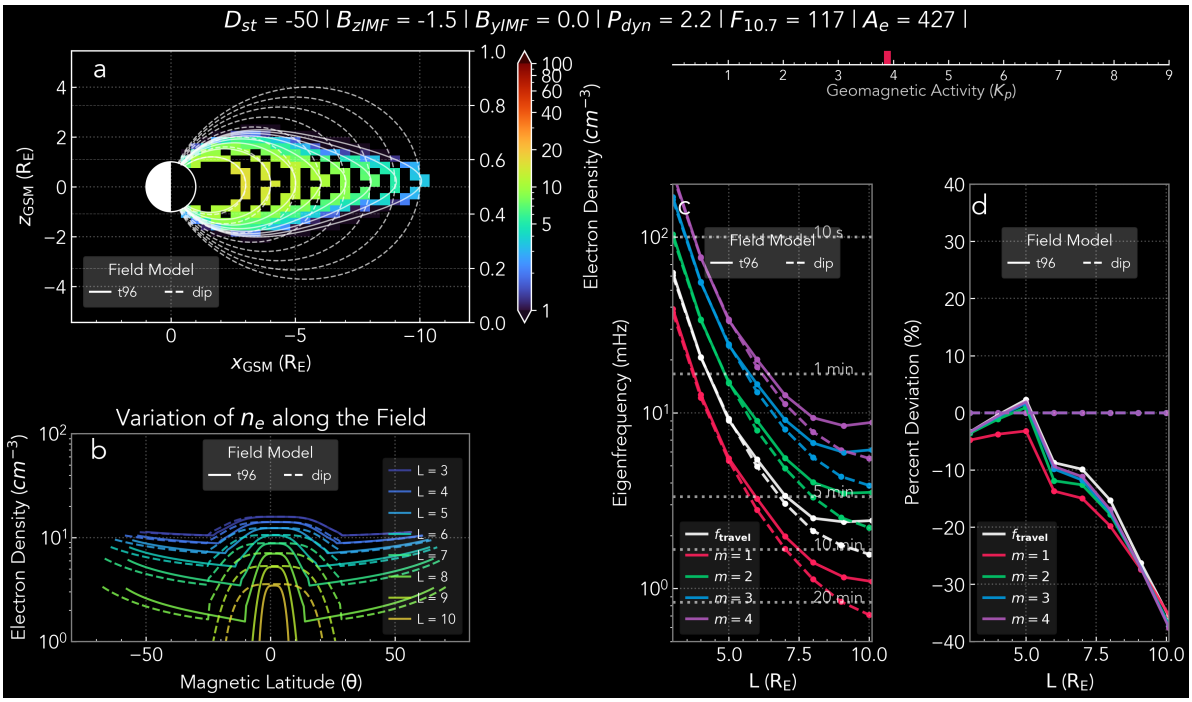

Figure 4.13: Field line parameters and eigenfrequencies in the midnight magnetotail for Sandhu et al. (2017) plasma density model and T96 magnetic field model for *Dst* index of -50 nT. Panel (a) shows electron densities along the field lines in the noon-midnight meridian, panel (b) shows the electron densities along the field lines against magnetic latitude, panel (c) shows the eigenfrequencies for the first 4 modes (red, green, blue, and magenta lines) and the frequency of the fundamental mode calculated from the Alfvén transit time (white lines), and panel (d) shows the percent deviations between the eigenperiods calculated for T96 magnetic field model and dipole field lines, with a negative deviation representing a shorter eigenperiod for the T96 field lines compared to the dipole field lines that cross the equator at the same radial distance.. The dotted lines in the panels (a), (b), and (c) show the results for dipolar field lines, and solid lines show results for field lines in T96.

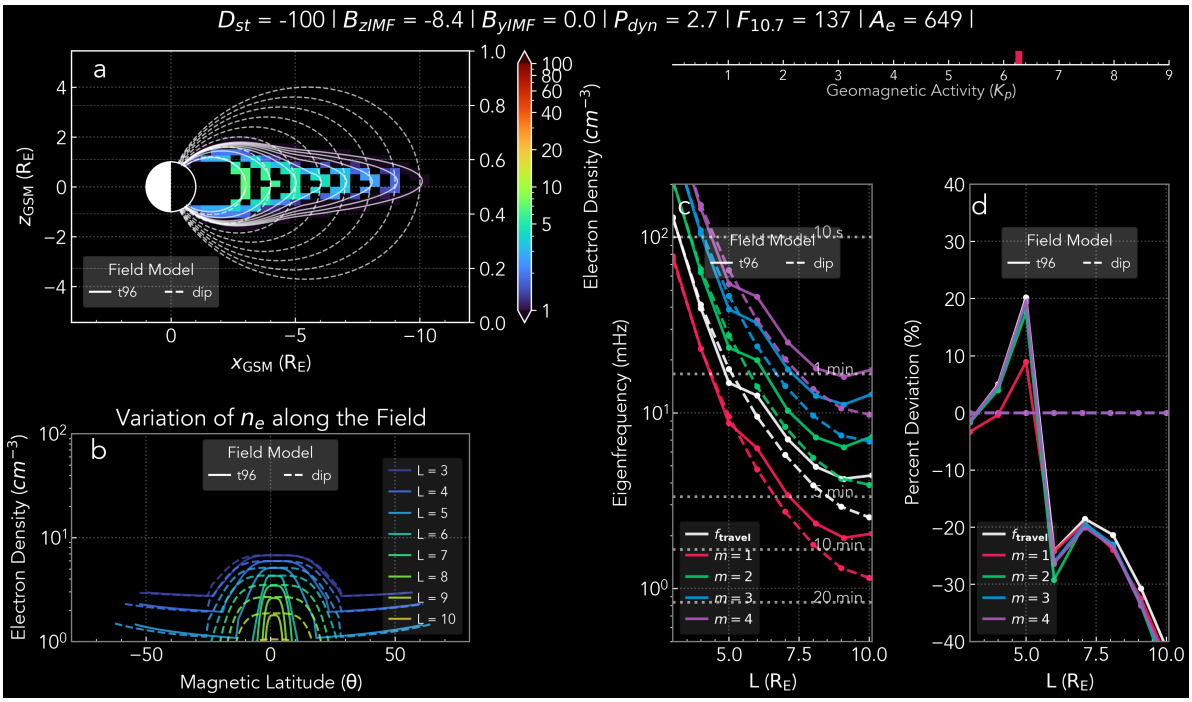

Figure 4.14: Field line parameters and eigenfrequencies in the midnight magnetotail for Sandhu et al. (2017) plasma density model and T96 magnetic field model for *Dst* index of -100 nT. Panel (a) shows electron densities along the field lines in the noon-midnight meridian, panel (b) shows the electron densities along the field against magnetic latitude, panel (c) shows the eigenfrequencies for the first 4 modes (red, green, blue, and magenta lines) and the frequency of the fundamental mode calculated from the Alfvén transit time (white lines), and panel (d) shows the percent deviations between the eigenperiods calculated for T96 magnetic field model and dipole field lines, with a negative deviation representing a shorter eigenperiod for the T96 field lines compared to the dipole field lines that cross the equator at the same radial distance. The dotted lines in the panels (a), (b), and (c) show the results for dipolar field lines, and solid lines show results for field lines in T96.

(panel 4.16d), a bit lower, but similar to the deviation calculated with the S2017 model. At moderate geomagnetic activity ($Dst = -100$ nT), we find higher eigenperiods than in the dipole field inside of $L = 6$, but much lower outside of $L = 6$ (Panel 4.17d).

Eigenfrequencies for both density models at other local times can be seen in the equatorial eigenfrequency visualizations in Figure 4.18. Panels 4.18a,c,e show eigenfrequencies for the S2017 model for increasing geomagnetic activity ($Dst = 0$ nT, -50 nT, and -100 nT), and panels 4.18b,d,f show equivalent calculations for D2022 model. The eigenfrequencies are similar between the two models inside of $5\,R_{\mathrm{E}}$, except for $Dst = -100$ nT, and outside of $5\,R_{\mathrm{E}}$ where eigenfrequencies are generally lower by a factor of 2 or three in the D2022 model. An obvious exception is the strong post-dusk increase of eigenfrequencies in the S2017 model for moderate geomagnetic activity ($Dst = -100$ nT) (Panel 4.18e). At dusk, the eigenfrequencies are larger by a factor of 4 or more than at dawn. In comparison, there is a much smaller increase of eigenfrequencies in the dusk sector in the D2022 model, with the dusk-side eigenfrequencies larger by 50-100% at most. A similar comparison for eigenperiods is shown in Figure 4.19. Panels 4.19a-f show the fundamental eigenperiods inside of $5\,R_{\mathrm{E}}$ are generally less than 5 min. The outer field lines between 5 and $10\,R_{\mathrm{E}}$ range in eigenperiods between 5 and 20 min. Generally, the eigenperiods for $L > 5$ are greater by 50 to 100% in the S2017 model than in D2022, except for lowest value of Dst (-100 nT), for which the two models produce eigenperiods that agree to within 30% everywhere except the outermost dusk sector (Panels 4.19e-f).

The deviations in the $m = 1$ eigenperiods between a dipole field and a realistic field model (T96) are visualized in an equatorial plane in Figure 4.20. As seen in Figure 4.14 and Figure 4.17, the T96 eigenperiods become larger than those of a dipole inside of $L = 6$ for moderate values of Dst. This effect is consistent between the two density models. The positive deviations inside of $L = 6$ are largest at post-dawn sector, implying nearly 20% higher eigenperiods than those for dipolar field lines. Outside of $L = 6$, the negative deviations are highest post-dusk for all geomagnetic indices and both density models, reaching 40-50%

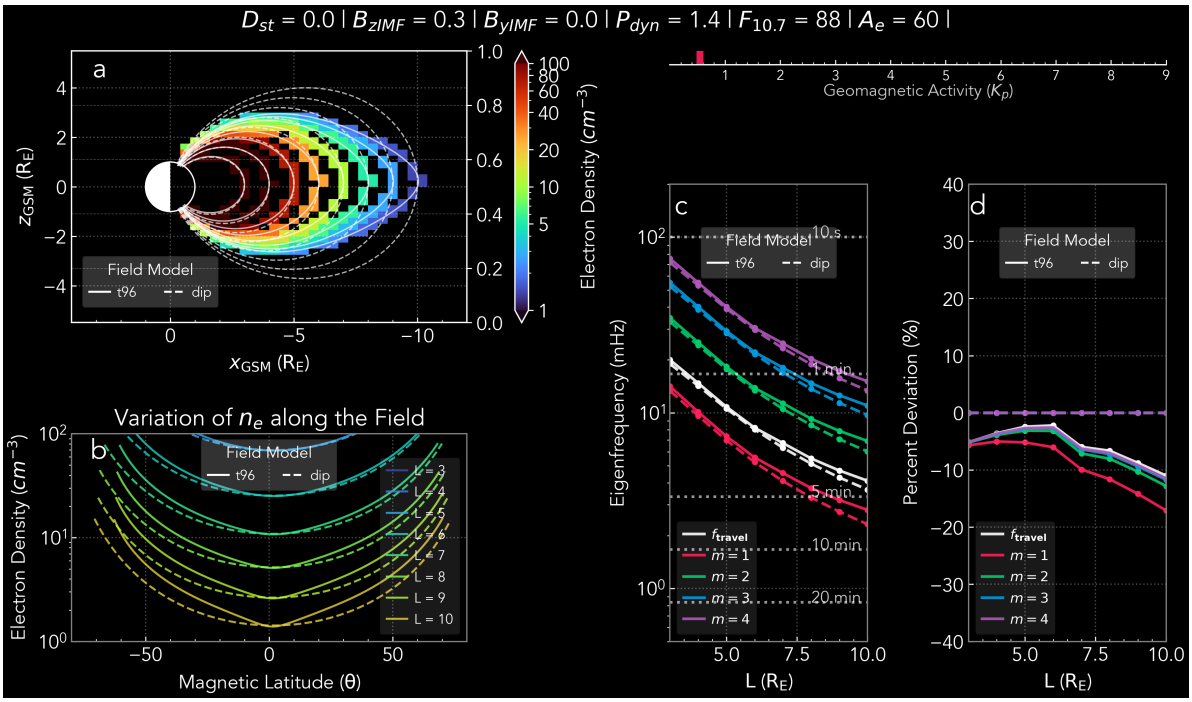

Figure 4.15: Field line parameters and eigenfrequencies in the midnight magnetotail for Denton et al. (2022) plasma density model and T96 magnetic field model for *Dst* index of 0 nT. Panel (a) shows electron densities along the field lines in the noon-midnight meridian, panel (b) shows the electron densities along the field against magnetic latitude, panel (c) shows the eigenfrequencies for the first 4 modes (red, green, blue, and magenta lines) and the frequency of the fundamental mode calculated from the Alfvén transit time (white lines), and panel (d) shows the percent deviations between the eigenperiods calculated for T96 magnetic field model and dipole field lines, with a negative deviation representing a shorter eigenperiod for the T96 field lines compared to the dipole field lines that cross the equator at the same radial distance. The dotted lines in the panels (a), (b), and (c) show the results for dipolar field lines, and solid lines show results for field lines in T96.

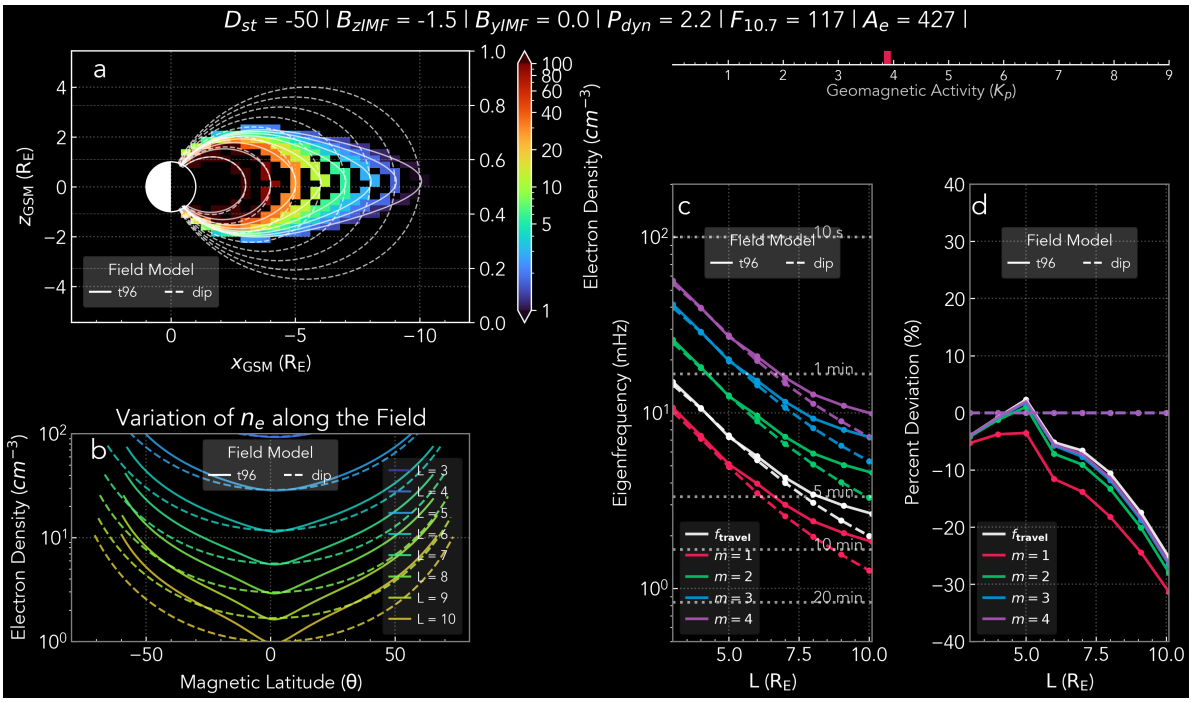

Figure 4.16: Field line parameters and eigenfrequencies in the midnight magnetotail for Denton et al. (2022) plasma density model and T96 magnetic field model for *Dst* index of -50 nT. Panel (a) shows electron densities along the field lines in the noon-midnight meridian, panel (b) shows the electron densities along the field against magnetic latitude, panel (c) shows the eigenfrequencies for the first 4 modes (red, green, blue, and magenta lines) and the frequency of the fundamental mode calculated from the Alfvén transit time (white lines), and panel (d) shows the percent deviations between the eigenperiods calculated for T96 magnetic field model and dipole field lines, with a negative deviation representing a shorter eigenperiod for the T96 field lines compared to the dipole field lines that cross the equator at the same radial distance. The dotted lines in the panels (a), (b), and (c) show the results for dipolar field lines, and solid lines show results for field lines in T96.

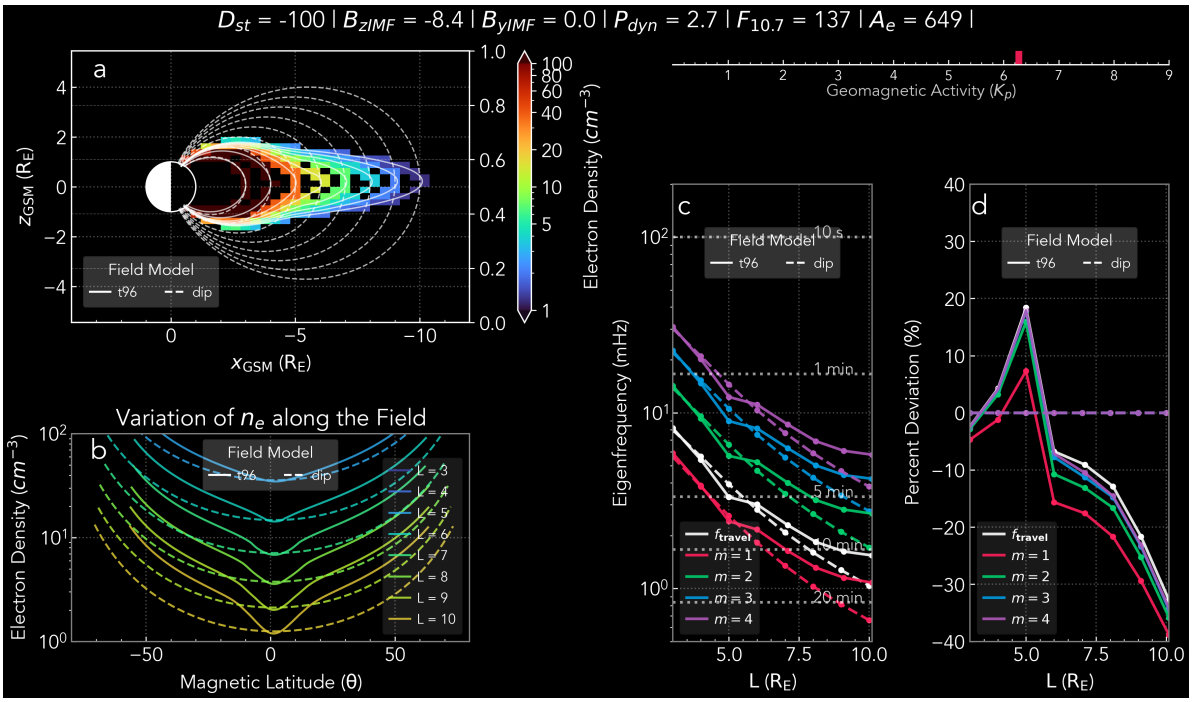

Figure 4.17: Field line parameters and eigenfrequencies in the midnight magnetotail for Denton et al. (2022) plasma density model and T96 magnetic field model for *Dst* index of -100 nT. Panel (a) shows electron densities along the field lines in the noon-midnight meridian, panel (b) shows the electron densities along the field against magnetic latitude, panel (c) shows the eigenfrequencies for the first 4 modes (red, green, blue, and magenta lines) and the frequency of the fundamental mode calculated from the Alfvén transit time (white lines), and panel (d) shows the percent deviations between the eigenperiods calculated for T96 magnetic field model and dipole field lines, with a negative deviation representing a shorter eigenperiod for the T96 field lines compared to the dipole field lines that cross the equator at the same radial distance. The dotted lines in the panels (a), (b), and (c) show the results for dipolar field lines, and solid lines show results for field lines in T96.

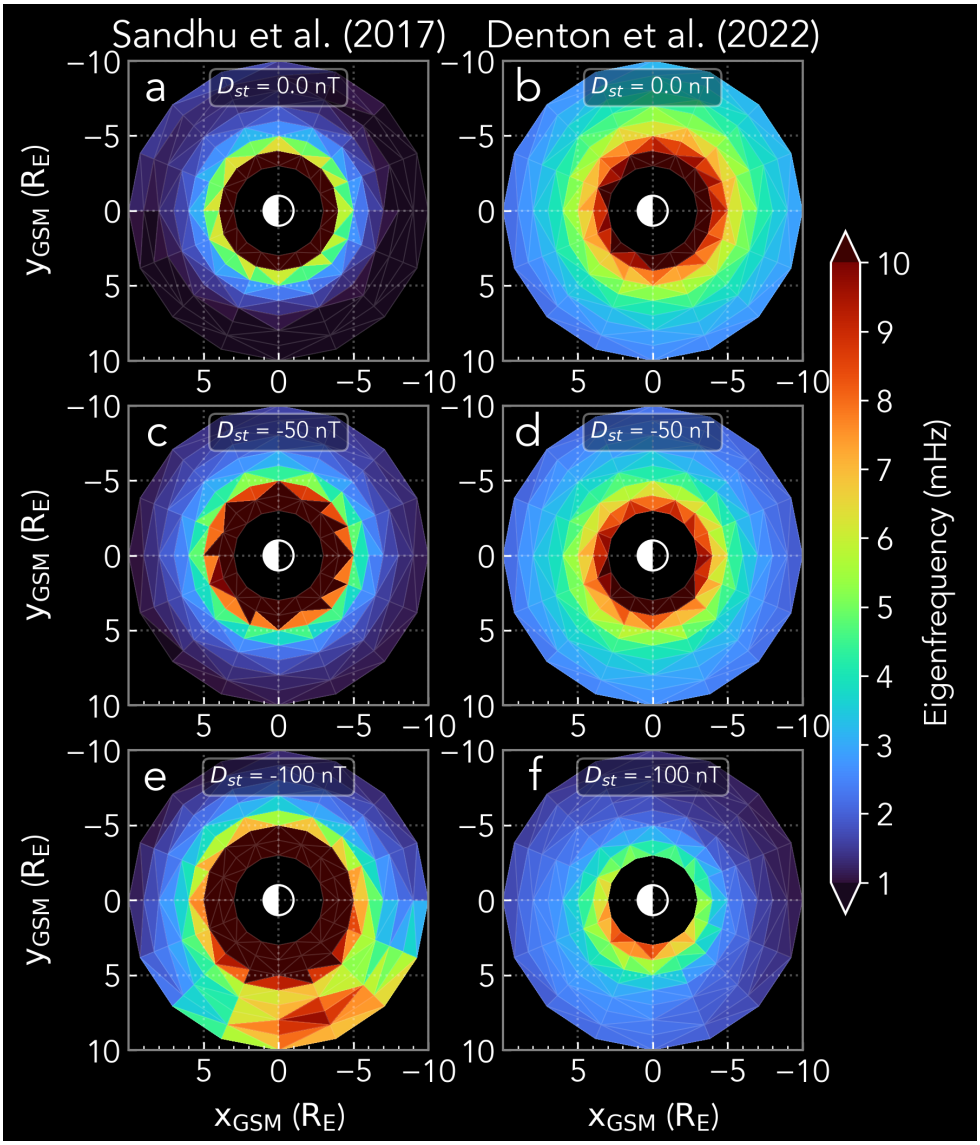

Figure 4.18: Equatorial plots of the $m = 1$ eigenfrequencies in GSM coordinates between 3 and 10 R_E, separated left-to-right by the plasma density model: (a), (c), (e) for Sandhu et al. (2017) and (b), (d), (f) for Denton et al. (2022). Vertically, the panels are labeled with the corresponding Dst index: (a), (b) for 0 nT, (c), (d) for -50 nT, and (e), (f) for -100 nT. The sunward direction is towards the left (positive x), also shown by the illuminated Earth cartoon.

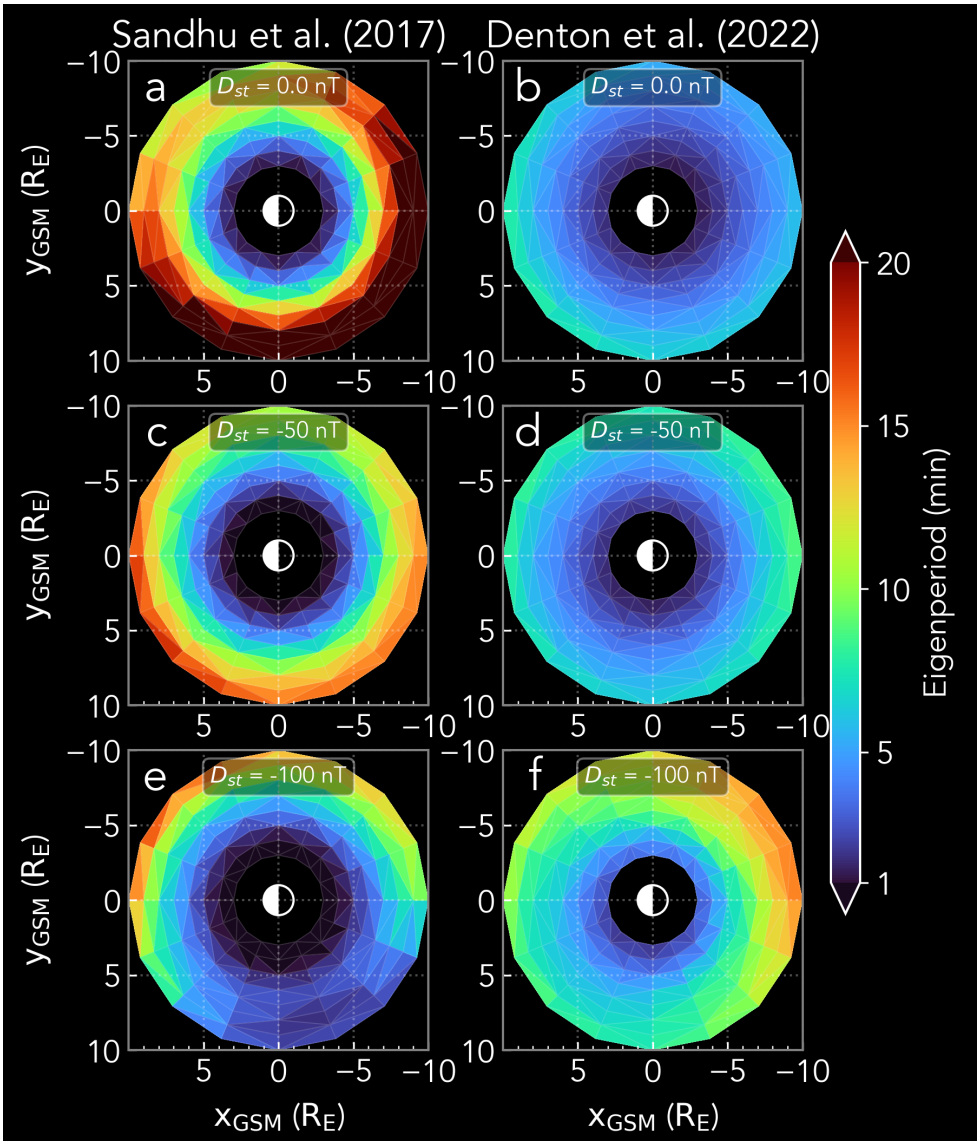

Figure 4.19: Equatorial plots of the $m = 1$ eigenperiods in GSM coordinates between 3 and 10 R_E, separated left-to-right by the plasma density model: (a), (c), (e) for Sandhu et al. (2017) and (b), (d), (f) for Denton et al. (2022). Vertically, the panels are labeled with the corresponding *Dst* index: (a), (b) for 0 nT, (c), (d) for -50 nT, and (e), (f) for -100 nT. The sunward direction is towards the left (positive x), also shown by the illuminated Earth cartoon.

negative deviation of the eigenperiods at $L = 10$.

The estimates of the fundamental eigenperiods using WKB approximation deviate significantly from the calculated $m = 1$ eigenperiods found by Singer et al. (1981) (Figure 4.21). The eigenperiods are generally larger than the transit time estimates by 40 to 70 percent inside of $6\,R_{\mathrm{E}}$ but can increase to 80 to 120 percent for the outermost field lines near $L = 10$. The deviations from Sandhu et al. (2017) (Panels 4.21a,c,e) are larger by $\sim$20% than at equivalent local times and radial distances in the Denton et al. (2022) model (Panels 4.21b,d,f). The deviations gradually increase from about 65% at $4.5\,R_{\mathrm{E}}$ to 80-120% in the Sandhu et al. (2017) model for all Dst. However, the local time with the largest deviations for $L > 6$ changes from post-dawn at quiet time (Panel 4.21a) to pre-dawn for weak geomagnetic activity (Panel 4.21c) to post-midnight at moderate geomagnetic activity. In contrast, the deviations in the Denton et al. (2022) model are largest at noon and smallest at midnight for $L > 5$ for all geomagnetic activity levels, and inside of $L = 5$ the decrease is 60% at $Dst = 0$ (Panel 4.21b) and 40% at $Dst = -100$ nT (Panel 4.21f).

We also investigated the effect of the power law index α (Equation 4.1) on the eigenperiods in the Denton et al. (2022) density model (Figure 4.22). Panels 4.22a-c show the electron densities against magnetic latitude (a), resulting eigenfrequencies versus L (b), and the deviations of the eigenperiods versus local time (c) between the models with $\alpha = 1$ (solid lines) and $\alpha = 2$ (dashed lines). Panels 4.22d-f compare the models with $\alpha = 1$ and $\alpha = 3$. Changing the power law index from 1 to 2 increases the eigenperiods by 5% at all local times and radial distances (Panel 4.22c), whereas increasing the power law index from 1 to 3 can lead to a 10% difference (Panel 4.22f).

We investigate the effects of varying the spread of the electron density distribution along the field line while keeping the total mass content of the field line constant (Figure 4.23). In the Panels a-c we show the effects of adding an equatorial electron density enhancement modeled as a Gaussian distribution at the equator with a width parameter σ (standard deviation of a Gaussian) of 1 and 2. The enhancement is added on top of the quiet-time

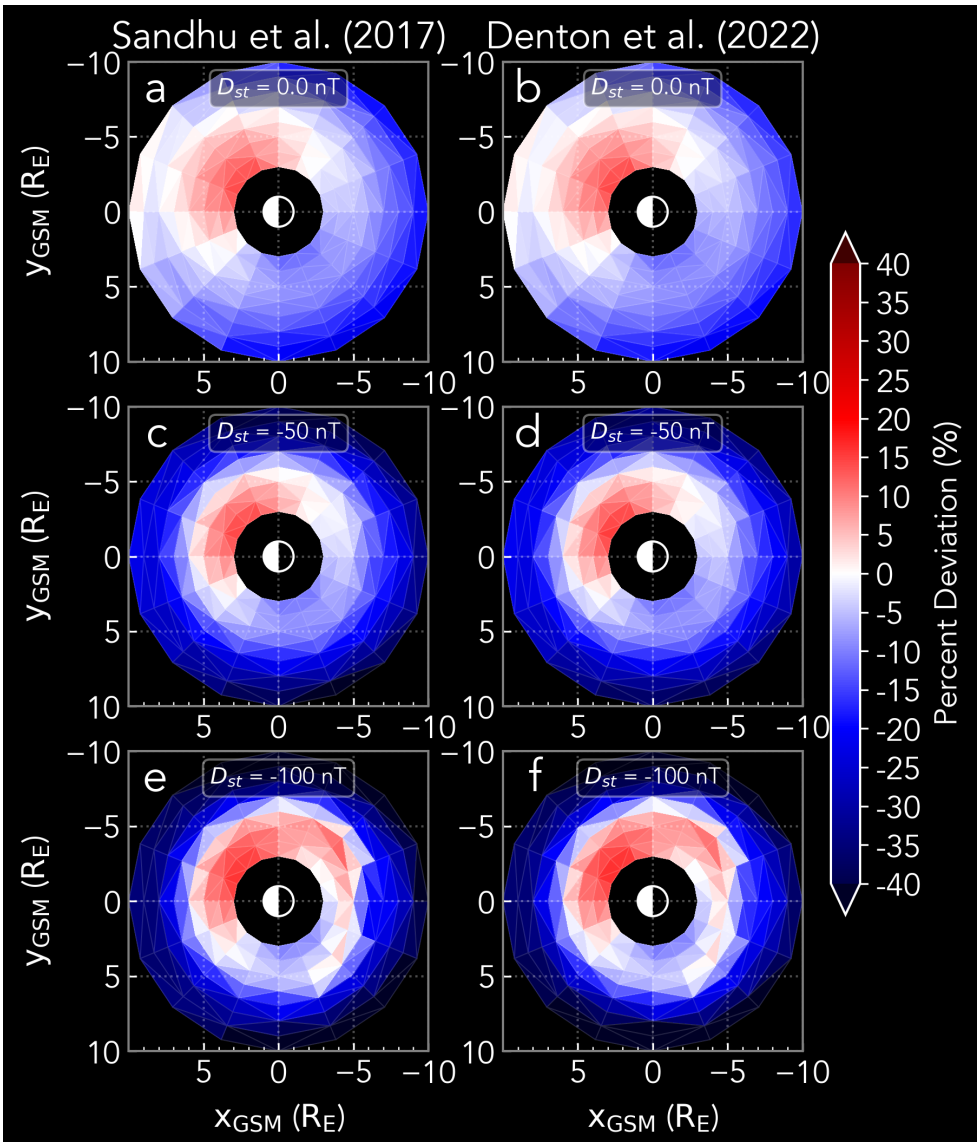

Figure 4.20: Equatorial plots of the $m = 1$ eigenperiod deviations between the eigenperiods calculated for T96 magnetic field model and dipole field lines at same equatorial positions in GSM coordinates between 3 and 10 R_E, separated left-to-right by the plasma density model: (a), (c), (e) for Sandhu et al. (2017) and (b), (d), (f) for Denton et al. (2022). Vertically, the panels are labeled with the corresponding Dst index: (a), (b) for 0 nT, (c), (d) for -50 nT, and (e), (f) for -100 nT. The sunward direction is towards the left (positive x), also shown by the illuminated Earth cartoon.

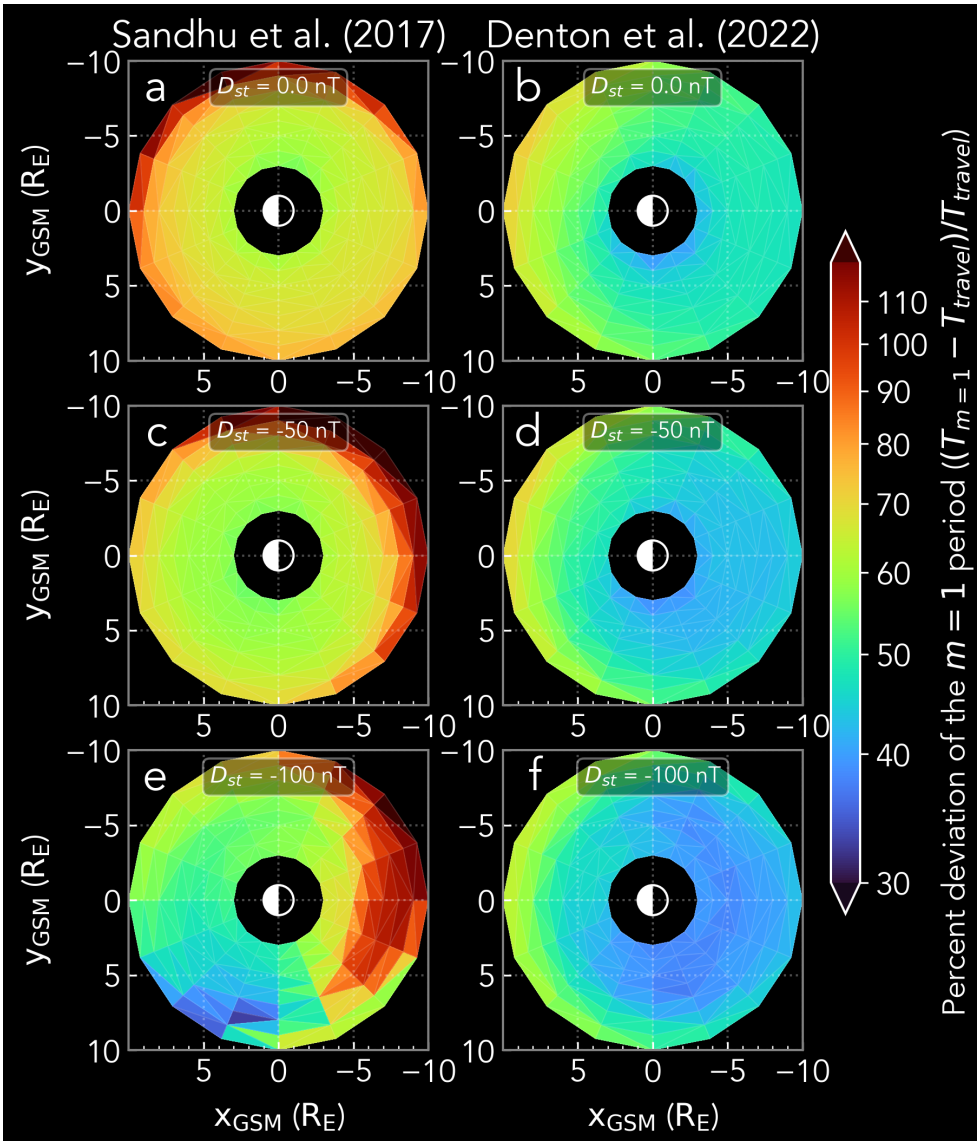

Figure 4.21: Equatorial plots of the deviations between the $m = 1$ eigenperiods and the estimates of the eigenperiods using the Alfvén transit time in GSM coordinates between 3 and 10 R_E, separated left-to-right by the plasma density model: (a), (c), (e) for Sandhu et al. (2017) and (b), (d), (f) for Denton et al. (2022). Vertically, the panels are labeled with the corresponding Dst index: (a), (b) for 0 nT, (c), (d) for -50 nT, and (e), (f) for -100 nT. The sunward direction is towards the left (positive x), also shown by the illuminated Earth cartoon.

values in the Denton et al. (2022) model. Panel 4.23a shows the electron density against magnetic latitude for field lines at $L = 5$, 7, and 9 in a quiet-time magnetotail, with $\sigma = 1$ enhancement represented by a solid line and $\sigma = 2$ by a dashed line. In this scenario, the amplitude of the enhancement is relatively strong – we add 20% of the total electron content along the respective field lines in the unchanged Denton et al. (2022) model with power law index $\alpha = 1$. Panel 4.23b shows the eigenfrequencies for the midnight field lines, and panel 4.23c visualizes the deviation of the eigenperiods between the two models with $\sigma = 1$ and $\sigma = 2$ in an equatorial plane between 3 and 10 R_{E}. Panels 4.23d-f show equivalent results but for a smaller enhancement amplitude of 10% of the total electron content along the field lines, and Panels 4.23g-i show the results for the same 10% enhancement but for enhancement distribution width parameter $\sigma = 2$ and $\sigma = 3$. The effect of redistributing the mass content of the enhancement is nearly uniform in local time and radial distance, leading to a decrease of the eigenperiods by 15% for a strong enhancement with σ changing from 2 to 1 (Panel 4.23c). For smaller equatorial electron density enhancements, the redistribution of the electron content leads to a decrease of the eigenperiods from 10% (Panel 4.23f) to less than 5% (Panel 4.23i).

4.4 Discussion

We have used realistic magnetic field and plasma density models to evaluate terrestrial field line eigenfrequencies for increasing levels of geomagnetic activity. The resulting eigenperiods in the two chosen density models differ by up to a factor of 2 for most levels of geomagnetic activity despite substantially different electron density and ion mass equatorial values. This illustrates the stronger dependence of the eigenperiods on the magnetic field model rather than the plasma density model.

The two plasma density models used in this study are both data-driven, yet they diverge significantly from each other. The S2017 model equatorial electron densities drop with

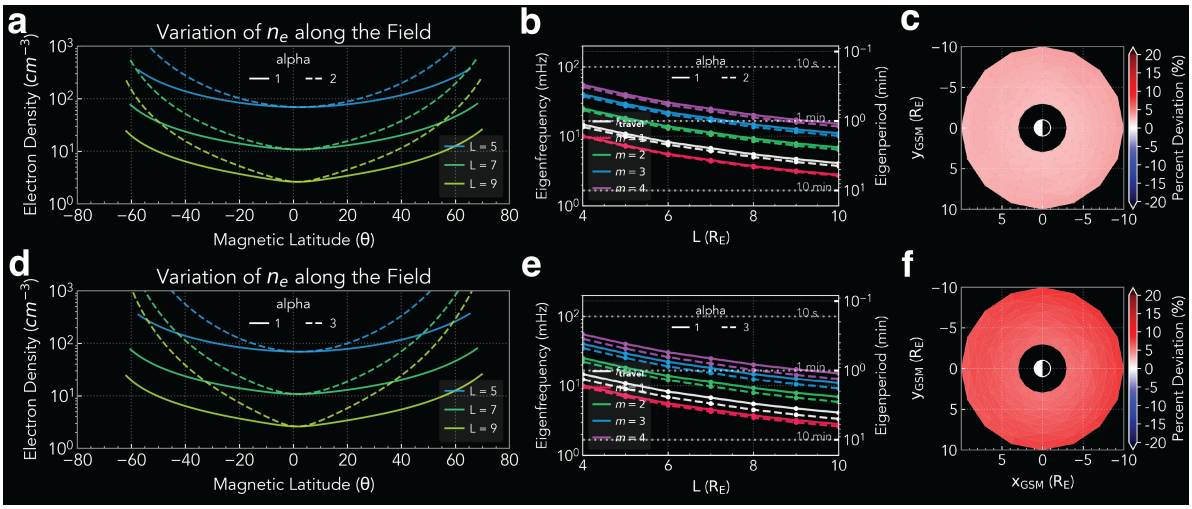

Figure 4.22: Midnight field lines between $L = 3$ and $L = 10$ for electron density power law index $\alpha = 1$ (a-c) and $\alpha = 2$ (d-f). Panels (a) and (b) show the electron density against magnetic latitude for reference field lines with $\alpha = 1$ (solid lines) and field lines with $\alpha = 2$ or 3 (dashed lines). Panels (b) and (e) show the eigenperiods of the first four harmonics (red, green, blue, and magenta lines) and the eigenperiod of the fundamental estimated from the Alfvén transit time (white lines). Panels (c) and (f) show deviations between the eigenperiods for field lines with $\alpha = 2$ or 3 and the reference eigenperiods with $\alpha = 1$. A red (positive) deviation indicates a larger eigenperiod for field lines with $\alpha = 2$ or 3 compared to field lines with a lower value of $\alpha = 1$ or 2.

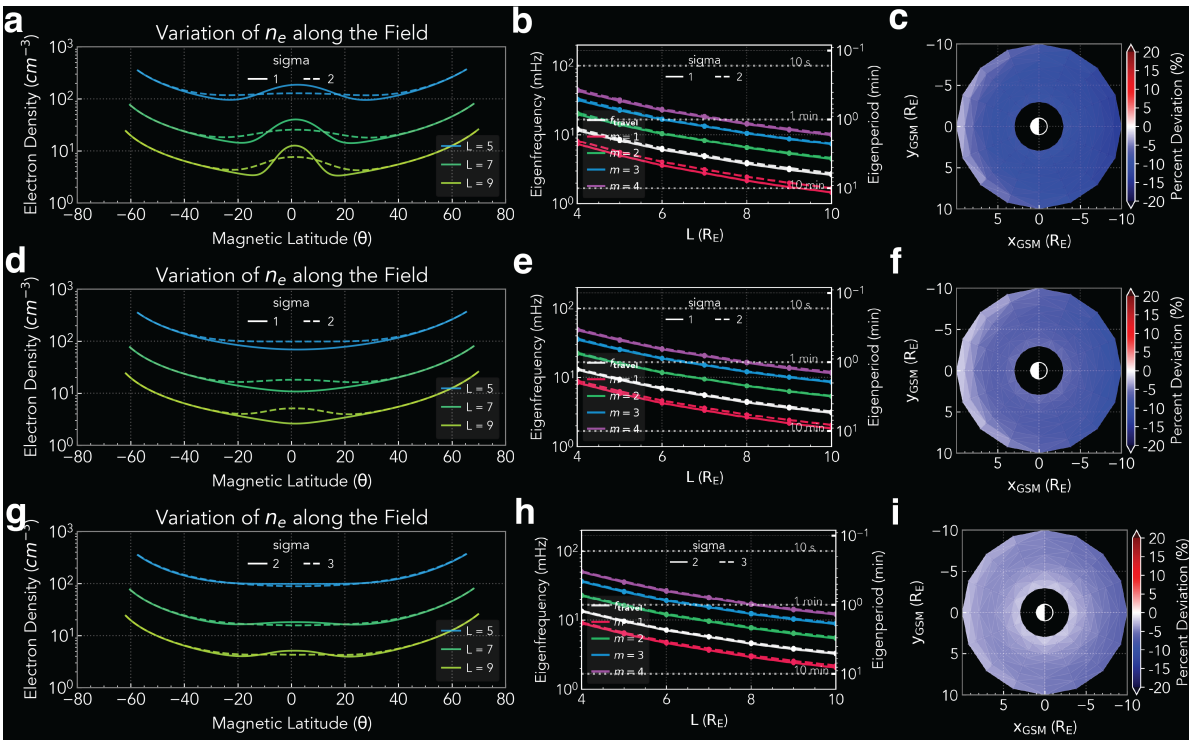

Figure 4.23: Midnight field lines between $L = 3$ and $L = 10$ for equatorial electron density enhancement width parameter (standard deviation of a normal distribution) $\sigma = 1$ and a high-amplitude enhancement (20% of the total field line electron content) (a-c), $\sigma = 1$ and a moderate-amplitude enhancement (10% of the total field line electron content) (d-f), and $\sigma = 2$ and a moderate-amplitude enhancement (10% of the total field line electron content) (d-f). Panels (a), (d), and (g) show the electron density against magnetic latitude for reference field lines with $\sigma = 1$ or 2 (solid lines) and field lines with $\sigma = 2$ or 3 (dashed lines). Panels (b), (e), and (h) show the eigenperiods of the first four harmonics (red, green, blue, and magenta lines) and the eigenperiod estimates using the Alfvén transit time (white lines). Panels (c), (f), and (i) show deviations between the eigenperiods for field lines with $\sigma = 2$ or 3 and reference eigenperiods with $\sigma = 1$ or 2 respectively. A blue (negative) deviation indicates a lower eigenperiod for field lines with $\sigma = 2$ or 3 compared to reference field lines with a lower value of $\sigma = 1$ or 2.

radial distance less quickly (from 20 cm^{-3} at $L = 5$ to 5 cm^{-3} at $L = 10$) than do the D2022 equatorial densities (40 cm^{-3} at $L = 5$ to 2 cm^{-3} at $L = 10$) for quiet-time magnetosphere (Figure 4.7a-b). As geomagnetic activity increases, the D2022 model remains more uniform as a function of MLT than does the S2017 model – there is a significant depletion of electron densities in the dusk region in the S2017 model at $Dst = -100$ nT, while D2022 shows a small enhancement in the densities in the pre-dusk region (Figures 4.7e-f). As Dst decreases, the D2022 electron densities do not show a significant change beyond the shift in the highest values towards the pre-dusk sector, whereas the S2017 density values drop at least by a factor of 2 between $Dst = -100$ nT and $Dst = 0$ nT. The closest the two models come to each other is at around equatorial field line crossing distance of $L = 6$ for most Dst and MLT values, but for $L < 6$ the S2017 model generally predicts lower densities than the D2022, and for $L > 6$ it predicts higher values.

The general decrease of electron densities with L is expected due to an increase of flux tube volume and length with higher L, as well as due to depletion of plasma by magnetotail processes (e.g. reconnection). This agrees with multiple previous observations (Sheeley et al., 2001; Denton et al., 2006). Sheeley et al. (2001) find no clear dependence of plasma number density with geomagnetic activity in the CRRES data between $L = 3$ to 7, however, there is a significant dependence on Dst in the S2017 model. Sandhu et al. (2017) attributes the depletion of electron densities at fixed L with decreasing Dst to multiple processes such as reduced refilling rates of the plasmaspheric electrons with Dst (Denton, 2002; Denton et al., 2006), earthward motion of the plasmapause, and erosion of the plasmasphere due to enhanced ring currents. The enhanced ring currents during active geomagnetic times is also suggested to cause the electrons to move into open drift paths that would lose them to the magnetopause (Sandhu et al., 2017).

The depletion of the electron densities in the S2017 model at dusk for $Dst = -100$ nT is attributed to the "plasmaspheric bulge" moving approximately from dusk to noon with decreasing Dst (Sandhu et al., 2017). However, such strong depletions and MLT asymmetries

are not present in the D2022 model (Figure 4.7f). In fact, there is an enhancement of the electron densities in the pre-dusk sector in the D2022 model at almost the same location whereas there is a depletion in the S2017 model. Such pre-dusk enhancement can also be seen in the statistical survey of the plasma densities observed by the THEMIS mission reported by Li et al. (2010). Li et al. (2010) reports the largest plasma densities on the dayside, peaking in the post-noon region due to the presence of plasmaspheric plumes (see Figure 1a, Li et al., 2010). Li et al. (2010) also observe an increase of night-side equatorial plasma densities for L between 6 and 8 compared to the quiet time, though such enhancements, suggested to be due to injection of plasma sheet electrons, are not seen in either of the models chosen in this study. Nevertheless, the D2022 density model values are close to the observations of Li et al. (2010), and therefore, it may be the more reliable estimate of the plasma density (at least for a quiet-time magnetosphere).

The equatorial ion mass values differ significantly between the S2017 and D2022 models at all levels of geomagnetic activity (Figure 4.8). The ion mass enhancement peaks in the post-dusk region in the S2017 model, and in the post-midnight region in the D2022 model. Except for the moderate geomagnetic activity of $Dst = -100$ nT, the ion mass increases with decreasing L in Sandhu et al. (2017). Sandhu et al. (2016) attribute this to mass dispersion effects that make heavier ions convect to lower L values than the lighter ions. The heavy ion torus outside the plasmasphere is also suggested to play some role (Sandhu et al., 2016). This enhancement of ion mass near the plasmasphere reaching 16 amu is not found in the D2022 model. At quiet times, the average ion mass in the D2022 model is approximately 1 amu at all radial distances (Figure 4.8b), and with decreasing Dst the outer post-midnight sector has an ion mass enhancement of up to 18 amu.

The electron density and average ion mass distributions are approximated by using a power law varying with radial distance (Equation 4.1) in both models. A positive power law index (α) is commonly used for the electron density distribution (Cummings et al., 1969; Goldstein et al., 2001; Denton et al., 2006). Our implementation of the D2022 model has

constant power law index ($\alpha = 1$) for the electron density that is a good first-order approximation to the electron distribution with radial distance (Denton, private communication). In addition to the power law, Sandhu et al. (2017) use an equatorial Gaussian enhancement that is most intense at large L in the magnetotail (Equation 4.4). Equatorial mass density enhancements have been noted before: Denton et al. (2006) found mass density depletion off the magnetic equator with decreasing Dst index. The equator-peaked distributions for disturbed conditions were due to the depletion of plasmaspheric electron density and enhanced ring current (Denton et al., 2006). Equatorial enhancements of the average ion mass are also expected due to centrifugal forces, which affect the heavier ions more than the lighter ones in stretched regions of magnetic field (Takahashi, 2004; Denton et al., 2006). The equatorial average ion mass enhancement is particularly visible in the noon-midnight meridian plot of field lines in the S2017 model (Figure 4.10a). In comparison, electron densities in the D2022 model change gradually along the field with $\alpha = 1$ (Figure 4.9b,d,f). The average ion mass is held constant along the field with $\alpha = 0$ for simplicity, which makes the ion mass dependent only on the equatorial value at the field line crossing point (panels 4.10b,d,f)

We combined the electron density and the ion mass distributions along the field lines to calculate the mass density and the resulting Alfvén velocity along the field (Figure 4.11). Since the Alfvén speed is proportional to $B/\sqrt{\rho}$, it is more sensitive to the variation in the magnetic field magnitude (B) than to the mass density (ρ). This explains why the Alfvén velocities in the noon-midnight meridian do not differ significantly between the two density models: they both result in a thin plasma sheet region of $1\,R_{\mathrm{E}}$ thickness at the equator with Alfvén velocity of $\sim$100km/s for $L > 5$ (Figure 4.11). The Alfvén velocities are generally greater in the Denton et al. (2022) model (panels 4.11b,d,f) than in the Sandhu et al. (2017) model (panels 4.11a,c,e), which is the one of the main reasons for higher-frequency harmonics in the Denton et al. (2022) model (compare Figures 4.12 and 4.15, for example). The profiles of Alfvén velocities along the field lines are otherwise similar for two models, owing to the significant contribution to Alfvén velocities of the strength of the magnetic field.

The stronger influence of the magnetic field model over the plasma density models can also be seen by comparing the fundamental eigenperiods between the models. In the quiet-time magnetosphere, the difference is insignificant at most MLT, but in the pre-noon sector it is as high as 20% for all geomagnetic activity levels and for both density models (Figure 4.20). For moderate geomagnetic activity ($Dst = -100$ nT), the positive deviation of the fundamental eigenperiod is present at other local times up to $5\,R_{\mathrm{E}}$ but is still strongest in the pre-noon sector (Panels 4.20e-f). A dipole field is a close approximation at geosynchronous orbit (leading to eigenperiods correct within 5% at $L = 6$) but can lead to significant eigenperiod error inside of $L = 6$, especially in the pre-noon sector, which might be due to more distorted magnetic field lines at this local time. The eigenperiods calculated in a dipole field are up to 20% lower than in the T96 model. Outside of $L = 6$, the magnetic field lines typically are stretched/lengthened compared to dipolar field lines, resulting in rapid decrease of the T96 eigenperiods with L. The deviation at $L = 10$ increases from ∼20% at quiet-time (Panels 4.20a-b) to nearly 50% in the presence of moderate geomagnetic activity (Panels 4.20e-f). Therefore, we recommend the use of a realistic magnetic field model (such as T96) for calculations of field line resonances at all radial distances, even inside of $L = 6$.

As expected from looking at the generally higher Alfvén velocities in the D2022 model (Figure 4.11), the calculated fundamental eigenperiod is typically lower in the D2022 model than in the S2017 model, especially at $L > 6$ (Figure 4.19). In the D2022 model, the eigenperiods for field lines between $L = 5$ and $L = 10$ range between 5 and 15 minutes, but in the S2017 model the eigenperiods remain close to 15-20 min at $L = 10$, except near dusk for Dst = -100 nT where the eigenperiods drop to a few minutes (Figure 4.19e) due to a depletion of electron densities (see Figure 4.7e). In contrast, the eigenperiods in the D2022 model have a MLT minimum pre-dusk for moderate geomagnetic activity (Figure 4.10f), and are within 30-50% of the S2017 model eigenperiods at most MLT and L. At quieter time, when Dst is only slightly negative, the eigenperiods in D2022 model are lower than in the Sandhu2017 model by a factor of 2 or more (Panels 4.19b,d). Comparing these results to the

THEMIS observations of Pc5-6 waves by Takahashi et al. (2015) and Zhang et al. (2018), we find the eigenperiods in the Denton2022 model match the observations more closely. Both Takahashi et al. (2015) and Zhang et al. (2018) find the typical period of ULF waves at $L = 5$ to be around 3 min, and roughly 6 min at $L = 10$. Except for the moderate geomagnetic activity, these eigenperiods are very close to those calculated in the D2022 model (see Figure 4.19).

We find that with increasing geomagnetic activity, the eigenperiods generally increase in the D2022 model for $L > 5$. This is likely due to a significant increase in the ion mass for more negative Dst. However, the ULF waves observed by Zhang et al. (2018) closer to storm time have slightly lower periods than non-storm-time waves by a few minutes or more. The eigenperiods calculated in the S2017 model generally decrease with geomagnetic activity, but the resulting periods are still higher than the typical observed periods by Takahashi et al. (2015) and Zhang et al. (2018). These disagreements between the models and observations remain a subject for further study.

THEMIS observations of ULF waves at dusk and midnight indicate that for $L > 10$ the observed Pc5-6 periods vary little with L (Takahashi et al., 2015; Zhang et al., 2018). We find a reduced eigenperiod dependency on L calculated in the region of $L > 8$, especially at moderate geomagnetic activity when the field is substantially stretched. Since the effect occurs for both density models (although more pronounced for the S2017 model), we conclude that the stretched field configuration is the main contributor to this effect. A similar behavior has been reported at Saturn, where the 60-min-period field line resonances occur at large regions of the outer magnetosphere (Rusaitis et al., 2021). Once the terrestrial plasma density models extending beyond $L = 10$ become available, it would be insightful to test if the observed ULF periods in the magnetotail can be reproduced.

A common approximation for calculating field line resonance periods is to use the WKB method (e.g. Sandhu et al., 2018; Takahashi et al., 2016). Comparing the $m = 1$ eigenperiod to the estimate of the fundamental using the WKB approach in both plasma density models

and increasing levels of geomagnetic activity (Figure 4.21), we find that the deviation between the two eigenperiods is typically between 40% and 100%. The difference is smaller closer to the planet than further out, but can vary with geomagnetic activity, which can significantly distort the field lines. Therefore, the WKB approximation should only be used as a rough estimate of the period.

One of the main uncertainties in our implementation of D2022 model is the choice of the power law index α for the variation of mass density along the field line. Although $\alpha = 1$ is expected to be a good approximation (Denton, private communication), we investigated the effects of varying α from 1 to 2 and 3. Figure 4.22c shows the deviation of fundamental eigenperiods between field lines with $\alpha = 1$ and $\alpha = 2$. The deviation is relatively small, within 5% for all MLT and radial distances. This deviation increases up to 10-15% when comparing field lines with $\alpha = 1$ and $\alpha = 3$ (Figure 4.22f). Nevertheless, we conclude that the choice of the power law index is less important to the correct estimation of field line resonance eigenperiods than the use of a realistic field model or using the wave equation of Singer et al. (1981) for calculation of eigenperiods. The error in eigenperiods due to the choice of α is expected to be within 5% to 15%, whereas the error due to a dipole field instead of a more realistic field model can range from 20% to 50% (Figure 4.20). The relatively small error due to a varying the power law index is primarily because of the equatorial plasma density is more important to the eigenperiod than the off-equator plasma. At the magnetic equator, the weak magnetic field leads to the lowest Alfvén speed along the field lines. We expect small differences of these errors with other choices of plasma density models and magnetospheric field models, but the relative size of these errors should remain similar.

Redistributing the equatorial mass density along the field line can also lead to significant deviations in eigenperiods. We investigated this by introducing a Gaussian equatorial electron density enhancement on top of the D2022 model with a power law index $\alpha = 1$, and varying the width of this enhancement along the field while keeping the total mass content constant. As expected, when more of the mass content is redistributed to higher latitudes

where the field is stronger, the eigenperiods decrease by 5% to 15% depending on the amplitude of the equatorial enhancement. For an equatorial electron density enhancement of 20% of the total electron content along the field line, the electron density distribution against magnetic latitude (Figure 4.23a) is like the density distributions seen in the S2017 model (Figure 4.12b). Changing the width of the enhancement σ (standard deviation) from 1 to 2 leads to an eigenperiod decrease by 20% (Panel 4.23c). For a lower equatorial enhancement (10% of the total electron content along the field line), the eigenperiod deviation is abount 10% smaller (Panel 4.23f). As seen in the Sandhu2017 model, the amplitude and width of such an equatorial enhancement changes significantly with L, MLT, and geomagnetic activity (see Figures 4.12-4.14), and such strong variations of mass density along the field can lead to significant errors in the field line eigenperiods if the distribution along the field is not chosen correctly. However, we are not certain how common such large deviations of mass density along the field lines are in a typical magnetosphere, as most plasma density models are constructed from near-equatorial measurements (e.g., Li et al., 2010). However, as long as the equatorial electron density and average ion mass are known well, the off-equatorial distribution of mass density should not lead to errors much greater than 20%, as seen in our investigation of the power law index in Figure 4.22.

4.5 Summary

To summarize, we have investigated field line resonances at Earth in a realistic field model up to $L = 10$ for two data-derived plasma density models and varying levels of geomagnetic activity. We closely reproduced the eigenperiods reported by in-situ THEMIS observations using the Denton et al. (2022) density model for quiet-time and weak geomagnetic activity.

Generally, the eigenperiods of the fundamental are found to increase with L from a few min at $L = 5$ to between 5 and 15 min at $L = 10$. Between $L = 8$ and $L = 10$, the eigenperiods show reduced dependency on L, especially at moderate geomagnetic activity. As

for the eigenperiod variation with L for $L > 10$, we lack a reliable plasma density model and can only speculate that the eigenperiods would change less with L than closer to the planet. If the plasma density models we investigated can be extrapolated, then the trend we see in the eigenperiods between $L = 8$ and $L = 10$ might continue, reducing the variation of the eigenperiod with L. That would be compatible with some of the ULF observations between $L = 10$ and $L = 30$ that detect a reduced dependence of the frequency with equatorial crossing distance of the field lines (e.g., Takahashi et al., 2015; Zhang et al., 2018). This is likely due to the stretched magnetic field in the tail together with gradually lower equatorial plasma densities with L which keeps the Alfvén velocities nearly constant at the equator with radial distance. A similar lack of eigenperiod variation with L is observed at Saturn between $10\,R_S$ and $20\,R_S$ (Rusaitis et al., 2021).

Additionally, we have evaluated the effects of several common approximations on the eigenperiods of field line resonances. We found that both dipole-field and WKB approximations can result in significant errors in the estimates of eigenperiods even inside of $L = 6$. WKB and dipole-field approximation should only be used for a rough estimation of the eigenperiods.

The greatest uncertainty in using the Denton et al. (2022) came from assuming the power law index (α, equation 4.1) for the distribution of mass density. As suggested by Denton (private communication), we assumed $\alpha = 1$, but we found little effect on the eigenperiods from assuming $\alpha = 2$. We have not investigated a flat distribution of the mass density along the field, but we suspect it would not have a significant effect on the eigeneperiods.

A more thorough comparison between the calculated eigenperiods for increasing levels of geomagnetic activity and the Pc5-6 ULF observations remains to be completed. A following study will compare the eigenperiods in D2022 model with the recently updated THEMIS ULF database (Hartinger, private communication).

CHAPTER 5

Summary and Ongoing Work

It is the mark of an educated mind to be able to entertain a thought without accepting it.

— *Aristotle*

Despite the differences in size, rotational velocities, and plasma distribution, the magnetospheres of Saturn and Earth exhibit multi-harmonic resonances along field lines in a wide range of local times and radial distances. We have modeled field line resonances in both magnetospheres and have reproduced many of their observed properties.

In chapter 2, we modeled the quasiperiodic 60-min waves observed in Saturn's outer magnetosphere by using Alfvén wave resonance theory in a realistic magnetic field model and data-driven plasma density distribution. The modeled eigenfrequencies for the second and higher modes were found to be independent of invariant latitude, map to large regions of the magnetosphere (least to $20\,R_S$), with the fourth harmonic modes having close to 1-hour eigenperiods. The model predicted that the normalized amplitudes for these modes in the magnetic field at high latitudes would exceed their amplitudes in the plasma sheet, in agreement with the observations of more frequent occurrences at mid-to-high latitudes.

Using 13 years of the Cassini magnetometer data from Saturn's magnetosphere, we detected signatures of quasiperiodic pulsations corresponding with periodicities around 30 minutes (QP30), 60 minutes (QP60), and 120 minutes (QP120), which closely match to the

lowest even harmonics of the field line resonance model in a realistic magnetic field/plasma density configuration. Chapter 3 describes the details and findings of this study. We found the quasi-periodic waves come in wave trains of 4-to-5 hours before decaying in amplitude, and reoccur in the magnetic field data at the rate of planetary period ocillations (10.7 h). Judging by the highest relative power of the quasi-periodic waves in the post-dusk sector and inside of 25 R_S, we suggest that these even-mode harmonics of Saturn's magnetic field lines are excited by the periodic vertical flapping of Saturn's magnetotail.

In chapter 4, we adapted our field line resonance model to Earth's magnetosphere using the Tsyganenko (1996) magnetic field model and several plasma density models. We examined the wave modes for increasing levels of geomagnetic activity and compared the eigenperiods to the ULF wave periods observed by the THEMIS mission. We found a close match between the eigenperiods calculated in the Denton et al. (2022) model and the Pc5-6 waves reported by Takahashi et al. (2015) and Zhang et al. (2018), agreeing within roughly 20-30% for quiet-time and weak geomagnetic activity. A more thorough comparison of the eigenperiods with an updated THEMIS ULF wave database for different levels of Dst (Hartinger, private communication) will be completed in a follow up study. It will help us understand if the eigenperiods of field line resonances should decrease or increase with higher levels of geomagnetic activity since in our study, the eigenperiods increased with lower Dst in the D2022 model, but generally decreased in the S2017 model. There is some observational evidence that storm-time ULF waves have lower eigenperiods than non-storm-time (Zhang et al., 2018), perhaps due to plasma mass depletion and dipolarization of the field lines. Our follow up study will address this question in more detail.

The distribution of mass density along the field was found to be less important in the eigenperiod calculations than the equatorial plasma mass or the field line geometry. Since the detected ultralow frequency (ULF) waves in the Pc4 and Pc5 bands can be used for inferring the mass content of the field lines, the results quantify the main uncertainties in using that technique.

The field line resonances at Earth in this dissertation have been modeled up to $L = 10$, constrained by the radial validity of the plasma density models, but there is a growing number of observations of standing-wave like structures in the magnetotail region up to $30\,R_{\mathrm{E}}$ (Takahashi et al., 2015; Zhang et al., 2018). The observed ULF waves in the magnetotail have reduced dependence on the invariant latitude (or the equatorial crossing point of the field line), similar to the observed and modeled eigenfrequencies in Saturn's outer magnetosphere from 10 to $20\,R_{\mathrm{S}}$ (Rusaitis et al., 2021). Our results show mostly decreasing eigenfrequencies with increasing L between $L = 3$ and $L = 8$, but between $L = 8$ and $L = 10$ the eigenperiods show a reduced dependence on L, especially at moderate geomagnetic activity. We do not have a reliable plasma density model past $L = 10$ to verify if this behavior is reproducible for field lines deeper in the magnetotail. It would be worthwhile to investigate the resulting eigenperiods once a reliable plasma density model for $L > 10$ becomes available. We suspect this lack of eigenperiod dependence on L further down the tail comes primarily from the effects of a stretched magnetic field, as well as gradually decreasing equatorial plasma density with radial distance. As a result, the Alfvén velocity near the equator is roughly constant with radial distance. This is like the the case at Saturn where the QP60 waves are found over a large region of outer magnetosphere.

It is important to note some key differences between the two magnetospheres. The combined effects of rapid rotation and shear size of the gas giants lead to important centrifugal forces that vastly exceed those of Earth. In the Kronian magnetosphere, there are significant sources of plasma and dust from the moon Enceladus. The mass loading from Enceladus and the centrifugal forces lead to the mass density distribution along the field being considerably different than that at Earth. This tightly confines the nodes of the harmonics of field line resonances within the plasma sheet (within $\pm 10^{\circ}$ magnetic latitude, see Rusaitis et al., 2021). The IMF at Saturn is probably not as effective in coupling the solar-wind momentum and energy to the magnetosphere as at Earth, because the magnetic pressure provides a weaker contribution to the total pressure in the magnetosheath (Russell et al.,

2016). Therefore, we are convinced by the regular modulation of the QP waves at Saturn at the PPO period that the associated field line resonances are driven internally. At Earth, due to the stronger influence of the solar wind, it is likely that most of the field line resonances are driven externally by processes such as perturbations in the solar wind dynamic pressure (Claudepierre et al., 2010; Ellington et al., 2016).

Our study is not without limitations – our work was limited to many of the approximations used by Singer et al. (1981). We have assumed a perfectly conducted ionosphere, ignoring the development and decay of the standing Alfvén waves. Our solutions for the toroidal and poloidal modes were also uncoupled, simplifying the numerical calculation. Nevertheless, we believe these approximations are justified for understanding the basic properties of field line resonances at Earth and Saturn.

Recently, there have been significant developments in the 3D field line resonance theory that cannot be ignored. Claudepierre et al. (2010) were the first to show that solar-wind driven toroidal mode field line resonances can develop in a self-consistent, global MHD. However, coupled MHD waves in a realistic magnetic geometry have many difficulties, and treatment of the ionosphere in the MHD model is non-trivial, since the ionosphere plays an important role in the structure and evolution of FLRs (Ellington et al., 2016). Wright and Elsden (2020) investigated the propagation and coupling of MHD waves in a modified dipole coordinate system, showing that FLRs can cross L shells with a polarization that is neither toroidal or poloidal. More recently, a comprehensive study of global MHD simulations of resonant waves excited by solar wind pulses has been published by Archer et al. (2022). They found many aspects of the standing Alfvén modes agreeing with the box and axially symmetric dipole models. However, additional nodes along field lines were found in the perpendicular and compressional components of the magnetic field that are not present in the displacement/velocity. It would be worthwhile to use the self-consistent fields and plasma densities of these MHD models and investigate the similarities and differences of the resulting eigenmodes with the approach used in this dissertation.

References

Alfvén, H. (1942a). Existence of electromagnetic-hydrodynamic waves. *Nature*, *150*(3805), 405–406. doi: 10.1038/150405d0

Alfvén, H. (1942b). On the existence of electromagnetic-hydrodynamic waves. *Arkiv för matematik, astronomi och fysik*, *29B(2)*, 1–7.

Archer, M. O., Southwood, D. J., Hartinger, M. D., Rastaetter, L., & Wright, A. N. (2022). How a realistic magnetosphere alters the polarizations of surface, fast magnetosonic, and Alfvén waves. *Journal of Geophysical Research: Space Physics*, *127*(2). doi: 10.1029/2021JA030032

Arridge, C. S., André, N., Khurana, K. K., Russell, C. T., Cowley, S. W. H., Provan, G., ... Young, D. T. (2011). Periodic motion of Saturn's nightside plasma sheet. *Journal of Geophysical Research: Space Physics*, *116*(A11). doi: 10.1029/2011JA016827

Arridge, C. S., Russell, C. T., Khurana, K. K., Achilleos, N., Cowley, S. W. H., Dougherty, M. K., ... Bunce, E. J. (2008). Saturn's magnetodisc current sheet. *Journal of Geophysical Research: Space Physics*, *113*(A4). doi: 10.1029/2007JA012540

Bader, A., Badman, S. V., Yao, Z. H., Kinrade, J., & Pryor, W. R. (2019). Observations of continuous quasiperiodic auroral pulsations on Saturn in high time-resolution UV auroral imagery. *Journal of Geophysical Research: Space Physics*, 2018JA026320. doi: 10.1029/2018JA026320

Bagenal, F., Adriani, A., Allegrini, F., Bolton, S. J., Bonfond, B., Bunce, E. J., ... Zarka, P. (2017). Magnetospheric science objectives of the Juno mission. *Space Science Reviews*, *213*(1-4), 219–287. doi: 10.1007/s11214-014-0036-8

Bagenal, F., & Delamere, P. A. (2011). Flow of mass and energy in the magnetospheres of Jupiter and Saturn. *Journal of Geophysical Research: Space Physics*, *116*(A5). doi: 10.1029/2010JA016294

Borovsky, J. E., & Shprits, Y. Y. (2017). Is the *Dst* index sufficient to define all geospace

storms? *Journal of Geophysical Research: Space Physics*, *122*(11). doi: 10.1002/2017JA024679

Bunce, E. J., Cowley, S. W. H., & Milan, S. E. (2005). Interplanetary magnetic field control of Saturn's polar cusp aurora. *Annales Geophysicae*, *23*(4), 1405–1431. doi: 10.5194/angeo-23-1405-2005

Bunce, E. J., Grodent, D. C., Jinks, S. L., Andrews, D. J., Badman, S. V., Coates, A. J., ... Provan, G. (2014). Cassini nightside observations of the oscillatory motion of Saturn's northern auroral oval. *Journal of Geophysical Research: Space Physics*, *119*(5), 3528–3543. doi: 10.1002/2013JA019527

Cao, H., Russell, C. T., Christensen, U. R., Dougherty, M. K., & Burton, M. E. (2011). Saturn's very axisymmetric magnetic field: No detectable secular variation or tilt. *Earth and Planetary Science Letters*, *304*(1-2), 22–28. doi: 10.1016/j.epsl.2011.02.035

Cao, H., Russell, C. T., Wicht, J., Christensen, U. R., & Dougherty, M. K. (2012). Saturn's high degree magnetic moments: Evidence for a unique planetary dynamo. *Icarus*, *221*(1), 388–394. doi: 10.1016/j.icarus.2012.08.007

Carbary, J. F., Kurth, W. S., & Mitchell, D. G. (2016). Short periodicities in low-frequency plasma waves at Saturn. *Journal of Geophysical Research: Space Physics*, *121*(7), 6562–6572. doi: 10.1002/2016JA022732

Chen, L., & Hasegawa, A. (1974). A theory of long-period magnetic pulsations: 1. Steady state excitation of field line resonance. *Journal of Geophysical Research*, *79*(7), 1024–1032. doi: 10.1029/JA079i007p01024

Claudepierre, S. G., Hudson, M. K., Lotko, W., Lyon, J. G., & Denton, R. E. (2010). Solar wind driving of magnetospheric ULF waves: Field line resonances driven by dynamic pressure fluctuations. *Journal of Geophysical Research: Space Physics*, *115*(A11). doi: 10.1029/2010JA015399

Cramm, R., Glassmeier, K.-H., Stellmacher, M., & Othmer, C. (1998). Evidence for resonant mode coupling in Saturn's magnetosphere. *Journal of Geophysical Research: Space*

Physics, *103*(A6), 11951–11960. doi: 10.1029/98JA00629

Cummings, W. D., O'Sullivan, R. J., & Coleman, P. J. (1969). Standing Alfvén waves in the magnetosphere. *Journal of Geophysical Research*, *74*(3), 778–793. doi: 10.1029/JA074i003p00778

Delamere, P. A., Otto, A., Ma, X., Bagenal, F., & Wilson, R. J. (2015). Magnetic flux circulation in the rotationally driven giant magnetospheres. *Journal of Geophysical Research: Space Physics*, *120*(6), 4229–4245. doi: 10.1002/2015JA021036

Denton, R. E. (2002). Magnetospheric electron density model inferred from Polar plasma wave data. *Journal of Geophysical Research*, *107*(A11), 1386. doi: 10.1029/2001JA009136

Denton, R. E., Goldstein, J., & Menietti, J. D. (2002). Field line dependence of magnetospheric electron density. *Geophysical Research Letters*, *29*(24), 58-1-58-4. doi: 10.1029/2002GL015963

Denton, R. E., Takahashi, K., Galkin, I. A., Nsumei, P. A., Huang, X., Reinisch, B. W., ... Hughes, W. J. (2006). Distribution of density along magnetospheric field lines. *Journal of Geophysical Research*, *111*(A4), A04213. doi: 10.1029/2005JA011414

Denton, R. E., Takahashi, K., Min, K., Hartley, D., & Nishimura, Y. (2022). Models for magnetospheric mass density. In *Geospace Environment Modeling.* Hawaii.

Dougherty, M. K., Cao, H., Khurana, K. K., Hunt, G. J., Provan, G., Kellock, S., ... Southwood, D. J. (2018). Saturn's magnetic field revealed by the Cassini Grand Finale. *Science*, *362*(6410), eaat5434. doi: 10.1126/science.aat5434

Dougherty, M. K., Kellock, S., Southwood, D. J., Balogh, A., Smith, E. J., Tsurutani, B. T., ... Cowley, S. W. H. (2004). The Cassini magnetic field investigation. *Space Science Reviews*, *114*(1-4), 331–383. doi: 10.1007/s11214-004-1432-2

Dougherty, M. K., Khurana, K. K., Neubauer, F. M., Russell, C. T., Saur, J., Leisner, J. S., & Burton, M. E. (2006). Identification of a dynamic atmosphere at Enceladus with the Cassini magnetometer. *Science*, *311*(5766), 1406–1409. doi: 10.1126/science.1120985

Dungey, J. W. (1955). Electrodynamics of the outer atmosphere. In *Physics of the Ionosphere* (p. 229). The Physical Society, London.

Ellington, S. M., Moldwin, M. B., & Liemohn, M. W. (2016). Local time asymmetries and toroidal field line resonances: Global magnetospheric modeling in SWMF. *Journal of Geophysical Research: Space Physics*, *121*(3), 2033–2045. doi: 10.1002/2015JA021920

Ferrière, K. M., Zimmer, C., & Blanc, M. (1999). Magnetohydrodynamic waves and gravitational/centrifugal instability in rotating systems. *Journal of Geophysical Research: Space Physics*, *104*(A8), 17335–17356. doi: 10.1029/1999JA900167

Fujita, S., Glassmeier, K.-H., & Kamide, K. (1996). MHD waves generated by the Kelvin-Helmholtz instability in a nonuniform magnetosphere. *Journal of Geophysical Research: Space Physics*, *101*(A12), 27317–27325. doi: 10.1029/96JA02676

Galopeau, P. H. M., & Lecacheux, A. (2000). Variations of Saturn's radio rotation period measured at kilometer wavelengths. *Journal of Geophysical Research: Space Physics*, *105*(A6), 13089–13101. doi: 10.1029/1999JA005089

Glassmeier, K.-H., Klimushkin, D., Othmer, C., & Mager, P. (2004). ULF waves at Mercury: Earth, the giants, and their little brother compared. *Advances in Space Research*, *33*(11), 1875–1883. doi: 10.1016/j.asr.2003.04.047

Glassmeier, K.-H., Ness, N. F., Acuña, M. H., & Neubauer, F. M. (1989). Standing hydromagnetic waves in the Io plasma torus: Voyager 1 observations. *Journal of Geophysical Research*, *94*(A11), 15063. doi: 10.1029/JA094iA11p15063

Glassmeier, K.-H., Othmer, C., Cramm, R., Stellmacher, M., & Engebretson, M. (1999). Magnetospheric field line resonances: A comparative planetology approach. *Surveys in Geophysics*, *20*(1), 61–109. doi: 10.1023/A:1006659717963

Goldstein, J., Denton, R. E., Hudson, M. K., Miftakhova, E. G., Young, S. L., Menietti, J. D., & Gallagher, D. L. (2001). Latitudinal density dependence of magnetic field lines inferred from Polar plasma wave data. *Journal of Geophysical Research: Space Physics*, *106*(A4), 6195–6201. doi: 10.1029/2000JA000068

Guo, R. L., Yao, Z. H., Wei, Y., Ray, L. C., Rae, I. J., Arridge, C. S., ... Dougherty, M. K. (2018). Rotationally driven magnetic reconnection in Saturn's dayside. *Nature Astronomy*, *2*(8), 640–645. doi: 10.1038/s41550-018-0461-9

Gurnett, D. A., Kurth, W. S., Hospodarsky, G. B., Persoon, A. M., Averkamp, T. F., Cecconi, B., ... Pedersen, A. (2005). Radio and plasma wave observations at Saturn from Cassini's approach and first orbit. *Science*, *307*(5713), 1255–1259. doi: 10.1126/science.1105356

Gurnett, D. A., Persoon, A. M., Kurth, W. S., Groene, J. B., Averkamp, T. F., Dougherty, M. K., & Southwood, D. J. (2007). The variable rotation period of the inner region of Saturn's plasma disk. *Science*, *316*(5823), 442. doi: 10.1126/science.1138562

Hill, T. W., & Michel, F. C. (1976). Heavy ions from the Galilean satellites and the centrifugal distortion of the Jovian magnetosphere. *Journal of Geophysical Research*, *81*(25), 4561–4565. doi: 10.1029/JA081i025p04561

Hunt, G. J., Cowley, S. W. H., Provan, G., Bunce, E. J., Alexeev, I. I., Belenkaya, E. S., ... Coates, A. J. (2014). Field-aligned currents in Saturn's southern nightside magnetosphere: Subcorotation and planetary period oscillation components. *Journal of Geophysical Research: Space Physics*, *119*(12), 9847–9899. doi: 10.1002/2014JA020506

Hunt, G. J., Cowley, S. W. H., Provan, G., Bunce, E. J., Alexeev, I. I., Belenkaya, E. S., ... Coates, A. J. (2015). Field-aligned currents in Saturn's northern nightside magnetosphere: Evidence for interhemispheric current flow associated with planetary period oscillations. *Journal of Geophysical Research: Space Physics*, *120*(9), 7552–7584. doi: 10.1002/2015JA021454

Jackman, C. M., Thomsen, M. F., & Dougherty, M. K. (2019). Survey of Saturn's magnetopause and bow shock positions over the entire Cassini mission: Boundary statistical properties and exploration of associated upstream conditions. *Journal of Geophysical Research: Space Physics*, *124*(11), 8865–8883. doi: 10.1029/2019JA026628

Jacobs, J. A., Kato, Y., Matsushita, S., & Troitskaya, V. A. (1964). Classification of

geomagnetic micropulsations. *Journal of Geophysical Research*, *69*(1), 180–181. doi: 10.1029/JZ069i001p00180

Jia, X., Hansen, K. C., Gombosi, T. I., Kivelson, M. G., Tóth, G., DeZeeuw, D. L., & Ridley, A. J. (2012). Magnetospheric configuration and dynamics of Saturn's magnetosphere: A global MHD simulation. *Journal of Geophysical Research: Space Physics*, *117*(A5). doi: 10.1029/2012JA017575

Jia, X., & Kivelson, M. G. (2012). Driving Saturn's magnetospheric periodicities from the upper atmosphere/ionosphere: Magnetotail response to dual sources. *Journal of Geophysical Research: Space Physics*, *117*(A11). doi: 10.1029/2012JA018183

Jia, X., & Kivelson, M. G. (2016). Dawn-dusk asymmetries in rotating magnetospheres: Lessons from modeling Saturn. *Journal of Geophysical Research: Space Physics*, *121*(2), 1413–1424. doi: 10.1002/2015JA021950

Jia, X., Kivelson, M. G., & Gombosi, T. I. (2012). Driving Saturn's magnetospheric periodicities from the upper atmosphere/ionosphere. *Journal of Geophysical Research: Space Physics*, *117*(A4). doi: 10.1029/2011JA017367

Khurana, K. K., Arridge, C. S., Schwarzl, H., & Dougherty, M. K. (2006). A model of Saturn's magnetospheric field based on latest Cassini observations. In *AGU Spring Meeting Abstracts* (Vol. 2007, p. P44A-01).

Khurana, K. K., & Kivelson, M. G. (1989). Ultralow frequency MHD waves in Jupiter's middle magnetosphere. *Journal of Geophysical Research*, *94*(A5), 5241. doi: 10.1029/JA094iA05p05241

Khurana, K. K., Sheng Hsien Chen, Max Hammond, C., & Kivelson, M. G. (1992). Ultralow frequency waves in the magnetotails of the Earth and the outer planets. *Advances in Space Research*, *12*(8), 57–63. doi: 10.1016/0273-1177(92)90377-A

Kivelson, M. G. (1976). Jupiter's distant environment. In *Physics of solar planetary environments: Proceedings of the international symposium on solar-terrestrial physics, June 7–18, 1976 Boulder, Colorado volume II* (pp. 836–853). American Geophysical

Union (AGU). doi: 10.1029/SP008p0836

Kleindienst, G., Glassmeier, K.-H., Simon, S., Dougherty, M. K., & Krupp, N. (2009). Quasiperiodic ULF-pulsations in Saturn's magnetosphere. *Annales Geophysicae*, *27*(2), 885–894. doi: 10.5194/angeo-27-885-2009

Kramers, H. A. (1926). Wellenmechanik und halbzahlige Quantisierung. *Zeitschrift für Physik*, *39*(10-11), 828–840. doi: 10.1007/BF01451751

Lepping, R. P., Burlaga, L. F., & Klein, L. W. (1981). Surface waves on Saturn's magnetopause. *Nature*, *292*(5825), 750–753. doi: 10.1038/292750a0

Li, W., Thorne, R. M., Nishimura, Y., Bortnik, J., Angelopoulos, V., McFadden, J. P., ... Auster, U. (2010). THEMIS analysis of observed equatorial electron distributions responsible for the chorus excitation. *Journal of Geophysical Research: Space Physics*, *115*(A6). doi: 10.1029/2009JA014845

Liu, W., & Fujimoto, M. (Eds.). (2011). *The Dynamic Magnetosphere*. Dordrecht: Springer Netherlands. doi: 10.1007/978-94-007-0501-2

Lysak, R. L., & Song, Y. (2020). Field line resonances in Jupiter's magnetosphere. *Geophysical Research Letters*, *47*(18). doi: 10.1029/2020GL089473

MacDowall, R., Kaiser, M., Desch, M., Farrell, W., Hess, R., & Stone, R. (1993). Quasiperiodic jovian radio bursts: Observations from the Ulysses radio and plasma wave experiment. *Planetary and Space Science*, *41*(11-12), 1059–1072. doi: 10.1016/0032-0633(93)90109-F

Mallat, S. G. (2009). *A wavelet tour of signal processing: The sparse way* (3rd ed ed.). Amsterdam ; Boston: Elsevier/Academic Press.

Manners, H., & Masters, A. (2019). First evidence for multiple-harmonic standing Alfvén waves in Jupiter's equatorial plasma sheet. *Geophysical Research Letters*, *46*(16), 9344–9351. doi: 10.1029/2019GL083899

Mathie, R. A., & Mann, I. R. (2000). Observations of Pc5 field line resonance azimuthal phase speeds: A diagnostic of their excitation mechanism. *Journal of Geophysical*

Research: Space Physics, *105*(A5), 10713–10728. doi: 10.1029/1999JA000174

Matzka, J., Stolle, C., Yamazaki, Y., Bronkalla, O., & Morschhauser, A. (2021). The geomagnetic *Kp* index and derived indices of geomagnetic activity. *Space Weather*, *19*(5). doi: 10.1029/2020SW002641

McKibben, R., Simpson, J., & Zhang, M. (1993). Impulsive bursts of relativistic electrons discovered during Ulysses' traversal of Jupiter's dusk-side magnetosphere. *Planetary and Space Science*, *41*(11-12), 1041–1058. doi: 10.1016/0032-0633(93)90108-E

Menietti, J. D., Palmaerts, B., Zahlava, J., Averkamp, T. F., Groene, J. B., & Kurth, W. S. (2020). Quasiperiodic Saturn auroral hiss observed during a Cassini proximal orbit. *Journal of Geophysical Research: Space Physics*, *125*(1). doi: 10.1029/2019JA027338

Menk, F. W., & Waters, C. L. (2013). *Magnetoseismology: Ground-based remote sensing of Earth's magnetosphere* (First ed.). Wiley. doi: 10.1002/9783527652051

Min, K., Bortnik, J., Denton, R. E., Takahashi, K., Lee, J., & Singer, H. J. (2013). Quiet time equatorial mass density distribution derived from AMPTE/CCE and GOES using the magnetoseismology technique. *Journal of Geophysical Research: Space Physics*, *118*(10), 6090–6105. doi: 10.1002/jgra.50563

Mitchell, D. G., Carbary, J., Bunce, E., Radioti, A., Badman, S., Pryor, W., ... Kurth, W. (2016). Recurrent pulsations in Saturn's high latitude magnetosphere. *Icarus*, *263*, 94–100. doi: 10.1016/j.icarus.2014.10.028

Mitchell, D. G., Krimigis, S. M., Paranicas, C., Brandt, P., Carbary, J., Roelof, E., ... Pryor, W. (2009). Recurrent energization of plasma in the midnight-to-dawn quadrant of Saturn's magnetosphere, and its relationship to auroral UV and radio emissions. *Planetary and Space Science*, *57*(14-15), 1732–1742. doi: 10.1016/j.pss.2009.04.002

Mitchell, D. G., Kurth, W. S., Hospodarsky, G. B., Krupp, N., Saur, J., Mauk, B. H., ... Hamilton, D. C. (2009). Ion conics and electron beams associated with auroral processes on Saturn. *Journal of Geophysical Research: Space Physics*, *114*(A2). doi: 10.1029/2008JA013621

Olson, W. P., & Pfitzer, K. A. (1974). A quantitative model of the magnetospheric magnetic field. *Journal of Geophysical Research*, *79*(25), 3739–3748. doi: 10.1029/JA079i025p03739

Orr, D. (1973). Magnetic pulsations within the magnetosphere: A review. *Journal of Atmospheric and Terrestrial Physics*, *35*(1), 1–50. doi: 10.1016/0021-9169(73)90214-6

Orr, D., & Matthew, J. A. D. (1971). The variation of geomagnetic micropulsation periods with latitude and the plasmapause. *Planetary and Space Science*, *19*(8), 897–905. doi: 10.1016/0032-0633(71)90141-3

Palmaerts, B., Roussos, E., Krupp, N., Kurth, W., Mitchell, D., & Yates, J. (2016). Statistical analysis and multi-instrument overview of the quasi-periodic 1-hour pulsations in Saturn's outer magnetosphere. *Icarus*, *271*, 1–18. doi: 10.1016/j.icarus.2016.01.025

Pan, D.-X., Yao, Z.-H., Guo, R.-L., Bonfond, B., Wei, Y., Dunn, W., ... Wan, W.-X. (2021). A statistical survey of low-frequency magnetic fluctuations at Saturn. *Journal of Geophysical Research: Space Physics*, *126*(2). doi: 10.1029/2020JA028387

Press, W. H. (Ed.). (2007). *Numerical recipes: The art of scientific computing* (3rd ed ed.). Cambridge, UK ; New York: Cambridge University Press.

Provan, G., Andrews, D. J., Arridge, C. S., Coates, A. J., Cowley, S. W. H., Cox, G., ... Jackman, C. M. (2012). Dual periodicities in planetary-period magnetic field oscillations in Saturn's tail. *Journal of Geophysical Research: Space Physics*, *117*(A1). doi: 10.1029/2011JA017104

Provan, G., Cowley, S. W. H., Lamy, L., Bunce, E. J., Hunt, G. J., Zarka, P., & Dougherty, M. K. (2016). Planetary period oscillations in Saturn's magnetosphere: Coalescence and reversal of northern and southern periods in late northern spring. *Journal of Geophysical Research: Space Physics*, *121*(10), 9829–9862. doi: 10.1002/2016JA023056

Radoski, H. R. (1967a). Highly asymmetric MHD resonances: The guided poloidal mode. *Journal of Geophysical Research*, *72*(15), 4026–4027. doi: 10.1029/JZ072i015p04026

Radoski, H. R. (1967b). A note on oscillating field lines. *Journal of Geophysical Research*,

72(1), 418. doi: 10.1029/JZ072i001p00418

Radoski, H. R. (1972). The effect of asymmetry on toroidal hydromagnetic waves in a dipole field. *Planetary and Space Science*, *20*(7), 1015–1023. doi: 10.1016/0032-0633(72)90212-7

Ramer, K. M., Kivelson, M. G., Sergis, N., Khurana, K. K., & Jia, X. (2017). Spinning, breathing, and flapping: Periodicities in Saturn's middle magnetosphere. *Journal of Geophysical Research: Space Physics*, *122*(1), 393–416. doi: 10.1002/2016JA023126

Riley, K. F., Hobson, M. P., & Bence, S. J. (2006). *Mathematical Methods for Physics and Engineering* (Third ed.). Cambridge: Cambridge University Press. doi: 10.1017/CBO9780511810763

Roussos, E., Krupp, N., Mitchell, D., Paranicas, C., Krimigis, S., Andriopoulou, M., ... Dougherty, M. (2016). Quasi-periodic injections of relativistic electrons in Saturn's outer magnetosphere. *Icarus*, *263*, 101–116. doi: 10.1016/j.icarus.2015.04.017

Rusaitis, L., Khurana, K. K., Kivelson, M. G., & Walker, R. J. (2021). Quasiperiodic 1-hour Alfvén wave resonances in Saturn's magnetosphere: Theory for a realistic plasma/field model. *Geophysical Research Letters*. doi: 10.1029/2020GL090967

Russell, C. T., Luhmann, J. G., & Strangeway, R. J. (2016). *Space physics: An introduction*. New York, NY: Cambridge University Press.

Sandhu, J. K., Yeoman, T. K., Fear, R. C., & Dandouras, I. (2016). A statistical study of magnetospheric ion composition along the geomagnetic field using the Cluster spacecraft for L values between 5.9 and 9.5. *Journal of Geophysical Research: Space Physics*, *121*(3), 2194–2208. doi: 10.1002/2015JA022261

Sandhu, J. K., Yeoman, T. K., & Rae, I. J. (2018). Variations of field line eigenfrequencies with ring current intensity. *Journal of Geophysical Research: Space Physics*, *123*(11), 9325–9339. doi: 10.1029/2018JA025751

Sandhu, J. K., Yeoman, T. K., Rae, I. J., Fear, R. C., & Dandouras, I. (2017). The dependence of magnetospheric plasma mass loading on geomagnetic activity using

Cluster. *Journal of Geophysical Research: Space Physics*, *122*(9), 9371–9395. doi: 10.1002/2017JA024171

Schardt, A. W., Kurth, W. S., Lepping, R. P., & Maclennan, C. G. (1985). Particle acceleration in Saturn's outer magnetosphere: In memoriam Alois Schardt. *Journal of Geophysical Research*, *90*(A9), 8539. doi: 10.1029/JA090iA09p08539

Sheeley, B. W., Moldwin, M. B., Rassoul, H. K., & Anderson, R. R. (2001). An empirical plasmasphere and trough density model: CRRES observations. *Journal of Geophysical Research: Space Physics*, *106*(A11), 25631–25641. doi: 10.1029/2000JA000286

Singer, H. J., Southwood, D. J., Walker, R. J., & Kivelson, M. G. (1981). Alfvén wave resonances in a realistic magnetospheric magnetic field geometry. *Journal of Geophysical Research: Space Physics*, *86*(A6), 4589–4596. doi: 10.1029/JA086iA06p04589

Sinha, S., Routh, P. S., Anno, P. D., & Castagna, J. P. (2005). Spectral decomposition of seismic data with continuous-wavelet transform. *GEOPHYSICS*, *70*(6), P19-P25. doi: 10.1190/1.2127113

Smith, E. J., Davis, L., Jones, D. E., Coleman, P. J., Colburn, D. S., Dyal, P., & Sonett, C. P. (1980). Saturn's magnetic field and magnetosphere. *Science*, *207*(4429), 407–410. doi: 10.1126/science.207.4429.407

Southwood, D. J. (1974). Some features of field line resonances in the magnetosphere. *Planetary and Space Science*, *22*(3), 483–491. doi: 10.1016/0032-0633(74)90078-6

Southwood, D. J., & Kivelson, M. G. (1986). The effect of parallel inhomogeneity on magnetospheric hydromagnetic wave coupling. *Journal of Geophysical Research*, *91*(A6), 6871. doi: 10.1029/JA091iA06p06871

Takahashi, K. (2004). Frequencies of standing Alfvén wave harmonics and their implication for plasma mass distribution along geomagnetic field lines: Statistical analysis of CRRES data. *Journal of Geophysical Research*, *109*(A8), A08202. doi: 10.1029/2003JA010345

Takahashi, K., Hartinger, M. D., Angelopoulos, V., & Glassmeier, K.-H. (2015). A statistical

study of fundamental toroidal mode standing Alfvén waves using THEMIS ion bulk velocity data. *Journal of Geophysical Research: Space Physics*, *120*(8), 6474–6495. doi: 10.1002/2015JA021207

Takahashi, K., Lee, D.-H., Merkin, V. G., Lyon, J. G., & Hartinger, M. D. (2016). On the origin of the dawn-dusk asymmetry of toroidal Pc5 waves. *Journal of Geophysical Research: Space Physics*, *121*(10), 9632–9650. doi: 10.1002/2016JA023009

Tamao, T. (1965). Transmission and coupling resonance of hydromagnetic disturbances in the non-uniform Earth's magnetosphere. *Science reports of the Tohoku University. Ser. 5, Geophysics*, *17*, 43–70.

Tapping, K. F. (2013). The 10.7 cm solar radio flux ($F_{10.7}$): F10.7. *Space Weather*, *11*(7), 394–406. doi: 10.1002/swe.20064

Tenfjord, P., Østgaard, N., Snekvik, K., Laundal, K. M., Reistad, J. P., Haaland, S., & Milan, S. E. (2015). How the IMF B_y induces a B_y component in the closed magnetosphere and how it leads to asymmetric currents and convection patterns in the two hemispheres. *Journal of Geophysical Research: Space Physics*, *120*(11), 9368–9384. doi: 10.1002/2015JA021579

Tsyganenko, N. A. (1995). Modeling the Earth's magnetospheric magnetic field confined within a realistic magnetopause. *Journal of Geophysical Research*, *100*(A4), 5599. doi: 10.1029/94JA03193

Tsyganenko, N. A. (1996). Effects of the solar wind conditions in the global magnetospheric configurations as deduced from data-based field models (Invited). In *Proceedings of the 3rd International Conference on Substorms* (Vol. 389, p. 181). Versailles, 12-17 May 1996.

Tsyganenko, N. A. (1998). Modeling of twisted/warped magnetospheric configurations using the general deformation method. *Journal of Geophysical Research: Space Physics*, *103*(A10), 23551–23563. doi: 10.1029/98JA02292

Tsyganenko, N. A. (2002). A model of the near magnetosphere with a dawn-dusk asymmetry

1. Mathematical structure. *Journal of Geophysical Research: Space Physics*, *107*(A8), SMP 12-1-SMP 12-15. doi: 10.1029/2001JA000219

Walker, R. J. (1976). An evaluation of recent quantitative magnetospheric magnetic field models. *Reviews of Geophysics*, *14*(3), 411. doi: 10.1029/RG014i003p00411

Warner, M., & Orr, D. (1979). Time of flight calculations for high latitude geomagnetic pulsations. *Planetary and Space Science*, *27*(5), 679–689. doi: 10.1016/0032-0633(79)90165-X

Welch, P. (1967). The use of fast Fourier transform for the estimation of power spectra: A method based on time averaging over short, modified periodograms. *IEEE Transactions on Audio and Electroacoustics*, *15*(2), 70–73. doi: 10.1109/TAU.1967.1161901

Wentzel, G. (1926). Eine Verallgemeinerung der Quantenbedingungen für die Zwecke der Wellenmechanik. *Zeitschrift für Physik*, *38*(6-7), 518–529. doi: 10.1007/BF01397171

Wild, J. A., Yeoman, T. K., & Waters, C. L. (2005). Revised time-of-flight calculations for high-latitude geomagnetic pulsations using a realistic magnetospheric magnetic field model. *Journal of Geophysical Research*, *110*(A11), A11206. doi: 10.1029/2004JA010964

Wilson, R. J., & Dougherty, M. K. (2000). Evidence provided by Galileo of ultra low frequency waves within Jupiter's middle magnetosphere. *Geophysical Research Letters*, *27*(6), 835–838. doi: 10.1029/1999GL010750

Wright, A. N., & Elsden, T. (2020). Simulations of MHD Wave Propagation and Coupling in a 3-D Magnetosphere. *Journal of Geophysical Research: Space Physics*, *125*(2). doi: 10.1029/2019JA027589

Yates, J. N., Southwood, D. J., Dougherty, M. K., Sulaiman, A. H., Masters, A., Cowley, S. W. H., ... Coates, A. J. (2016). Saturn's quasiperiodic magnetohydrodynamic waves. *Geophysical Research Letters*, *43*(21), 11,102–11,111. doi: 10.1002/2016GL071069

Zhang, S., Tian, A., Shi, Q., Li, H., Degeling, A. W., Rae, I. J., ... Pu, Z. (2018). Statistical

study of ULF waves in the magnetotail by THEMIS observations. *Annales Geophysicae*, *36*(5), 1335–1346. doi: 10.5194/angeo-36-1335-2018